Anomalous Hall effect and Spin-Orbit Torques in Noncollinear Antiferromagnetic $Mn_3Ni_{0.35}Cu_{0.65}N$ thin films

Dissertation

zur Erlangung des Grades

Doktor der Naturwissenschaften (Dr. rer. nat.)

am Fachbereich Physik

der Johannes Gutenberg-Universität Mainz

von:

Adithya Rajan

geboren in Chennai, Indien

Mainz, 2025

Adithya Rajan

Anomalous Hall effect and Spin-Orbit Torques in Noncollinear Antiferromagnetic $Mn_3Ni_{0.35}Cu_{0.65}N$ thin films

Datum der mündlichen Prüfung:

Gutachter: *Removed due to data privacy.*

Kommission: *Removed due to data privacy.*

Johannes Gutenberg Universität Mainz
AG Kläui
Institut für Physik
Staudingerweg 7
55128 Mainz

Declaration of Authorship

I hereby declare that I have composed this thesis independently and that it has not been submitted, either in the same or a similar form, for another degree. I have used only the resources and aids indicated and have appropriately acknowledged all sources of ideas, quotations, and materials.

Hiermit erkläre ich, dass ich die vorliegende Dissertation selbstständig und ohne unerlaubte Hilfe Dritter verfasst habe. Die Arbeit wurde bisher weder im Inland noch im Ausland in gleicher oder ähnlicher Form im Rahmen eines Prüfungsverfahrens vorgelegt. Es wurden ausschließlich die angegebenen Quellen und Hilfsmittel verwendet und alle Stellen, die wörtlich oder sinngemäß aus anderen Werken entnommen wurden, sind als solche kenntlich gemacht.

Adithya Rajan

Abstract

The continued scaling of conventional charge-based electronics faces significant challenges, creating an urgent need for alternative paradigms capable of delivering low-power, high-speed, and scalable computing technologies. Spintronics, by exploiting the spin and orbital degrees of freedom of electrons, has emerged as a promising pathway, particularly through the development of spin–orbit torque (SOT) based memory devices. In this context, noncollinear antiferromagnets (NCAFM) offer a unique materials platform, combining vanishing net magnetization with exotic spin textures that can give rise to robust electronic transport phenomena such as the anomalous Hall effect (AHE) and unconventional spin–orbit torques.

This thesis investigates the anomalous Hall effect and spin–orbit torques in the cubic antiperovskite $Mn_3Ni_{0.35}Cu_{0.65}N$ (Mn_3NiCuN). A detailed experimental framework was established to disentangle higher-order contributions to the AHE by performing angular-dependent Hall measurements under both in-plane and out-of-plane magnetic field geometries. A nontrivial in-plane AHE was observed, confirming the presence of higher-order multipolar contributions—specifically, an octupolar moment—rather than conventional dipolar magnetization. The angular dependence of the AHE exhibited a 120° symmetry, consistent with the symmetry of the octupolar spin texture, and was further supported by phenomenological modeling that incorporated scalar spin chirality (SSC) contributions to the transport signal.

In parallel, spin–orbit torques were investigated via second harmonic Hall measurements and spin-torque ferromagnetic resonance (ST-FMR). A significant enhancement of the damping-like torque was observed near the Néel temperature. This enhancement could be attributed to two alternative mechanisms: (i) increased spin and orbital current generation from critical fluctuations of the noncollinear antiferromagnetic order, and (ii) spin currents arising from fluctuation-induced scalar spin chirality. Notably, this work presents the first experimental indication of orbital Hall effect contributions in a NCAFM, offering a new perspective on angular momentum generation in complex magnetic systems.

The findings of this thesis provide direct insight into the role of higher-order magnetic multipoles, critical spin fluctuations, and orbital transport in NCAFM. Beyond advancing fundamental understanding, these results highlight the potential of NCAFMs for developing energy-efficient, field-free spintronic devices, marking a significant step toward exploiting complex magnetic textures for future information technologies.

Zusammenfassung

Die fortschreitende Miniaturisierung konventioneller ladungsbasierter Elektronik stößt zunehmend auf fundamentale physikalische und thermische Grenzen. Daher besteht ein dringender Bedarf an alternativen Paradigmen, die niedrige Leistungsaufnahme, hohe Geschwindigkeit und Skalierbarkeit ermöglichen. Die Spintronik, welche den Spin und das Bahnmoment der Elektronen nutzt, stellt einen vielversprechenden Ansatz dar, insbesondere durch die Entwicklung spin–orbitaler Drehmoment (SOT)-basierter Speichertechnologien. In diesem Kontext bieten nichtkollineare Antiferromagnete (NCAFM) ein einzigartiges Materialsystem, das trotz fehlender Netto-Magnetisierung exotische Spinanordnungen aufweist und robuste elektronische Transporteigenschaften wie den anomalen Halleffekt (AHE) und unkonventionelle Spin–Orbit-Torques ermöglicht.

In dieser Arbeit wird der anomale Halleffekt sowie die Erzeugung von Spin–Orbit-Torques in der kubischen Antiperowskit-Verbindung $Mn_3Ni_{0.35}Cu_{0.65}N$ (MNCN) untersucht. Ein detaillierter experimenteller Ansatz wurde entwickelt, um höhere Beiträge zum AHE zu isolieren, indem winkelabhängige Hallmessungen sowohl im in-plane als auch im out-of-plane Magnetfeld durchgeführt wurden. Dabei konnte ein nichttrivialer AHE im in-plane-Messaufbau beobachtet werden, was auf Beiträge höherer Ordnung –insbesondere von Oktupolmomenten – anstelle der klassischen Dipol-Magnetisierung hinweist. Die Winkelabhängigkeit des AHE zeigte eine charakteristische 120° Symmetrie, im Einklang mit der symmetrischen Anordnung der Oktupolstruktur, und wurde zusätzlich durch ein phänomenologisches Modell unterstützt, das Beiträge von skalaren Spin-Chiralitäten (SSC) berücksichtigt.

Parallel dazu wurden Spin–Orbit-Torques mittels Second Harmonic Hall Measurements und Spin-Torque Ferromagnetic Resonance (ST-FMR) untersucht. Es wurde eine deutliche Verstärkung des dämpfungsartigen Drehmoments nahe der Néel- Temperatur festgestellt. Diese Verstärkung lässt sich auf zwei alternative Mechanismen zurückführen: (i) die Erzeugung von Spin- und Orbitalströmen infolge kritischer Fluktuationen der nichtkollinearen antiferromagnetischen Ordnung oder (ii) auf Spinströme, die durch fluktuationsinduzierte skalare Spin-Chiralität entstehen. Hervorzuhe-

ben ist, dass in dieser Arbeit erstmals experimentelle Hinweise auf Beiträge des orbitalen Halleffekts (OHE) in einem nichtkollinearen Antiferromagneten erbracht wurden.

Die Ergebnisse dieser Arbeit liefern tiefe Einblicke in die Rolle höherer magnetischer Multipolmomente, kritischer Spinfluktuationen und orbitaler Transporteigenschaften in nichtkollinearen Antiferromagneten. Über die fundamentale Bedeutung hinaus zeigen sie auf, dass NCAFMs ein großes Potenzial für die Entwicklung energieeffizienter, feldfreier Spintronikbauelemente besitzen, und eröffnen neue Perspektiven für die Nutzung komplexer magnetischer Strukturen in zukünftigen Informationstechnologien.

Contents

List of Figures

Acknowledgments

Removed due to data privacy.

1. Introduction

For decades, the semiconductor industry has advanced under the guiding principle of Moore's Law [1, 2], which predicts an exponential increase in the number of transistors that can be integrated onto a silicon chip. However, as devices continue to scale down in size, fundamental physical and thermal limitations have emerged, posing serious challenges to power efficiency, thermal dissipation, and reliability. At the same time, the ever-increasing demand for data storage, real-time processing, and low-power computation in emerging technologies—such as edge computing, neuromorphic hardware, and AI accelerators—has exposed the need for alternative computing paradigms that can complement or surpass traditional charge-based electronics.

Spintronics, which exploits the intrinsic angular momentum of electrons in addition to their charge, has emerged as a promising candidate to address these challenges. By utilizing spin degrees of freedom to store and manipulate information, spintronic devices offer nonvolatility, high endurance, and low-energy switching capabilities. A central mechanism in next-generation spintronic memory technologies such as spin-orbit torque magnetic random-access memory (SOT-MRAM) is the ability to efficiently switch the magnetization of a nanomagnet using current-induced torques rather than magnetic fields. Conventionally, such spin-orbit torques (SOTs) are realized in heavy metal/ferromagnet bilayers via the spin Hall effect (SHE), where an applied in-plane electric current in a heavy metal induces a transverse spin current that diffuses into an adjacent magnetic layer, exerting a torque [3].

While ferromagnets have long been the cornerstone of spintronic devices, antiferromagnetic materials—and in particular, noncollinear antiferromagnets (NCAFMs)—are gaining increasing attention as a fundamentally distinct and technologically relevant alternative. Unlike conventional antiferromagnets, NCAFMs feature chiral spin textures that break time-reversal symmetry without producing a net magnetization. These spin configurations can host a variety of emergent phenomena, including anomalous Hall effects (AHE) [4, 5, 6, 7], even in the absence of ferromagnetic order. Their lack of stray fields, ultrafast spin dynamics, and robustness against external perturbations make NCAFMs particularly appealing for high-density, low-power memory and logic devices.

The breaking of time-reversal symmetry (TRS) in combination with spin-orbit coupling (SOC) gives rise to a transverse flow of electrons manifesting as an anomalous Hall voltage—a hallmark long associated with ferromagnets [8, 3]. However, it has been predicted and subsequently confirmed in materials such as Mn_3Sn and Mn_3Ge that NCAFMs with noncoplanar spin textures can also host a large AHE, despite having no net magnetic moment [5, 6]. In these materials, the magnitude of the AHE cannot be explained by their small residual magnetization [5, 7], suggesting that the effect arises from Berry curvature generated by the symmetry of the spin lattice. However, many experimental studies rely on out-of-plane field geometries that potentially confound the magnetization signal with intrinsic Hall contributions. A comprehensive understanding of the AHE in these systems thus requires field-angle-resolved measurements that probe the symmetry of the transverse response.

In parallel, spin-orbit torque generation mechanisms are being actively investigated in NCAFMs. While the SHE and inverse spin galvanic effect (iSGE) have provided a framework for understanding current-induced torques in conventional systems, orbital Hall currents—arising from the orbital character of the band structure—are now being explored as an alternative angular momentum source [10, 11, 12]. These orbital currents are not limited by SOC and may enable torque generation in a wider range of materials, including light metals and antiferromagnets. Moreover, recent theoretical work has predicted that spin fluctuations in chiral NCAFMs can enhance spin and orbital current generation near the Néel temperature [13], potentially giving rise to fluctuation-mediated torques—a phenomenon recently observed in ferromagnets [14, 15, 16] and collinear antiferromagnets [17, 18], but still unconfirmed in noncollinear systems.

In this thesis, we explore this open question through a systematic study of spin-orbit torques in the noncollinear antiferromagnet $Mn_3Ni_{0.35}Cu_{0.65}N$ (Mn_3NiCuN), a cubic antiperovskite material with a Néel temperature near 210 K. The accessible temperature range allows us to investigate the angular dependence, symmetry, and fluctuation-enhanced behavior of spin and orbital torques from cryogenic temperatures to room temperature. Our results offer new insights into the interplay of chirality, Berry curvature, and spin fluctuations in NCAFMs, and point toward novel pathways for designing energy-efficient spintronic devices using antiferromagnetic order.

2. Theory

2.1. Microscopic Origins of Magnetism

Magnetism in solids is a macroscopic manifestation of the quantum mechanical properties of electrons, primarily. These properties include intrinsic spin, orbital motion, and the collective interactions among electrons within atoms and across atomic sites in crystalline solids. The total magnetic moment of an atom arises from the spin and orbital magnetic moments of its electrons, and these atomic moments interact via quantum mechanical exchange to form different types of magnetic order, such as ferromagnetism, antiferromagnetism, and ferrimagnetism. Understanding these microscopic origins is crucial for interpreting a wide range of phenomena, from classical magnetic ordering to modern spintronic effects[19, 20].

2.1.1. Atomic magnetism

Each electron possesses an intrinsic form of angular momentum known as spin. Spin is a purely quantum mechanical property, characterized by a quantum number s=1/2, and has no classical analog. The spin angular momentum vector $\vec{S}$ is given by

$$\vec{S} = \sqrt{s(s+1)}\hbar, \tag{2.1}$$

where s is the spin quantum number of the electron and $\hbar$ is the reduced Planck's constant. The associated magnetic moment is given by

$$\vec{\mu}_{\text{spin}} = -g\frac{\mu_B \vec{S}}{\hbar}, \tag{2.2}$$

where μ_B is the Bohr magneton and g $\approx$ 2 is the Landé g-factor for the electron spin. Electrons also possess orbital angular momentum due to their motion in quantized atomic orbitals, which generates a magnetic moment

$$\vec{\mu}_{\text{orb}} = -\frac{\mu_B \vec{L}}{\hbar}, \tag{2.3}$$

where $\vec{L}$ is the orbital angular momentum operator. Then, the total magnetic moment is given by

$$\vec{\mu}_{\text{tot}} = \vec{\mu}_{\text{spin}} + \vec{\mu}_{\text{orb}} = -\frac{\mu_B}{\hbar}(\vec{L} + 2\vec{S}) \tag{2.4}$$

Spin–orbit coupling (SOC) is a relativistic interaction that links the spin and orbital motion of electrons. It arises from the transformation of the nuclear electric field into an effective magnetic field in the rest frame of the moving electron. This effective field interacts with the spin magnetic moment of the electron, leading to an additional term in the Hamiltonian of the form

$$\hat{H}_{SO} = \lambda_{SO}\vec{L} \cdot \vec{S}, \tag{2.5}$$

where λ_{SO} is the spin–orbit coupling constant. SOC plays a fundamental role in determining magnetocrystalline anisotropy and is essential in modern spintronics, influencing phenomena such as the anomalous Hall effect and spin–orbit torque [21].

The coupling between spin and orbital angular momentum alters the electronic energy levels, leading to the splitting of degenerate states and introducing a directional dependence into the magnetic properties of the material.

The total magnetic moment of an electron is the vector sum of its spin and orbital contributions. In atoms with multiple electrons, these contributions are combined according to specific coupling schemes. The most common of these is LS (Russell–Saunders) coupling, where the total spin $\vec{S} = \sum \vec{s_i}$ and total orbital angular momentum $\vec{L} = \sum \vec{l_i}$ are formed first and then combined into the total angular momentum $\vec{J} = \vec{L} + \vec{S}$. This scheme is dominant for light atoms, where spin–orbit coupling is relatively weak. In contrast, in heavy atoms, the strong spin–orbit interaction leads to the dominance of J-J coupling, where individual orbital and spin angular momenta ($\vec{j_i} = \vec{s_i} + \vec{l_i}$) are combined first before summing over all electrons. In multi-electron atoms, only electrons occupying partially filled shells contribute to the net angular momentum, as the contributions from fully filled shells cancel out due to paired spins and opposite orbital momenta. The total angular momentum of such atoms arises from different combinations of spin and orbital angular momenta associated with the unfilled shells, and these configurations determine the atom's energy levels. In addition to the Pauli exclusion principle, the distribution of electrons within these shells is governed by Hund's rules [20], which provide a set of empirical guidelines for identifying the ground state of an atom. As a result, elements such as iron (Fe), cobalt (Co), and nickel (Ni), which possess incompletely filled 3d subshells, exhibit a net atomic magnetic moment. This moment is a prerequisite for the emergence of conventional ferromagnetism in solid-state systems.

2.1.2. Magnetism in Solids

When atoms are brought together in a solid, their magnetic moments interact. One of the most fundamental interactions responsible for magnetic order is the exchange interaction. Unlike classical magnetic interactions, exchange arises from the quantum mechanical requirement that the total wavefunction for identical fermions must be antisymmetric. The energy difference between spin-parallel and spin-antiparallel configurations can be described using the exchange integral J, which appears in the Heisenberg exchange Hamiltonian:

$$\hat{H} = -2J\vec{S}_1 \cdot \vec{S}_2 \tag{2.6}$$

If J $>$ 0, the system favors parallel spin alignment, resulting in ferromagnetism. If J $<$ 0, antiparallel alignment is favored, leading to antiferromagnetism. This concept generalizes in solids through the Heisenberg model:

$$\hat{H} = -\sum_{i,j} J_{ij}\vec{S}_i \cdot \vec{S}_j, \tag{2.7}$$

where J_{ij} characterizes the interaction strength between spins at sites i and j. The value of J_{ij} depends on the spatial overlap of atomic orbitals, electronic configuration, and the crystal environment. In insulating systems, this model is highly effective and forms the basis for describing magnetic excitations, domain formation, and critical behavior near phase transitions. However, the localized picture is insufficient for describing magnetism in many metallic systems, where electrons—particularly those in the d-bands—are not strictly confined to individual atoms. In transition metals like Fe, Co, and Ni, the magnetic properties are better described using itinerant electron models. Here, magnetism arises from the collective behaviour of conduction electrons whose spin-dependent band structure leads to a net magnetization.

The Stoner model provides a foundational theory for itinerant ferromagnetism [20]. It introduces a competition between the kinetic energy cost of spin polarization and the exchange energy gain. The criterion for ferromagnetic ordering is given by the Stoner

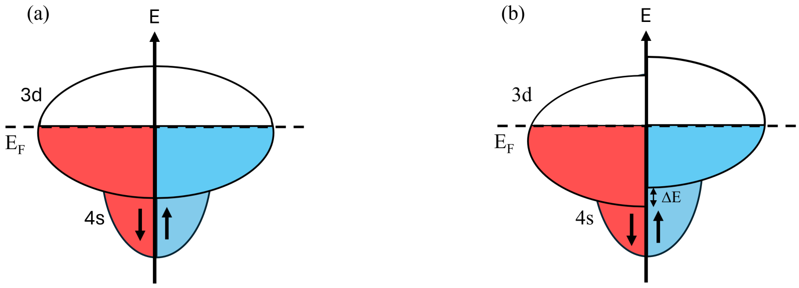

Figure 2.1.: (a) Band structure of a non-magnetic metal with equally filled spin sub-bands. (b) Band structure a ferromagnetic metal, exhibiting energy split spin sub-bands, leading to a different electronic population of the two spin-sub bands and to a net magnetic moment.

condition [22]:

$$I \cdot N(E_F) > 1, \tag{2.8}$$

where I is the Stoner exchange parameter and $N(E_F)$ is the density of states at the Fermi level. When this condition is met, the electron system lowers its total energy by developing a net spin imbalance, leading to spontaneous magnetization. In this model, the exchange interaction causes a spin-dependent shift in the electronic bands, splitting the spin-up and spin-down states, as opposed to a non-magnetic material which has a symmetric band structure. This results in different Fermi levels for each spin channel and gives rise to a magnetic moment per atom. The magnitude of the moment is determined by integrating the difference in densities of states across the Fermi surface. This framework explains why magnetic moments in transition metals are often non-integer ($\approx 2.2\ \mu_B$ in Fe) and why their magnitude is sensitive to alloying, pressure, and temperature. Advanced models build on the Stoner picture by incorporating band structure effects and electron correlations [23].

In conclusion, the microscopic origins of magnetism are rooted in the spin and orbital properties of electrons and their interactions, both within atoms and across a crystal lattice. Localized moment models, such as the Heisenberg Hamiltonian, are powerful for describing insulating magnets, while itinerant models like the Stoner and Hubbard frameworks are more apt for metallic and correlated systems. Together, these models form the theoretical foundation for modern magnetism and provide essential insights into magnetic materials used in technology ranging from permanent magnets to spintronic devices.

2.2. Micromagnetic Energy Terms

The micromagnetic approximation bridges atomic-scale magnetic properties with continuum-level magnetization behavior. In this framework, the magnetization vector field $\vec{M}(r)$ is treated as a continuous function of position, valid over length scales much larger than atomic spacing but smaller than typical device dimensions. This enables computational and analytical treatment of magnetization dynamics and equilibrium configurations, capturing phenomena such as domain walls, vortices, and skyrmions. The total magnetic energy is expressed as a functional of $\vec{M}(r)$, composed of several energy contributions rooted in atomic-scale interactions [20, 21]. The total micromagnetic energy E_{tot} is given by:

$$E_{tot} = \int [E_{ex}(r) + E_{ani}(r) + E_{Zeeman}(r) + ...]dV, \tag{2.9}$$

where $E_{ex}(r)$ is the exchange energy, $E_{ani}(r)$ the anisotropy energy and $E_{Zeeman}(r)$ the Zeeman energy. In the micromagnetic approximation, the exchange energy is written as

$$E_{ex} = A \int |\nabla m|^2 dV, \tag{2.10}$$

where A is the exchange stiffness and $\vec{m} = \vec{M}/M_s$ is the normalized magnetization vector. $E_{ex}(r)$ originates from the quantum mechanical exchange interaction between spins. It reflects the tendency of neighboring spins to align and can favor either parallel or antiparallel alignment depending on the sign of the exchange constant J. In ferromagnetic materials (J > 0), parallel alignment is favored, while in antiferromagnets (J < 0), antiparallel alignment minimizes energy.

The $E_{ex}(r)$ arises due to spin–orbit coupling and reflects the underlying crystal symmetry of the material, which energetically favors certain directions of magnetization. These preferred directions, known as easy axes, result in an energy penalty for deviations of the magnetization from specific crystallographic orientations.

In the general case, the magnetocrystalline anisotropy energy depends on the direction cosines α_i of the normalized magnetization vector $\vec{m}$ with respect to the crystal axes. For cubic systems, the lowest-order anisotropy term is expressed as:

$$E_{ani,cubic} = K_1(\alpha_1^2\alpha_2^2 + \alpha_2^2\alpha_3^2 + \alpha_3^2\alpha_1^2) \tag{2.11}$$

where K_1 is the cubic anisotropy constant and α_i are the direction cosines of $\vec{m}$ along the crystallographic x,y,z directions. This form reflects the equivalence of multiple symmetry axes in cubic lattices such as Fe or Ni.

For uniaxial anisotropy, where a single axis $\vec{e}_u$ defines the preferred magnetization direction, the energy can also be written in terms of direction cosines. If θ is the angle between $\vec{m}$ and $\vec{e}_u$, then the uniaxial anosotropy energy is:

$$E_{ani,uniaxial} = K_u sin^2(\theta) = K_u(1 - (\vec{m} \cdot \vec{e}_u)^2) \tag{2.12}$$

This dot product formulation is particularly useful for micromagnetic simulations and analytical treatments, where K_u denotes the uniaxial anisotropy constant and $\vec{e}_u$ is the unit vector along the easy axis.

Magnetocrystalline anisotropy plays a critical role in stabilizing magnetic domain structures, determining coercivity, and controlling switching behavior in spintronic devices. It competes with exchange and Zeeman energies to define the equilibrium spin configuration in ferromagnetic and antiferromagnetic materials [20, 21].

The Zeeman energy describes the interaction of magnetization with an external magnetic field $\vec{H}_{ext}$. It favors alignment of M with the field and is given by

$$E_{Zeeman} = \mu_0 \int \vec{M} \cdot \vec{H}_{ext} dV \tag{2.13}$$

This term plays a dominant role in magnetization switching and reorientation processes [21].

The demagnetization field, also known as the stray field, arises from the spatial distribution of magnetization within a magnetic material. It originates from effective magnetic “charges” that appear at surfaces or within the volume of the sample due to nonuniform magnetization. These charges generate an internal magnetic field that typically acts in opposition to the local magnetization direction, thereby contributing to the total magnetic energy.

Formally, the demagnetization field ($\vec{H}_d$ is derived from Maxwell’s equations under magnetostatic conditions, where no free current exists. It satisfies the relation:

$$\nabla \cdot \vec{H}_d = -\nabla \cdot \vec{M} \tag{2.14}$$

and is irrotational:

$$\nabla \times \vec{H}_d = 0 \tag{2.15}$$

Thus, it can be expressed as the gradient of a scalar potential ($\phi_m$$) : $\vec{H}_d = -\nabla\phi_m(2.16)$

where the scalar potential is obtained by solving Poisson's equation:

$$\nabla^2\phi_m = \nabla \cdot \mathbf{M}$$

The energy associated with the demagnetization field is given by:

$$E_{\text{demag}} = -\frac{1}{2}\mu_0 \int_V \vec{M} \cdot \vec{H}_d \, dV \tag{2.17}$$

This term is nonlocal, as $\vec{H}_d$ at a point depends on the magnetization over the entire sample volume, making its computation complex and computationally intensive in micromagnetic modeling.

Physically, the demagnetization field plays a critical role in the formation of magnetic domains. It promotes configurations that minimize magnetic poles by favoring closed-flux or flux-closure arrangements of spins. In thin films, it energetically penalizes out-of-plane magnetization, effectively stabilizing in-plane orientation. Similarly, in elongated structures, the field favors alignment of magnetization along the long axis, leading to shape-dependent anisotropy.

The formation of stable magnetic textures arises from the delicate balance between the various energy contributions described above. Exchange energy promotes spatial uniformity in magnetization, penalizing rapid directional changes. Anisotropy energy enforces alignment along preferred crystallographic directions, depending on material symmetry. The Zeeman energy tends to align magnetization with externally applied magnetic fields, while the demagnetizing energy favors flux closure and the minimization of magnetic stray fields. In ferromagnets such as iron, this competition results in the formation of magnetic domains and domain walls, where the balance between exchange and anisotropy sets the wall width, and demagnetizing energy governs domain shapes and sizes. Beyond simple domains, more intricate textures emerge when these energies compete under additional constraints. For instance, magnetic skyrmions—topologically protected whirls of spin—are stabilized by the interplay between exchange, Dzyaloshinskii–Moriya interaction (DMI), uniaxial anisotropy, and external magnetic fields [24, 25]. Another example is the helical spin spiral, a periodic spin arrangement where the magnetization continuously rotates along a propagation direction, stabilized in systems where competing ferromagnetic and antiferromagnetic interactions yield a minimum energy configuration at finite wavevector [26].

2.3. Models of Magnetic Order

Understanding magnetic order in solids requires theoretical models that describe how atomic magnetic moments (spins) interact and align under various conditions. Depending on the dimensionality, interaction symmetry, and temperature, different models apply. The key models discussed below provide essential insights into ferromagnetism and antiferromagnetism.

2.3.1. Weiss Mean Field Theory

The Weiss molecular field theory is one of the earliest and most widely used models to describe magnetic ordering in solids. It replaces the many-body spin interaction problem with an effective field approximation, assuming that each spin experiences a local molecular field proportional to the average magnetization of its neighbours. This leads to an effective field:

$$\vec{H}_{eff} = \vec{H}_{ext} + \lambda \vec{M}, \tag{2.18}$$

where λ is the molecular field constant. For ferromagnets, this results in the Curie–Weiss law for susceptibility:

$$\chi = \frac{C}{T - T_C} \tag{2.19}$$

which predicts a spontaneous magnetization below the Curie temperature T_C [19].

The theory can also be adapted for antiferromagnets by introducing two oppositely aligned sublattices A and B, each experiencing a field due to the other:

$$\vec{H}_A = \vec{H} + \lambda_B \vec{H}_B = \vec{H} + \lambda_A \tag{2.20}$$

Solving the coupled equations leads to the Néel temperature T_N, marking the transition from a paramagnetic to an antiferromagnetic state. The susceptibility follows:

$$\chi = \frac{C}{T + \theta} \tag{2.21}$$

with $\theta < 0$, reflecting antiferromagnetic interactions [21, 20]. While simplistic, the two-sublattice Weiss model captures key features such as zero net magnetization and a cusp in the susceptibility at T_N. It provides a useful approximation for interpreting AFM behaviour, though it becomes insufficient for noncollinear or frustrated systems.

2.3.2. Ising Model

The Ising model is a discrete, microscopic model of magnetism where spins are restricted to two values: $S_i = \pm 1$. The Hamiltonian is:

$$\hat{H} = -J \sum_{\langle i,j \rangle} S_i S_j - \mu \sum_i S_i H, \tag{2.22}$$

where J represents the exchange coupling, and $\langle i, j \rangle$ denotes summation over nearest neighbours. For J>0, the system favours ferromagnetic order, while J<0 leads to antiferromagnetic alignment. The Ising model shows no long-range order in 1D at finite temperature but exhibits a phase transition in 2D and 3D. The exact solution in 2D revealed a critical temperature below which spontaneous magnetization occurs [27]. The Ising model has become a cornerstone in the theory of critical phenomena. It captures essential features like spontaneous symmetry breaking, universality, and scaling laws. It is also a powerful tool in numerical studies, forming the basis for Monte Carlo simulations of magnetism and related statistical systems.

2.3.3. Heisenberg Model

The Heisenberg model extends the Ising model by treating spins as three-dimensional vectors. The Hamiltonian is:

$$\hat{H} = -J \sum_{\langle i,j \rangle} \vec{S}_i \cdot \vec{S}_j \tag{2.23}$$

This model captures the full rotational symmetry of spin interactions and is more physically accurate for most magnetic materials. For $J>0$, the ground state is ferromagnetic, while for $J<0$, antiferromagnetic order emerges.

It also forms the basis for studying more exotic phases like spin spirals and canted AFMs when extended with next-nearest-neighbour exchange or anisotropy. Its vectorial nature makes it ideal for modelling real magnets [19, 26].

2.3.4. The tanh Function in Magnetic Hysteresis Modelling

The hyperbolic tangent (tanh) is widely used to model magnetic hysteresis due to its natural emergence in mean-field theories and empirical effectiveness [28]. In the Ising model under mean-field approximation, magnetization at equilibrium is derived as:

$$\vec{M} = \tanh\left(\frac{\vec{H} + \lambda\vec{M}}{k_B T}\right) \tag{2.24}$$

where $\vec{H}$ is the external field, λ quantifies exchange interactions, and T is temperature. This arises from balancing Boltzmann-distributed spin states with a self-consistent molecular field, inherently producing an S-shaped curve with saturation. If hysteresis is modelled as a result of a Gaussian distribution of switching fields, the integrated magnetization follows the error function (erf):

$$erf(x) = \frac{2}{\sqrt{\pi}} \int_0^{\pi} e^{-t^2} dt \tag{2.25}$$

While erf differs mathematically from tanh, their shapes are similar, and tanh approximates erf with proper scaling (e.g., erf(x)≈ tanh (1.6x)). This makes tanh a pragmatic substitute, avoiding complex integrations. In addition, the tanh function is widely adopted in hysteresis modelling due to its simplicity, as closed-form derivatives expedite numerical computation. Its empirical fit aligns with the observed soft saturation behaviour in ferromagnetic materials, capturing the gradual approach to magnetization limits under increasing fields. Furthermore, the flexibility of tanh allows straightforward parameter tuning—such as slope and saturation amplitude—enabling adaptability to diverse material responses and experimental datasets. These attributes collectively render tanh a pragmatic choice for phenomenological [28] and mean-field descriptions of magnetic hysteresis.

2.4. Noncollinear Antiferromagnets

Noncollinear antiferromagnets (NCAFM) have emerged as a new paradigm in quantum materials, distinguished by complex spin textures that break time-reversal symmetry (TRS) without generating net magnetization. These materials exhibit a wealth of unconventional transport phenomena that were previously thought to require ferromagnetic order [29]. The emergence of these exotic transport phenomena is intimately linked to the underlying magnetic geometry and symmetry of the lattice. The magnetic spins are often arranged in triangular sub-lattices, forming a kagome lattice. If two adjacent atomic moments couple antiferromagnetically and collinearly, the orientation of the third moment becomes ambiguous—it is energetically unfavourable for it to align either parallel to the first or antiparallel to the second. This configuration gives rise to geometric frustration, wherein competing interactions prevent the system from minimizing its energy through a simple collinear arrangement [20]. A common resolution to this frustration is for the magnetic moments to orient themselves at 120° angles relative to one another within each triangle. This arrangement preserves magnetic compensation but removes collinearity, resulting in a NCAFM ground state [20]. Such magnetic order arises naturally from the specific crystal symmetries of materials like Mn_3NiN and Mn_3Sn [30] (Fig. 1(a) and (b) respectively), though their resulting spin textures differ due to variations in lattice symmetry and anisotropy.

In Mn_3NiN, the noncollinear AFM order develops within the (111) kagome plane of its cubic antiperovskite structure. As one moves from one Mn site to the next in

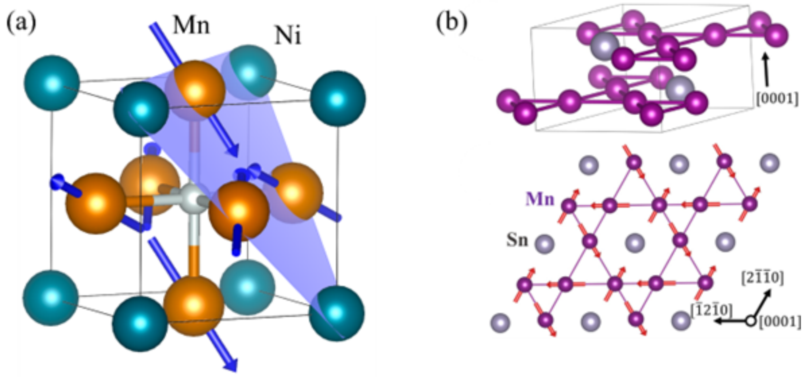

Figure 2.2.: Crystal structures of the NCAFM (a) Mn_3NiN showing cubic structure with triangular arrangement of Mn spins shown in golden spheres with dark blue arrows within the (111) plane shaded blue and (b) Mn_3Sn showing hexagonal arrangement and the Mn atoms in purple sphere arranged in the basal plane [30]

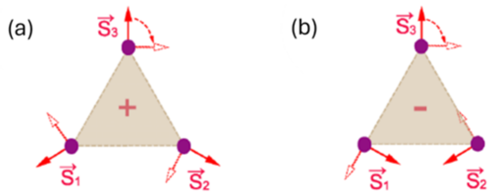

Figure 2.3.: Schematic showing the (a) triangular and (b) inverse triangular arrangement of spins in a NCAFM. The solid and hollow arrows show different in-plane spin rotation possibility with the same chiral structure. Adapted from [31]

a clockwise direction, each magnetic moment rotates by 120° clockwise, forming a triangular spin texture shown in Fig. reffig:Two$_C$$hirality(a).Incontrast,Mn_3$$Sn$ crystallizes in a hexagonal structure, with noncollinear order confined to the (0001) basal plane. Here, the moments rotate 120° anticlockwise when hopping clockwise across a triangle, and 120° clockwise when hopping in the reverse direction—giving rise to an inverse triangular spin texture shown in Fig. 2.3(b).

The precise nature of the noncollinear order is influenced by multiple factors, including magnetocrystalline anisotropy (MCA), which imposes preferential spin alignment axes, and the competition between ferromagnetic (FM) and antiferromagnetic (AFM) exchange interactions. Additional contributions from Dzyaloshinskii–Moriya interactions (DMI) can further stabilize a diverse array of magnetic textures, including helical spin structures and (anti)skyrmions [32].

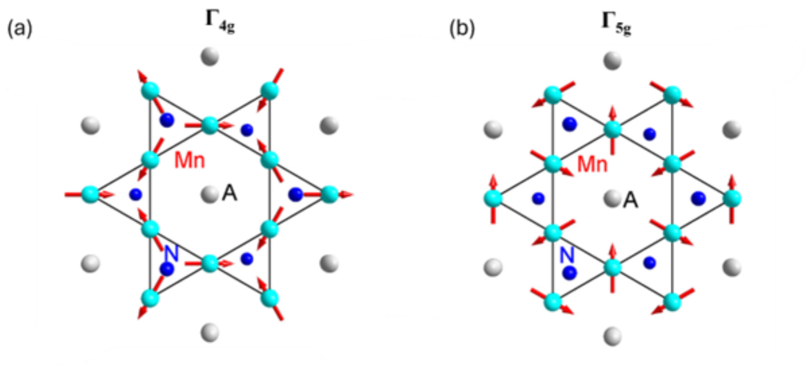

Figure 2.4.: Depiction of (a) Γ_{4g} and (b) Γ_{5g} phase in Mn_3NiN. With a 65% substitution of Ni with Cu, Γ_{4g} phase is stabilized up to 2 K. Adapted from [41]

One of the most remarkable phenomena in NCAFMs is the anomalous Hall effect (AHE) [4], which occurs even in the absence of net magnetization. The nontrivial spin structure on a kagome lattice induces a large Berry curvature in momentum space, giving rise to an AHE with Hall conductivities as high as $500\Omega^{-1}cm^{-1}$ at room temperature [33].

Recent studies have also demonstrated a nonconventional spin Hall effect (SHE) in NCAFMs. This effect has been attributed to symmetry-allowed skew scattering and chiral spin structures, rather than to conventional mechanisms relying on heavy metals [34, 13, 35]. These findings broaden the scope of efficient spin–charge interconversion mechanisms and suggest that NCAFMs could serve as both sources and detectors of spin currents in all-antiferromagnetic spintronic devices. A particularly rich material is Mn_3NiN [36], a cubic antiperovskite NCAFM, which not only exhibits the nontrivial transport properties like AHE [7, 37] like other NCAFM like Mn_3Sn but also a large piezomagnetic effect [38], magnetovolume [39], and barocaloric effects [40]. It exhibits the triangular spin arrangement as shown in Fig. 2.3(a). With the same chirality, there exist two different spin phases called Γ_{5g} and Γ_{5g} which differ by the simultaneous in-plane spin rotation (marked by the transformation in 2.3(a)). Below 180 K, Mn_3NiN hosts the Γ_{5g} phase, shown in Fig. 2.4(b) and between 180 K and up to 260 K (T_N) the Γ_{4g} phase, shown in Fig.2.4(a) which is more interesting owing to the necessary symmetry breaking that results in a host of nontrivial properties [31]. It has been shown that substituting Ni with Cu resulting in $Mn_3Ni_{0.35}Cu_{0.65}N$(Mn_3NiCuN from here on) results in the stabilization of the Γ_{4g} phase from 2 K up to $\approx$ 205 K, which is the modified TN due to the Cu substitution [7]. AHE has also been reported in Mn_3NiCuN despite a small net- magnetization of 3mμ_B/Mn [41].

The device potential of NCAFMs is underscored by recent demonstrations of all-antiferromagnetic tunnel junctions showing 70% tunneling magnetoresistance at room temperature in Mn_3Pt [42], and by field-free SOT switching in Mn_3Ir [43]. These results suggest a clear pathway toward ultrafast, high-density memory and logic elements that exploit the unique symmetry properties of antiferromagnetic spin order.

Looking forward, key challenges remain in realizing the full potential of NCAFMs. These include the experimental detection of orbital currents, the epitaxial integration of complex magnetic orders with semiconductor platforms, and the fine control of competing magnetic phases via strain or doping. Further opportunities lie in engineering critical fluctuations near magnetic phase transitions, which can be harnessed for adaptive torque control, and in exploring chiral edge modes in kagome AFMs for possible topological interconnects. Finally, the inherently ultrafast spin dynamics of these materials—often in the THz range—make them compelling candidates for beyond-CMOS, spin-based information processing architectures [29]. In conclusion, noncollinear antiferromagnets provide a fertile platform where topology, symmetry breaking, spin transport, and fluctuations coalesce into a versatile framework for both fundamental discoveries and applied spintronic technologies.

2.5. Symmetry and Hall Effects

The Hall effect encompasses a family of transverse voltage phenomena that arise when a current-carrying conductor is subject to a magnetic field or internal magnetic structure. The classical Hall effect, discovered by Edwin Hall[44] in 1879, is the basis for this family. In its simplest form, when a magnetic field B is applied perpendicular to a current-carrying conductor, charge carriers are deflected by the Lorentz force, resulting in a voltage transverse to both current and field — the Ordinary Hall Effect. The Hall voltage is linear in B, and its slope provides information on the carrier type and density. In magnetic materials, however, more complex transverse responses emerge, even in the absence of an external field [45]. These include (1) the Anomalous Hall Effect (AHE), which arises from the internal spin structure and spin–orbit coupling, and (2) the Planar Hall Effect (PHE), which emerges from anisotropic magnetoresistance when the magnetization lies in the plane of the sample. These effects can be understood and disentangled through symmetry analysis of the transverse Hall signal. When a magnetic field is swept in both positive and negative directions, the total transverse voltage V_{xy} (B) is typically decomposed into an antisymmetric component:

$$V_{xy}^{Anti-Sym.} = \frac{V_{xy}(B) - V_{xy}(-B)}{2}, \tag{2.26}$$

which captures all contributions odd in magnetic field, such as the ordinary Hall effect and AHE, and a symmetric component:

$$V_{xy}^{Sym.} = \frac{V_{xy}(B) + V_{xy}(-B)}{2}, \tag{2.27}$$

which contains components even in field, such as the Planar Hall Effect and other parasitic effects like anisotropic magnetoresistance (AMR) or thermal voltages from slight contact misalignments[46]. The Planar Hall Effect arises in materials with in-plane magnetization and results from the same anisotropic scattering mechanism responsible for AMR. Unlike the AHE, which exists even for out-of-plane magnetization and is associated with broken time-reversal symmetry, the PHE is purely a geometrical effect tied to the orientation between magnetization and current. Its magnitude depends on the angle ϕ between the current and magnetization.

2.5.1. The Anomalous Hall Effect

The Anomalous Hall Effect (AHE) is a transverse voltage generated in magnetic materials even in the absence of an external magnetic field. Unlike the ordinary Hall effect, which arises from the Lorentz force on charge carriers, the AHE is governed by the material's magnetic ordering and spin–orbit interaction. It serves as a direct probe of time-reversal symmetry (TRS) breaking and Berry curvature in the electronic band structure. Though traditionally associated with ferromagnets, recent discoveries have shown that AHE can also occur in NCAFMs, and more recently in collinear altermagnets [47], with zero net magnetization, provided certain symmetry conditions are met. The AHE was first recognized in the early 20th century in ferromagnets such as iron and nickel, where it was observed that the Hall voltage was orders of magnitude larger than could be explained by the Lorentz force alone [45]. In 1954, Karplus and Luttinger proposed a seminal theory that attributed the AHE to an anomalous velocity arising from the Berry phase acquired by electrons moving in spin–orbit coupled bands [48]. This was the first identification of a topological contribution to electrical transport. Their insight revealed that the Berry curvature $\vec{\Omega}_n(k)$ acts like a magnetic field in momentum space, producing a transverse velocity for the charge carriers:

$$v_{anomalous} = -\frac{e}{\hbar}\vec{E} \times \vec{\Omega}_n(k) \tag{2.28}$$

This intrinsic mechanism forms the backbone of our current understanding of the AHE in systems where band topology plays a crucial role.

Extrinsic Contributions: Skew Scattering and Side-Jump

While the Karplus–Luttinger mechanism explains the AHE in clean systems, extrinsic mechanisms also contribute, especially in disordered or metallic materials. Two prominent extrinsic effects are (1) Skew scattering, introduced by Smit [49], results from asymmetric scattering of spin-polarized electrons by impurities. It leads to a Hall resistivity component proportional to the longitudinal resistivity and (2) Side-jump scattering, proposed by Berger [50], arises from a lateral displacement of the electron wave packet during spin–orbit coupled scattering events. This effect scales quadratically with the longitudinal resistivity but is independent of impurity concentration.

AHE in Ferromagnets

In ferromagnets, the AHE is well established and widely observed. The presence of net magnetization, strong SOC, and broken TRS makes these systems ideal hosts for both intrinsic and extrinsic Hall effects. The Hall resistivity is often written as:

$$\rho_{xy} = R_0\vec{B} + R_S\vec{M}, \tag{2.29}$$

where R_0 is the ordinary Hall coefficient and R_s is the anomalous Hall coefficient. First-principles calculations incorporating Berry curvature have successfully reproduced experimentally observed AHE in elemental ferromagnets such as Fe, Co, and Ni, validating the intrinsic model and establishing AHE as a bulk band property [51].

AHE in Noncollinear Antiferromagnets

A major breakthrough in the field came with the prediction of a large AHE in NCAFM by Chen, Niu, and MacDonald in 2014 [4]. They showed that noncollinear magnetic order can act as a source of Berry curvature, provided the crystal symmetry does not cancel it out. This prediction was rapidly confirmed in experiments by Nakatsuji et al. (2015) [5] and Nayak et al. (2016) [6], who measured room-temperature AHE in Mn_3Sn and Mn_3Ge with conductivities comparable to ferromagnetic metals. Subsequently AHE was also observed in antiperovskite nitrides [7]. The magnetic order in these materials is often described not by a dipolar magnetization vector but by a cluster magnetic multipole, such as a magnetic octupole [52]. These multipoles serve as effective time-reversal breaking fields and can drive Hall currents in ways similar to net magnetization. The presence or absence of an AHE in a magnetic material is ultimately dictated by symmetry. For intrinsic AHE to exist, TRS must be broken (either explicitly or spontaneously), the space group must not force Berry curvature to integrate to zero over the Brillouin zone and no symmetry operation (like inversion, mirror, or combined TR) should cancel the anomalous velocity contributions [4, 31]. Thus, the emergence of AHE without net magnetization is a natural consequence of nontrivial magnetic symmetry and SOC. This principle underpins much of the interest in topological antiferromagnetic spintronics, where functional properties arise not from net moments but from symmetry-protected Berry phases.

2.5.2. Scalar spin chirality and Topological Hall Effect

Scalar spin chirality (SSC) and the topological Hall effect (THE) are two interconnected phenomena in condensed matter physics that arise due to noncoplanar spin textures in magnetic systems. SSC quantifies the geometric arrangement of spins, while THE is an observable transport phenomenon resulting from the interaction of conduction electrons with these textures. Despite their connection, distinguishing THE from SSC-driven effects is critical, as SSC does not always imply the presence of topologically nontrivial structures like skyrmions.

SSC is a geometric measure of non-coplanarity in a system of three spins S_i, S_j, S_k defined as:

$$\chi_{ijk} = \vec{S}_i \cdot (\vec{S}_j \times \vec{S}_k) \tag{2.30}$$

This geometric property generates real-space Berry curvature that influences electron transport [53]. While SSC is typically probed through neutron scattering [54], its most striking consequence manifests in conducting systems through emergent electromagnetic fields, which are effective gauge fields that arise from the geometric and topological properties of quantum states in condensed matter systems. Unlike fundamental electromagnetic fields, these are not tied to real charges but emerge from the collective behavior of electrons in solids, such as spin textures [55]. These arise from the Berry phase acquired by electrons traversing non-coplanar spin textures, creating synthetic magnetic fluxes [56]. However, the SSC alone does not guarantee observable transport signatures—it requires coupling to itinerant electrons to produce effects that can be observed as part of the Hall conductivity [8] .

$$\sigma_{xy}^{Anti-Sym.} = \gamma_{\mathrm{Oct}} \left[\vec{Q}_{T_{1g}}\right]_z + \gamma_{\mathrm{dip}} \left[\vec{M}_{T_{1g}}\right]_z + \gamma_{\mathrm{SSC}} \left[\sum_{ijk} \vec{S}_i \cdot (\vec{S}_j \times \vec{S}_k)\right] \tag{2.31}$$

The topological Hall effect (THE) appears as an additional contribution to the Hall resistivity when electrons couple to non-coplanar spin textures [57]. Distinct from ordinary and anomalous Hall effects, THE scales with the net emergent flux and typically peaks where spin chirality is maximized. While often associated with skyrmions, THE can also arise in other non-coplanar systems.

Non-trivial features in the transverse Hall signal are often attributed to the THE, which arises from non-trivial topological structures such as magnetic skyrmions [58]. However, several studies have highlighted that attributing such features solely to the THE requires specific conditions to be met, and simplistic attributions can be incorrect [59, 60, 61]. In many cases, non-trivial transverse Hall signals can emerge from two-channel sources of the anomalous Hall effect (AHE) with opposing Hall conductivity factors. This phenomenon is particularly relevant in bilayer systems, such as those composed of oxides of Sr [62, 63, 64]. In such systems, the two channels may manifest in the AHE signal as one hysteretic channel and one non-hysteretic channel, resulting in the observed non-trivial shapes of the AHE curves. In contrast to these systems, centrosymmetric NCAFMs like Mn_3NiCuN, do not exhibit these characteristics as their structure precludes the formation of topologically non-trivial structures with a fixed chirality like skyrmions, and it is not known to support multiple AHE channels as seen in bilayer systems.

2.6. Magnetization Dynamics and the Orbital Hall Effect (OHE)

Understanding the time evolution of magnetization is essential for modelling modern spintronic phenomena. The dynamics of magnetization under applied magnetic fields and currents are governed by the Landau–Lifshitz–Gilbert (LLG) equation, which describes how the magnetization vector precesses and relaxes over time [65]. In addition to external magnetic fields, spin-polarized currents can exert torques on the magnetization, giving rise to current-induced magnetization dynamics. These torques fall into two main categories: the spin-transfer torque (STT) and the spin–orbit torque (SOT). More recently, phenomena such as the orbital Hall effect (OHE) have expanded the theoretical framework of electrically driven magnetization control in magnetic and nonmagnetic systems [66, 67].

2.6.1. Landau–Lifshitz–Gilbert Equation

The LLG equation forms the foundation of micromagnetic dynamics. It describes how the magnetization vector M precesses around an effective magnetic field $\vec{H}_{eff}$, while also experiencing a damping torque that aligns it with the field. The equation is expressed as:

$$\frac{d\vec{M}}{dt} = -\gamma \vec{M} \times \vec{H}_{\text{eff}} + \alpha M_S \left(\vec{M} \times \frac{d\vec{M}}{dt} \right) \tag{2.32}$$

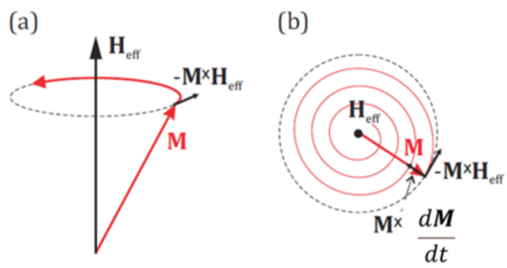

Figure 2.5.: Schematic illustration of the magnetization dynamics in an effective magnetic field $\vec{H}_{eff}$. The precession only leads to a continuous rotation as shown in (a), while the damping slowly aligns the magnetization with the field, resulting in a spiralling motion shown in (b).

Here, γ is the gyromagnetic ratio, α is the dimensionless Gilbert damping parameter, and M_S is the saturation magnetization. A schematic of the dynamics is shown in Fig. 2.5. The first term captures the torque due to precession, while the second accounts for energy dissipation. The LLG framework is central to micromagnetic simulations and describes both ferromagnetic and antiferromagnetic dynamics.

2.6.2. Spin–Orbit Torques (SOTs)

Spin–orbit torques (SOTs) refer to a class of current-induced torques that enable electrical control of magnetization without the need for spin-polarized currents from a reference magnetic layer. They arise from the interplay between charge transport and spin–orbit coupling (SOC) in systems with broken inversion symmetry, either in the bulk or at interfaces [68, 69]. Unlike spin-transfer torques (STTs), which rely on spin accumulation generated via ferromagnetic injection, the SOTs are generated intrinsically by the flow of charge in spin-orbit-coupled media. SOTs play a critical role in modern spintronic technologies such as the spin–orbit torque magnetic random access memory (SOT-MRAM), racetrack memories, and ultrafast switching devices [70, 71].

Two principal microscopic mechanisms underpin SOTs: the spin Hall effect (SHE) and the inverse spin galvanic effect (iSGE). While both mechanisms originate from SOC, they differ in their physical origin, geometry, and symmetry constraints. The SHE generates spin currents in the bulk of a nonmagnetic layer, which diffuse into the adjacent magnetic layer to exert torques as shown in Fig. 2.6(a). In contrast, the iSGE operates at interfaces with broken inversion symmetry, where a charge current induces a non-equilibrium spin density directly at the magnetic interface shown in Fig. 2.6(b). Understanding the relative contribution and symmetry of these two mechanisms is essential for interpreting experimental torque efficiencies and designing optimized spintronic devices [72, 73].

Spin Hall Effect (SHE)

The spin Hall effect is a bulk transport phenomenon in which an applied charge current gives rise to a transverse spin current, either via extrinsic skew scattering and side-jump mechanisms or through intrinsic band structure effects such as Berry curvature [3, 12]. First proposed theoretically by Dyakonov and Perel in the 1970s and reformulated in the modern framework by Hirsch [74], the SHE manifests strongly in nonmagnetic materials with significant spin–orbit interaction, such as Pt, W, and Ta. When a charge current j_C flows through such a material, a transverse spin current is generated with spin polarization $\vec{\sigma}$, resulting in spin accumulation at interfaces. In layered systems, this spin current diffuses into an adjacent magnetic layer, exerting a damping-like torque on the magnetization:

$$\vec{\tau}_{DL} \propto \vec{M} \times (\vec{\sigma} \times \vec{M}) \tag{2.33}$$

The efficiency of this process is governed by the spin Hall angle θ_{SH}, which quantifies the conversion efficiency from charge to spin current [3]. The SHE is responsible for robust and reproducible damping-like torques in heavy metal/ferromagnet heterostructures and remains the most experimentally accessible mechanism for SOT generation.

Inverse Spin Galvanic Effect (iSGE / Rashba–Edelstein Effect)

The inverse spin galvanic effect (iSGE), also known as the Rashba–Edelstein effect, is an interfacial phenomenon that occurs in systems with broken inversion symmetry and finite spin–orbit coupling. Here, a charge current induces a non-equilibrium spin density (spin polarization) at the interface, without the need for spin current flow [75, 76]. This spin accumulation acts as an effective magnetic field that can exert both field-like and damping-like torques on the local magnetization:

$$\vec{\tau}_{FL} \propto \vec{M} \times \vec{\sigma} \tag{2.34}$$

The iSGE is particularly important in systems with strong Rashba SOC, such as asymmetric quantum wells, topological insulators, or single layer non-centrosymmetric magnets. Because the spin polarization is induced directly at the interface, the resulting torque can be large and highly sensitive to interfacial structure and symmetry [72, 73]. Importantly, the iSGE can produce torques even in single-layer magnetic systems and

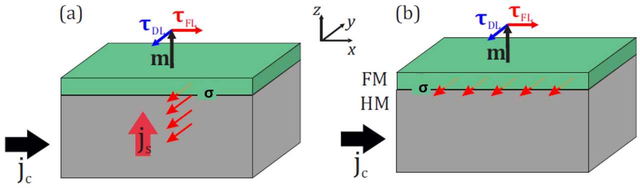

Figure 2.6.: Two main models of spin-charge conversion mechanisms at the HM/FM interface. (a) SHE: an electric current through the bulk of the HM layer results in the generation of a transverse spin current, with the spin being perpendicular to the plane of both current. (b) iSGE: an electric current through the interface between HM and FM layer experiences a Rashba field via the SOC under the structural inversion asymmetry, which results in a spin accumulation near the interface. $\vec{\sigma}$ indicates the spin polarization direction. Both mechanisms produce DL and FL torques acting on the magnetization of the FM layer. Adapted from [68]

can operate independently or in concert with the SHE. In systems like Mn_2Au, CuMnAs, and certain noncollinear antiferromagnets, iSGE-derived torques are critical for field-free magnetization switching and offer a pathway for symmetry-driven device engineering [77].

2.6.3. Orbital Hall Effect

The orbital Hall effect (OHE) refers to the generation of a transverse flow of orbital angular momentum (OAM) in response to an applied electric field, independent of spin–orbit coupling (SOC). Unlike the spin Hall effect (SHE), which requires SOC to convert charge currents into transverse spin currents, the OHE can arise purely from the orbital character of electronic wave functions and their motion through crystalline potentials. This effect originates from the orbital Berry curvature in momentum space and the cycloidal real-space motion of electronic wave packets—even in systems where the electronic states are dominated by ss-orbitals. Recent theoretical and experimental work has firmly established the OHE as a cornerstone of orbitronics, a growing field focused on the use of orbital degrees of freedom in solid-state systems for low-dissipation information transport and spin–orbit torque generation. Notably, the OHE has been observed in materials with weak SOC, such as titanium, opening pathways to angular momentum control without relying on heavy elements [10, 78, 79].

The OHE originates from the momentum-space geometry of Bloch states, specifically from the orbital Berry curvature. For a given Bloch state $|u_{nk}\rangle$, the orbital Berry curvature tensor associated with the OAM component $L_\gamma$is given by [11]:

$$\vec{\Omega}^{L_\gamma}_{n,\alpha,\beta}(\vec{k}) = -2\,\mathrm{Im}\sum_{m\neq n}\frac{\langle u_{nk}|\,\hat{v}_\alpha\,|u_{mk}\rangle\,\langle u_{mk}|\,\hat{L}_\gamma\,|u_{nk}\rangle}{(E_{nk}-E_{mk})^2} \tag{2.35}$$

Here, $\hat{v}_\alpha$ is the velocity operator in direction α, and L_γ is the orbital angular momentum operator along direction γ. This expression closely mirrors that of the spin Berry curvature in the spin Hall effect, but crucially, SOC is not required for the OHE to arise. Instead, the effect is driven by interband matrix elements involving OAM and velocity operators. The orbital Hall conductivity (OHC) is computed by integrating the orbital Berry curvature over the Brillouin zone, and its magnitude depends on the interatomic electronic structure—including hopping terms and crystal symmetry. One of the most compelling demonstrations of the OHE is the direct observation in elemental titanium, a light metal with negligible SOC. Using magneto-optical Kerr effect (MOKE) measurements, Choi et al. observed OAM accumulation at the surfaces of Ti, with orbital diffusion lengths exceeding 70 nm—an order of magnitude longer than typical spin diffusion lengths in heavy metals [78]. Further evidence for the OHE has emerged from orbital-resolved photoemission experiments, which confirmed that orbital accumulation can occur independently of ferromagnetic layers, suggesting a robust and intrinsic orbital transport mechanism. These results confirm theoretical predictions that OAM currents can propagate over long distances and be manipulated by electric fields without relying on spin degrees of freedom [78]. The integration of the OHE into spin–orbit torque (SOT) devices has also seen progress. Recent proposals suggest that orbital currents injected into a magnetic layer can generate both damping-like and field-like torques via interfacial spin–orbit conversion, offering a new channel for magnetization control in systems where conventional SHE-based mechanisms are inefficient [79].

The emergence of the OHE fundamentally reshapes the understanding of angular momentum transport in solids. Its independence from SOC makes it particularly attractive for applications in light-element-based spintronic devices, where reduced resistive losses and longer diffusion lengths offer performance advantages. As orbitronics continues to evolve, the OHE is expected to play a pivotal role in nonvolatile memory, ultrafast logic, and topological quantum systems. Furthermore, the OHE offers exciting opportunities for synergy with noncollinear antiferromagnets, where spin and orbital fluctuations near criticality can enhance orbital transport phenomena. With ongoing developments in orbital imaging and manipulation, the OHE provides a powerful conceptual and practical framework for next-generation angular momentum electronics.

3. Methods

3.1. Structural Characterization via X-ray Diffraction

Structural properties of thin films were characterized using high-resolution X-ray diffraction (XRD) on a Bruker D8 Discover diffractometer equipped with a Cu $K\alpha$ source and a Ge(220) monochromator.

XRD is a non-destructive technique used to probe the crystalline structure of materials by analyzing the diffraction of X-rays from periodically spaced atomic planes[80]. The method is based on Bragg's law, which defines the condition for constructive interference of X-rays reflected from different crystallographic planes:

$$2d \sin\theta = n\lambda \tag{3.1}$$

Here, d is the interplanar spacing, θ is the incident angle, λ is the X-ray wavelength, and n is the diffraction order. By analyzing the angular position and intensity of the diffracted beams, one can extract information about lattice parameters, crystal orientation, and degree of structural order.

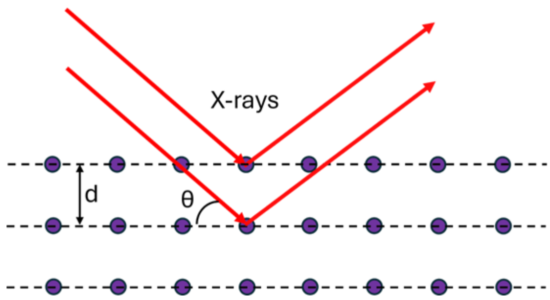

Figure 3.1.: Schematic of an X-ray beam (red lines) interacting with the atoms (purple). The angle between the plane of atoms and the X-ray beam is defined as θ. The distance between scattering planes (horizontal lines) is named d.

3.1.1. $2\theta - \omega$ Scan

The $2\theta - \omega$ (or coupled) scan is used to determine the out-of-plane orientation of the crystal structure and identify the phases present in the sample. In this geometry, both the incident and detector angles are swept simultaneously to probe lattice planes parallel to the substrate surface. The angular positions of diffraction peaks are used to calculate lattice constants and the crystallographic phase.

3.1.2. Rocking Curve (ω Scan)

Rocking curves are recorded to assess the mosaic spread along the film's growth direction. Mosaic spread is a measure used in crystallography to describe the angular distribution of orientations of small, perfectly ordered regions (crystallites or domains) within an otherwise imperfect crystal. Rather than being a single, perfectly aligned lattice, a real crystal often consists of many such domains, each slightly misaligned with respect to its neighbors [80].In an ω-scan, the detector is held fixed at a chosen Bragg angle while the sample is rocked in small angular steps. The full width at half maximum (FWHM) of the resulting peak provides a measure of the angular distribution of crystallites, reflecting strain, grain tilt, and vertical alignment.

3.1.3. ϕ- Scan

ϕ scans are performed to evaluate in-plane crystallographic alignment and epitaxial relationships. During this scan, the sample is rotated azimuthally (ϕ) at a fixed incident and diffraction angle, usually targeting asymmetric reflections. The symmetry and periodicity of the resulting diffraction peaks provide insight into the in-plane orientation of the film relative to the substrate and reveal twinning, rotational domains, or epitaxial mismatch.

3.2. Superconducting Quantum Interference Device

The magnetic properties of the thin films are characterized using a Superconducting Quantum Interference Device (SQUID) magnetometer, specifically a Quantum Design MPMS XL 5 system. SQUID magnetometry is one of the most sensitive techniques available for detecting absolute values of magnetic moments, capable of measuring signals as low as 10^{-8} emu [81]. It operates on the principle of quantum interference of Cooper pairs in a superconducting loop containing Josephson junctions [82]. A schematic of the gradiometer coils in shown in Fig. 4.2. A change in the magnetic flux

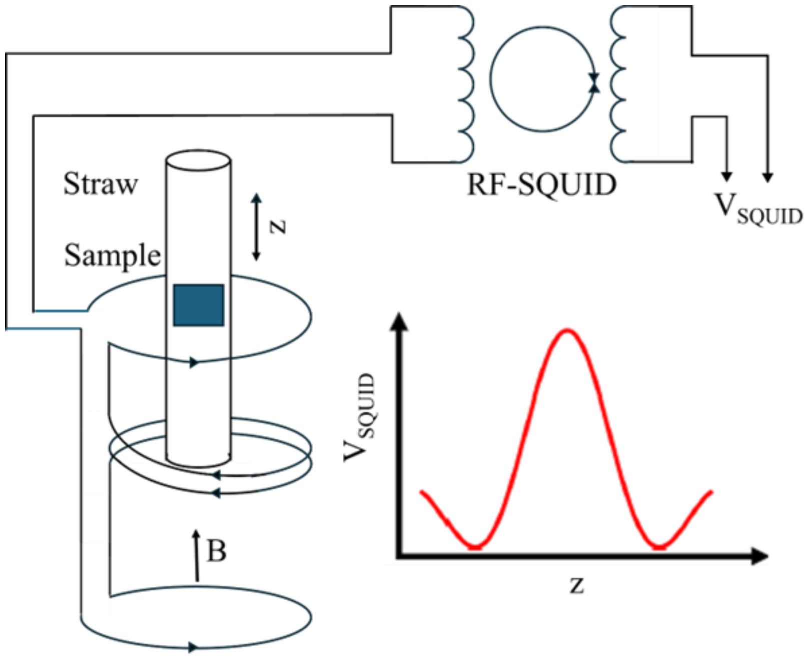

Figure 3.2.: Schematic depiction of a SQUID magnetometer with second order gradiometer pickup coils and a typical signal of a sample under displacement along z.

linked to the superconducting pickup coils induces a current, which is measured as a voltage signal correlated with the sample's magnetization.

To study thermal magnetic behaviour and identify phase transitions, temperature-dependent magnetization measurements were performed. The sample was cooled to cryogenic temperatures and magnetization was measured while warming under a small applied field. For the field dependence, magnetization versus field (M–H) loops were acquired at selected temperatures by sweeping the magnetic field typically between. The applied field could be oriented either in-plane or out-of-plane relative to the sample surface, allowing the evaluation of coercivity, remanent magnetization, saturation magnetization, and magnetic anisotropy.

3.3. Device Fabrication

For the experiments described in this work, sputtered thin films were patterned into a range of device geometries. These included cross-shaped structures to control current flow and geometry to perform ST-FMR with fixed probe dimensions. The general patterning workflow follows a four-step lithographic process, based on methods described in Ref. [83]

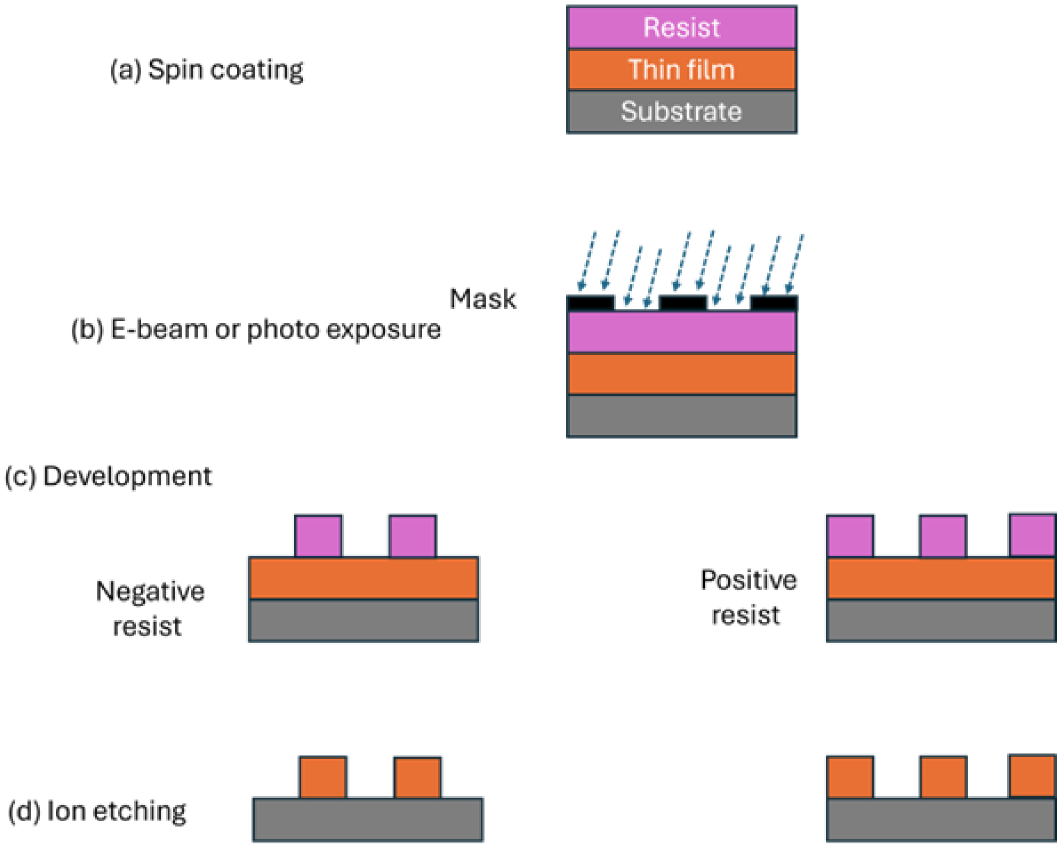

Figure 3.3.: Different steps of the patterning process using a primitive manual mask are depicted. In modern fabrication tools, the optics is focussed on the sample based on a mask software. After the (a) spin coating and (b) exposure (b) of the photoresist, the resist is (c) developed. Depending on the type of the resist, negative or positive, different final structures can be produced by (d) ion beam etching.

First, the samples undergo multistep cleaning to remove organic and particulate contaminants. Then, a radiation-sensitive polymer (photoresist) is applied to the surface of the thin film stack. A few drops of photoresist are dispensed on the surface and spin-coated to ensure uniform thickness. The coated sample is then baked on a hot plate to evaporate any residual solvent and promote adhesion. In the second step, the desired pattern is transferred to the resist layer via exposure. In optical lithography, a chromium-patterned mask is aligned with the sample and illuminated with UV light from a mercury vapor lamp, causing photochemical reactions in the exposed resist areas. Additionally, an automatic pattern transfer by MicroWriter ML 3 was also used for fabrication. In electron beam lithography, a focused electron beam writes the pattern directly onto the resist according to predefined designs, enabling higher-resolution features. The third step involves developing the exposed resist. Depending on the type of resist used, development removes either the exposed regions (positive resist) or the unexposed regions (negative resist), thus creating a patterned resist mask on the surface. In the final step, the patterned resist serves as a mask for subsequent processing. In the case of etching, inert Ar+ ions are used to selectively remove the unprotected regions of the thin film. Alternatively, material (e.g., metal for markers or contacts) can be deposited into the exposed areas followed by lift-off in acetone, leaving behind the deposited structure only where the resist had been removed. This flexible process allows for both additive and subtractive fabrication steps to define a wide variety of thin-film devices.

3.4. Magnetotransport measurements in a cryostat

Magnetotransport measurements were performed to investigate field-dependent electrical transport properties such as the anomalous Hall effect (AHE), planar Hall effect (PHE), and related spintronic responses [8, 45]. These experiments were conducted using a high-field, variable-temperature cryostat system equipped with a piezo-controlled rotatable sample stage (attocube ANRv51), enabling angle-dependent Hall measurements. The cryostat utilizes liquid helium (LHe) cooling, allowing for temperatures as low as 2.4 K to be reached. A superconducting magnet coil, submerged in the LHe reservoir, provides fields up to 15 T. To access a wide temperature range, a variable temperature insert (VTI) is integrated into the cryostat. The VTI is an evacuated region into which helium gas from the reservoir is drawn via a needle valve. Temperature control is achieved by regulating the flow of helium into the VTI and applying localized heating at the gas inlet. This configuration allows precise and stable control of sample temperature between 2.4 K and 300 K. The cryostat itself is vacuum-insulated to maintain thermal isolation from ambient conditions and preserve helium efficiency. Additionally, the heater and temperature sensor on the sample rod close to the sample allows for precise sensing and control of sample temperature. The patterned Hall bar samples were mounted on a gold-contacted printed circuit board (PCB) using PMMA as an adhesive and wire-bonded using a TPT Hybond 572-40 wire bonder. The PCB was then affixed to the rotator head and inserted into the cryostat. Depending on the sample stage, precise out-of-plane or in-plane rotation with respect to the magnetic field direction was allowed, enabling systematic angular sweeps. A DC current was sourced through the longitudinal arms of the Hall bar using a Keithley 2400 source meter, and the transverse Hall voltage was measured using a Keithley 2182A nanovoltmeter. All measurements were performed with current levels carefully chosen to minimize Joule heating effects, and the data were typically averaged over current injections to improve signal-to-noise ratio. At each measurement angle, the external magnetic field was swept symmetrically (typically from −15 T to +15 T) while recording the transverse voltage V_{xy} . After each field sweep, the sample was rotated to the next angular position, usually in increments of $\phi = 15°$. This procedure was repeated

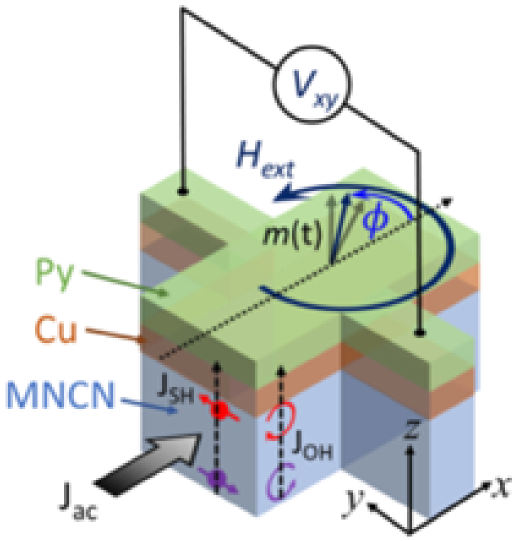

Figure 3.4.: Schematic of the SHH measurement procedure. H_{ext} is swept in the sample plane while measuring the transverse voltage (V_{xy}) from the applied J_{ac}.

across a range of temperatures, enabling a comprehensive angular and temperature-dependent study of the magnetotransport behaviour. These measurements formed the basis for extracting the anomalous Hall signal and angular symmetry features.

3.5. Second Harmonic Hall method

To quantify spin-orbit torques (SOTs), we adopt the well-established method of second harmonic Hall (SHH) method [84, 85, 86], performed in a three-dimensional vector magnet cryostat capable of generating magnetic fields up to 5 T out-of-plane (OOP) and 1 T in-plane (IP). These measurements were carried out across a temperature range from 4 K to 300 K, with angular control of the external magnetic field H_{ext} around the in-plane and out-of-plane directions. A low-frequency AC current is applied to the Hall bar, and the resulting transverse voltages at the first ($V_{1\omega}$) and second harmonic ($V_{2\omega}$) frequencies were measured using a lock-in amplifier. While $V_{1\omega}$ captures the conventional Hall and magnetoresistive responses, $V_{2\omega}$ contains signatures of spin-orbit torque-induced magnetization oscillations and possible thermal contributions.

Spin-orbit torques generate two distinct components – in-plane damping-like torque (DLT), $\tau_{DL} \propto m \times (\sigma \times m)$ where m is the unit vector of Py magnetization and σ is generated by angular momentum from SHE and/or OHE. For the DLT, the equivalent current-induced effective spin-orbit field (SOF), H^z_{DL} deflects the magnet out of the plane, creating an oscillation in the resistance due to AHE. (2) Out-of-plane field-like torque (FLT), $\tau_{FL} \propto m \times \left(H^{Oe}_{FL} + H^{Y}_{FL}\right)$ where H_{Oe} is the oersted field generated by the conductive shunting layers and H^y_{FL}corresponds to interfacial SOF [87]. FLT from H^{Oe}_{FL} deflects the magnet in the sample plane, resulting in oscillating resistance due to the planar Hall effect (PHE). The mixing of the oscillating applied current and oscillating resistance produces $V_{2\omega}$, which can be expressed as:

$$V_{2\omega} = C_A \cos\phi + C_P \cos\phi \cos 2\phi \tag{3.2}$$

where

$$\begin{aligned} C_P &= -\left(H^{Oe}_{FL} + H^{Y}_{FL}\right) \frac{V_P}{H_{ext}} + C_0 \\ C_A &= -H^{Z}_{DL} \frac{V_A}{2\left(H_{ext} + H_{\perp}\right)} + V_{ANE} + V_{ONE} H_{ext} \end{aligned} \tag{3.3}$$

V_{ANE} and V_{ONE} are the strength of anomalous Nernst effect (ANE) and ordinary Nernst effect (ONE), respectively [88], which are generated due to the unintentional out-of-plane thermal gradient that is coupled to the in-plane magnetization of the ferromagnet and H_{ext} respectively [89]. V_P is the coefficient of the PHE voltage,$V_{PHE} = V_P \sin 2\phi$ where ϕ is the angle between applied current and magnetization in the sample plane (xy plane). V_P is determined by measuring $V_{1\omega}$ while rotating H_{ext} in the plane. V_A is the coefficient of the AHE voltage, $V_{AHE} = V_A \cos\theta$ where θ is the angle between the magnetization and out-of-plane z-axis. The coefficient V_A is obtained from $V_{1\omega}$ while sweeping H_{ext} out of the plane. The same measurement also provides us with the information of $H_{\perp}$, the out-of-plane demagnetization field.

3.6. Spin-Torque Ferromagnetic resonance (ST-FMR)

Spin-torque ferromagnetic resonance (ST-FMR) was used as a complementary technique to second harmonic Hall measurements for quantifying spin-orbit torques (SOTs) [90, 91]. Unlike SHH, which is a time-domain measurement, ST-FMR operates in the frequency domain and probes magnetization dynamics under microwave-frequency excitation. This technique allows simultaneous extraction of both damping-like and field-like torque components through lineshape analysis of the resonance signal.

The measurements were performed at room temperature on lithographically patterned bar-shaped devices composed of heavy metal/ferromagnet bilayers shown in Fig. 3.5. In a typical configuration, a microwave-frequency current was applied along the device using a vector network analyzer or a signal generator via an RF probe. The current generates both an Oersted field and a spin current via the spin Hall effect (or orbital

Figure 3.5.: Microscopic image of a device to perform the ST-FMR measurement. The large area in gold represents the gold contact pads for the RF probes. The small bar attached to the two pads is the material being probed.

Hall effect) in the heavy metal layer. The spin current exerts torques on the magnetization of the ferromagnetic layer, driving precessional motion when the applied magnetic field satisfies the resonance condition. The external magnetic field was applied in the plane of the sample at 45° to the current direction to enable detection of both symmetric and antisymmetric voltage components. As the magnetization precesses, the device resistance oscillates due to anisotropic magnetoresistance (AMR). The mixing of the RF current and the time-varying resistance produces a DC voltage signal known as the mixing voltage, which is measured using a nanovoltmeter or lock-in detection with amplitude modulation. The measured DC mixing voltage $V_{mix}(H)$ as a function of the applied magnetic field H is typically fit to a combination of symmetric and antisymmetric Lorentzian functions:

$$V_{\mathrm{mix}}(H) = S\frac{\Delta H^2}{(H - H_{\mathrm{res}})^2 + \Delta H^2} + A\frac{\Delta H\,(H - H_{\mathrm{res}})}{(H - H_{\mathrm{res}})^2 + \Delta H^2} \tag{3.4}$$

Where H_{res} is the resonance field, δH is the full width at half maximum (FWHM) of the resonance, S and A are the amplitudes of the symmetric and antisymmetric components. The symmetric component S is primarily attributed to the damping-like torque, while the antisymmetric component A includes contributions from the Oersted field and possible field-like torques [92]. By analyzing the frequency dependence of H_{res}, the effective magnetization and gyromagnetic ratio can be extracted. Furthermore, the ratio S/A provides a direct measure of the relative strengths of the spin-orbit torque contributions, allowing for estimation of spin Hall angle or torque efficiency. This frequency-domain method provides a robust and complementary validation of spin-torque effects observed in DC and harmonic Hall measurements.

4. Anomalous Hall Effect in $Mn_3Ni_{0.35}Cu_{0.65}N$

The anomalous Hall effect (AHE) has long been considered a hallmark of ferromagnetic materials, arising from the interplay between broken time-reversal symmetry and spin–orbit coupling (SOC) [8, 3]. In conventional ferromagnets, the magnitude of the AHE is proportional to the net magnetization, reflecting the alignment of spins along a single direction. However, recent discoveries have expanded the scope of the AHE to include certain classes of noncollinear antiferromagnets (NCAFMs) [4, 5, 93], where complex spin textures break time-reversal symmetry (TRS) locally without producing a net magnetic moment.

In these systems, Berry curvature arising from the chiral spin configuration acts as an effective magnetic field in momentum space, giving rise to a sizable anomalous Hall response [8]. Notably, in materials such as Mn_3Sn and Mn_3Ge, the observed AHE cannot be explained by their weak net magnetization alone [5, 6, 94]. This highlights the possibility of higher-order multipolar contributions—such as octupolar moments—governing the transport properties.

Despite these advances, most experimental investigations have been limited to conventional measurement geometries, where the magnetic field is applied perpendicular to the sample plane and the current is driven in-plane. Such configurations entangle any novel contributions to the Hall signal with conventional dipolar magnetization effects, making it challenging to isolate the true origin of the AHE. A comprehensive understanding of the mechanisms responsible for the AHE thus requires a systematic investigation of the Hall response under varied magnetic field orientations, probing the symmetry of the signal across different directions in space.

In parallel, scalar spin chirality (SSC), arising from noncoplanar spin arrangements, has been proposed as an additional source of Hall responses [57]. SSC-induced contributions can coexist with higher-order multipolar effects and offer further complexity

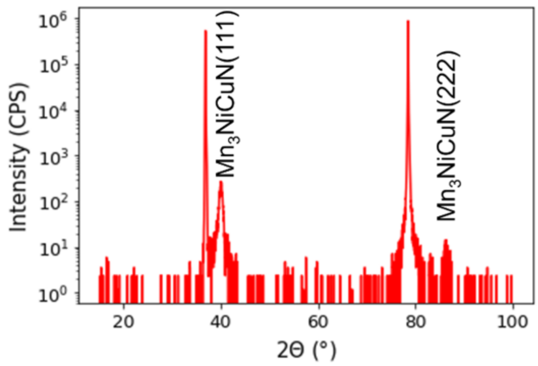

Figure 4.1.: X-ray diffraction pattern showing the sharp MgO (111) substrate peak, closely followed by the Mn_3NiCuN peak, confirming alignment of the OOP direction of the substrate and the thin film.

to the transport behavior in such systems. In this chapter, we address these key questions by performing angle-dependent AHE measurements in the noncollinear antiferromagnet $Mn_3Ni_{0.35}Cu_{0.65}N$ (Mn_3NiCuN).

4.1. Sample characterization

X-ray diffraction was performed on the MgO(111)/Mn_3NiCuN/Pt sample, as shown in Fig.4.1. Sharp diffraction peaks are observed at approximately 39° and 78°, corresponding to the (111) and (222) reflections of the MgO substrate, respectively. In addition, two relatively intense peaks attributed to the Mn_3NiCuN (111) and (222) planes appear in close alignment with the substrate peaks, as indicated in the figure.

Using a SQUID magnetometer, the magnetic characterization of Mn_3NiCuN was performed. Magnetic hysteresis of the sample was performed as a function of $\vec{H}$ along the [111] direction. The paramagnetic background from the substrate was subtracted and the resulting signal shown in Fig 4.2. The magnetization at saturation is about 0.026 μ_B/Mn atom.

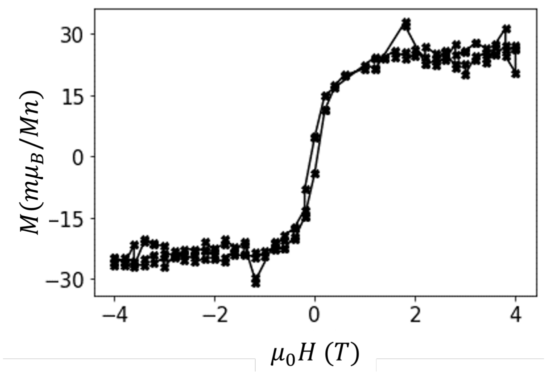

Figure 4.2.: Magnetic Hysteresis showing weak magnetization when $\vec{H}$ is swept along [111]

4.2. Hall measurements on MgO(111)/Mn_3NiCuN/Pt thin film

Hall measurement was performed as described in 3.4. As a first confirmation, a $\vec{H}$ was applied perpendicular to the sample plane (hereafter OOP configuration), and the transverse voltage was measured. Fig.4.3 shows the R_{xy} as a function of $\vec{H}$ for 10 K and 230 K. As can be seen, there is a clear AHE at 10 K, characterized by the switching of the R_{xy} at $\vec{H} \approx 2$ T, eventually saturating close to 5 T. This temperature is well below the reported T_N of this material [41]. As a comparison, the resultant R_{xy} for 250 K, which is above the T_N is plotted in orange, showing that the AHE vanishes at this temperature. This indicates that the observed AHE at 10 K originates from the NCAFM order below the $T_N \approx 210$ K. We can further calculate the AH conductivity of our sample by using the following equation

$$\sigma_{\mathrm{xy}} = -\frac{\rho_{\mathrm{xy}}}{\rho_{\mathrm{xx}}^2} \tag{4.1}$$

, where ρ_{xx} is the longitudinal resistivity and ρ_{xy} the Hall resistivity. From our measurement, for a film thickness of 20 nm and $\rho_{xx} \approx 150 \mu\Omega cm$ this yields 15 S/cm at 10 K. A detailed comparison of σ_{xy} of different NCAFMs, and some FM is presented in the A.2.

Next, we apply a magnetic field in the sample plane and acquire the Hall signal. The AH curve after data processing (see A.1) is shown in Fig.4.4. From the figure, we can again see an AHE switching with the applied $\vec{H}$. It has to be emphasized that the observation AHE with $\vec{H}$ in the plane is significant. This is a direct observation of AHE in an NCAFM with no contribution from the ferromagnetic magnetization. We are able to discard the ferromagnetic contribution by the clever use of geometry whereby our Hall measurement is only sensitive to the OOP magnetization, which can

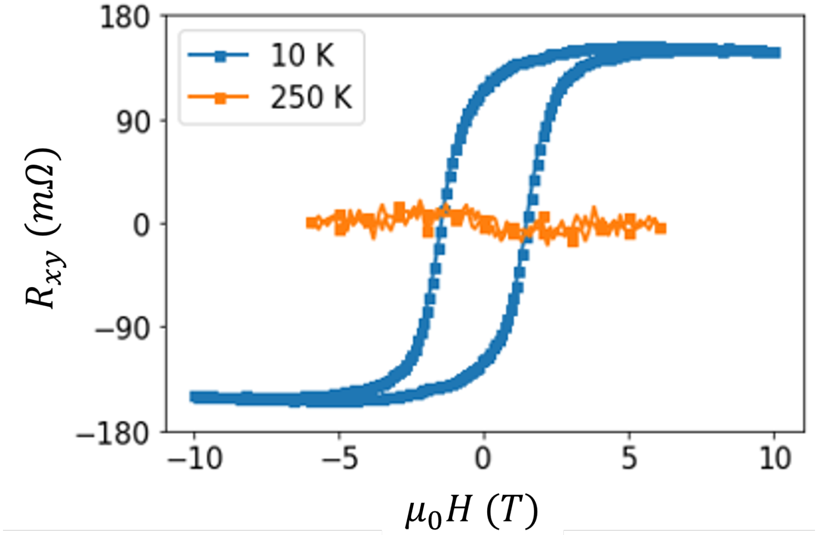

Figure 4.3.: Anomalous Hall effect signal in Mn_3NiCuN when $\vec{H}$ is swept out of plane along [111]

be ruled out as a result of the sizeable $\vec{H}$ we apply in the plane. With this technique, there is no need to speculate on the possible ferromagnetic contribution to the AHE and one can conclusively assert its origins in the noncollinear antiferromagnetic spin order.

This shows a direct confirmation that AHE in NCAFM arises without a ferromagnetic moment, as any induced magnetization from $\vec{H}$ along the plane strictly does not contribute to the AHE, which is measured in the symmetry of the system.

This observation motivates a closer investigation into the parameters governing the AHE and their interaction with the in-plane $\vec{H}$. To gain further insights, systematic field sweeps, like the one shown in Fig. 4.4 were performed at angular increments of $\phi = 15°$. The resulting angular dependence, particularly its symmetry, may provide clues regarding the underlying mechanism responsible for the in-plane AHE observed in this system.

To acquire a robust data set and to avoid any effects due to local inhomogeneities, we performed the measurements on two Hall devices. Further, the measurements were repeated after warming up to room temperature and re-cooling to 100 K to obtain a comprehensive data set. The averaged values of all data are plotted in Fig. 4.5. One immediately notices a sinusoidal behavior of the data points. This was confirmed

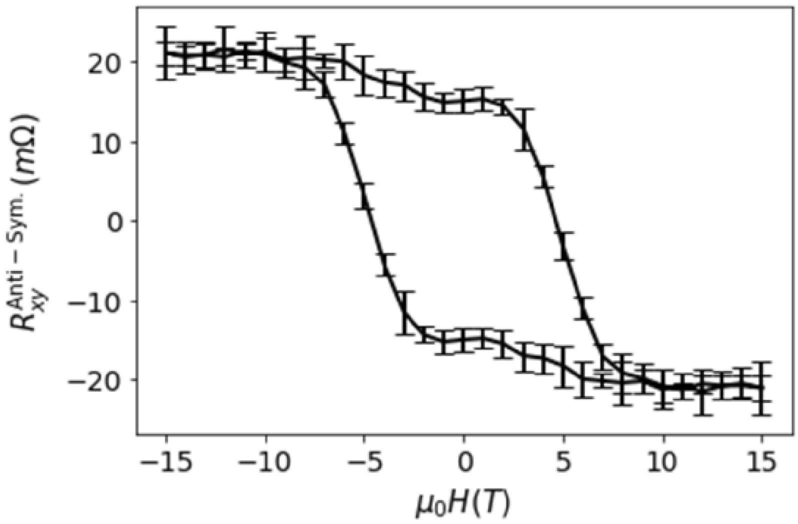

Figure 4.4.: Anti-symmetrized R_{xy} as a function of $\vec{H}$ applied along the (111) plane.

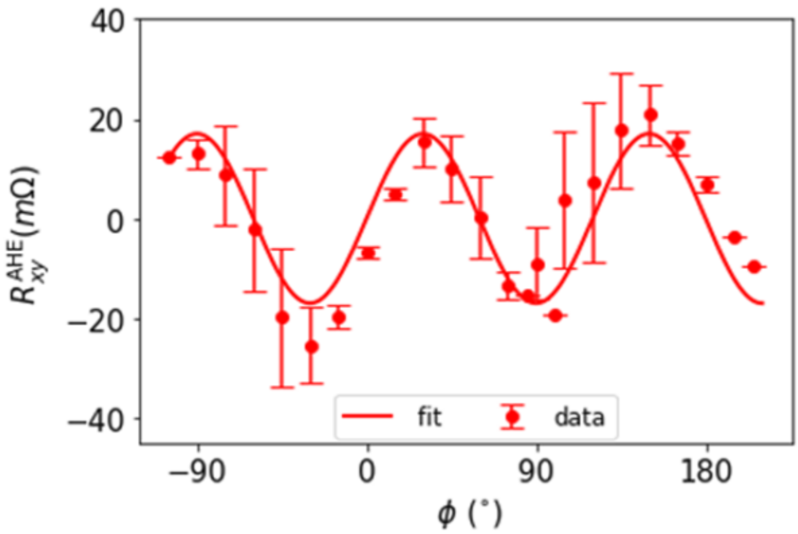

Figure 4.5.: R_{xy}^{AHE} (15 T) as a function of the $\vec{H}$ direction ϕ in the (111) plane. Dots represent the experimental data points, while the solid curve is a sinusoidal fit with 3-fold symmetry.

when a sinusoidal function of 120° periodicity was plotted for comparison, shown as a solid red curve in Fig. 4.5. The origin of this 120° symmetry in the AHE can be understood by revisiting the different components of the anti-symmetric transverse conductivity $\sigma_{xy}^{Anti-Sym.}$

$$\sigma_{xy}^{Anti-Sym.} = \gamma_{\mathrm{Oct}} \left[\vec{Q}_{T_{1g}}\right]_z + \gamma_{\mathrm{dip}} \left[\vec{M}_{T_{1g}}\right]_z + \gamma_{\mathrm{SSC}} \left[\sum_{ijk} \vec{S}_i \cdot (\vec{S}_j \times \vec{S}_k)\right] \tag{4.2}$$

In the absence of contributions from $\vec{M}_{T_{1g}}$, the next leading term, $\vec{Q}_{T_{1g}}$, is expected to contribute to the signal. To explore this further, we performed a symmetry analysis in conjunction with density functional theory (DFT) calculations of the response of $\vec{Q}_{T_{1g}}$ to the direction of the external $\vec{H}$ depicted in Fig.4.6(d). This theoretical analysis was performed by Dr. Tom. G. Saunderson and Dr. Fabian Lux. The black stars represent the eight energetically favorable orientations of the octupole vector $\vec{Q}_{T_{1g}}$, which correspond to the eight equivalent [111] directions. Of these 8, two – Υ_0 and $\overline{\Upsilon}_0$ – correspond to the OOP directions [111] and $[\bar{1}\bar{1}\bar{1}]$ which are not accessible because of the IP direction of the $\vec{H}$. However, the other 6, namely Υ_1, Υ_2, Υ_3 and $\overline{\Upsilon}_1$,$\overline{\Upsilon}_2$,$\overline{\Upsilon}_3$ are. When one applies $\vec{H}$ along $\phi = 90°$ for example, $\vec{Q}_{T_{1g}}$ can align along the Υ_1. The arrangement of Mn spins and the resultant $\vec{Q}_{T_{1g}}$ of this configuration within a single sublattice is depicted in Fig.4.6(c) pointing along Υ_1. Here, one can see which of the equivalent (111) planes the spins align in, and correspondingly which 111 direction, the $\vec{Q}_{T_{1g}}$ points toward.

In order to visualize how this affects the observed AHE signal, let us have a closer look at the six directions that are accessible in our geometry. From the [111] viewing direction, as illustrated in Fig. 4.7(a), it is immediately observable how the six directions present themselves in a 120° symmetry. If we look at the octupoles from the perspective shown in Fig. 4.7(b) where the (111) plane is depicted in purple, it further reveals that Υ_1, Υ_2, Υ_3 have a positive component orthogonal to the (111) plane, and $\overline{\Upsilon}_1$,$\overline{\Upsilon}_2$,$\overline{\Upsilon}_3$ have a negative component. This orientation is crucial to understanding their contribution to the σ_{xy} as in our geometry, where the Hall measurements are performed in the (111) plane, only the components orthogonal to the plane will contribute to σ_{xy}. When the $\vec{H}$ is along $\phi = 90°$, for example, $\vec{Q}_{T_{1g}}$ will align along Υ_1. Υ_1 not just has a nonzero OOP contribution, but the projection of Υ_1 along [111] is positive. This results in the positive AHE we observe when $\vec{H}$ is along $\phi = 90°$. Similarly, when $\vec{H}$ is along $\phi = 30°$, $\vec{Q}_{T_{1g}}$ aligns along $\overline{\Upsilon}_2$ which has a non-zero OOP component and has a negative projection along [111]. This results in a negative contribution of the octupole to the AHE. However, if the $\vec{H}$ is along $\phi = 0°$, there is no preferred direction of alignment for the octupole, resulting in an average of no $\vec{Q}_{T_{1g}}$ contribution to σ_{xy}.

Considering the role of $\vec{Q}_{T_{1g}}$, two important features become evident: (i) the presence of a nonzero AHE even in an in-plane magnetic field geometry. Although $\vec{M}_{T_{1g}}$ aligns along the direction of $\vec{H}$ and does not contribute to the AHE in this configuration, $\vec{Q}_{T_{1g}}$ retains nonzero components along the [111] direction, resulting in a finite AHE signal. (ii) Furthermore, the symmetry properties of Υ_i and $\overline{\Upsilon}_i$ with respect to the (111) plane account for the experimentally observed 120° periodicity in R_{xy}, as shown in Fig.4.5.

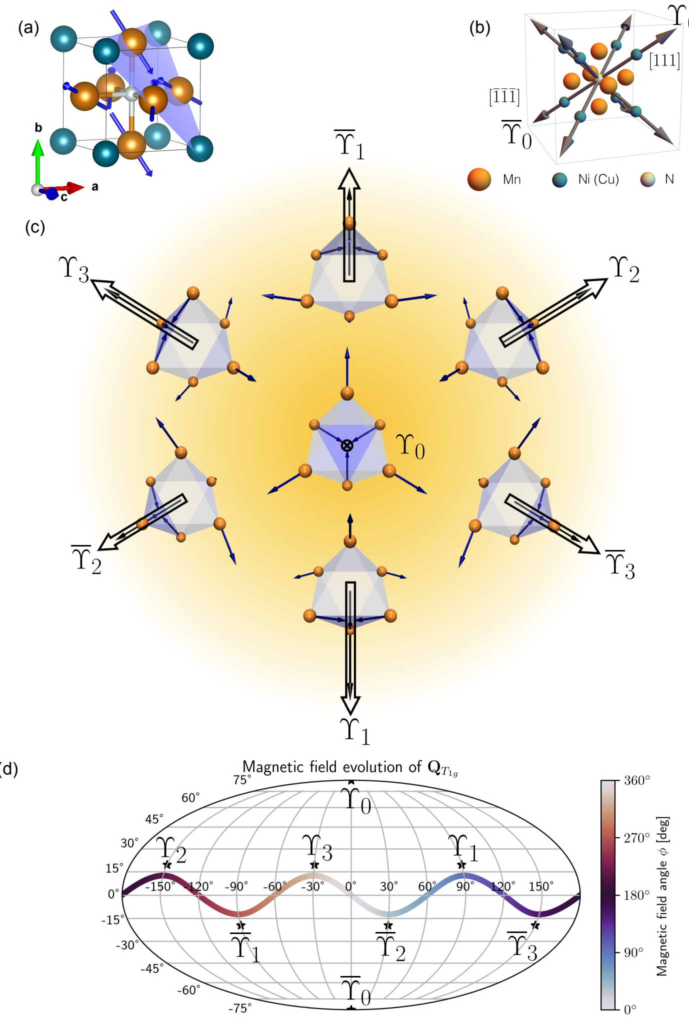

Figure 4.6.: Cubic unit cell of Mn_3NiCuN with Mn atoms in orange, Ni and Cu in blue, and N in off-white. The blue arrows in (a) indicate the Mn spin arrangement in the (111) plane (blue). (b) Depiction of the eight octupoles which point perpendicular to the eight equivalent (111) planes. The out-of-plane components of the octupole moment are labelled as Υ_0 and $\overline{\Upsilon}_0$, pointing along the [111] and $[\bar{1}\bar{1}\bar{1}]$ directions respectively. (c) blackThe Mn spin configurations (blue arrows) and the corresponding octupoles (black bold arrows) when a magnetic field is applied along different crystallographic directions in the (111) plane. The particular directions labelled represent the specific angles where the magnetic field is parallel to the in-plane projections of the octupoles Υ_i and $\overline{\Upsilon}_i$. The central panel of (c) shows the spin configuration when the magnetic field is swept out the kagome plane ($\overline{\Upsilon}_0$) and that corresponds to $\vec{Q}_{T_{1g}}$ along [111] direction. (d) Graphical representation of the evolution of $\vec{Q}_{T_{1g}}$ in spherical coordinates as a function of the applied external magnetic field in the (111) kagome plane (shown in color bar). It shows 120° oscillations of the projection of $\vec{Q}_{T_{1g}}$ along [111] direction, parallel to the Υ_0 octupole. When the magnetic field is swept from positive to negative in-plane field along certain in-plane projections of the octupole, for example Υ_1 to $\overline{\Upsilon}_1$, there is switching of the out-of-plane component of $\vec{Q}_{T_{1g}}$ with the maximum strength (shown in black stars), which will manifest as a step in the Hall resistance (generating AHE) and follow 120° angular dependence. Adapted from [95]

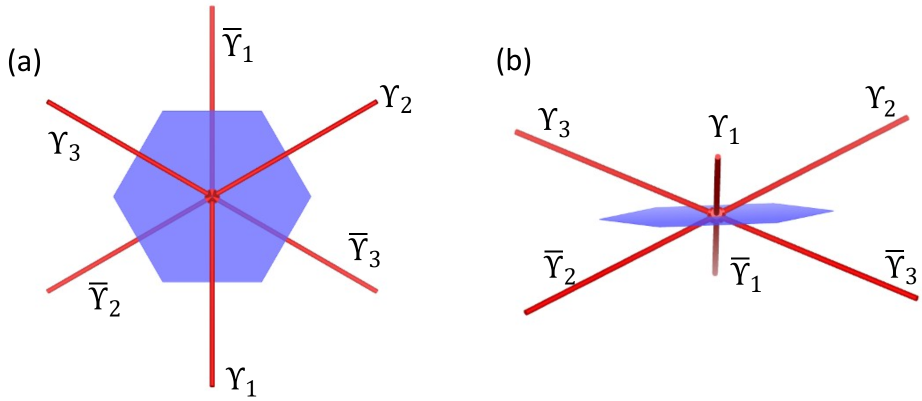

Figure 4.7.: Preferred orientations of the 6 $\vec{Q}_{T_{1g}}$ directions accessible in an IP field geometry shown in red and the (111) plane in purple (a) from the [111] perspective and (b) from the perspective showing the projection in and out of the (111) plane.

4.3. Additional features in the $R_{xy}^{Anti-Sym.}$ hysteresis curves

In the previous section, we examined the symmetry of $R_{xy}^{Anti-Sym.}$ (15 T) with respect to ϕ and and identified that it reflects the symmetry of the energy minima of the $\vec{Q}_{T_{1g}}$ vector. Considering that the octupoles exhibit a preferred direction along [111], and given that six equivalent directions are available in the in-plane (IP) geometry, a natural emergence of a 120° symmetry is observed.

To further investigate this symmetry, individual field sweeps were performed over a range of ϕ to construct the $R_{xy}^{Anti-Sym.}$ (15 T) vs ϕ plot. These sweeps revealed non-trivial features that deviate from the typical tanh shape commonly associated with anomalous Hall effect (AHE) and magnetization curves (See.). Examples of such non-trivial features are presented in Fig. 1 (a) and (b).

The curves shown in Fig. 1(a) display distinct characteristics, such as peaks and dips near zero field, which differ from the expected tanh behaviour. Additionally, in Fig. 1 (b), there are cases where the peaks exceed the magnitude of the saturation signal, highlighting the presence of unexpected behaviours in the system. The expectation of a tanh behaviour arises from the conventional understanding of AHE and magnetization curves of simple ferromagnets. However, it would be sensible to check whether a tanh

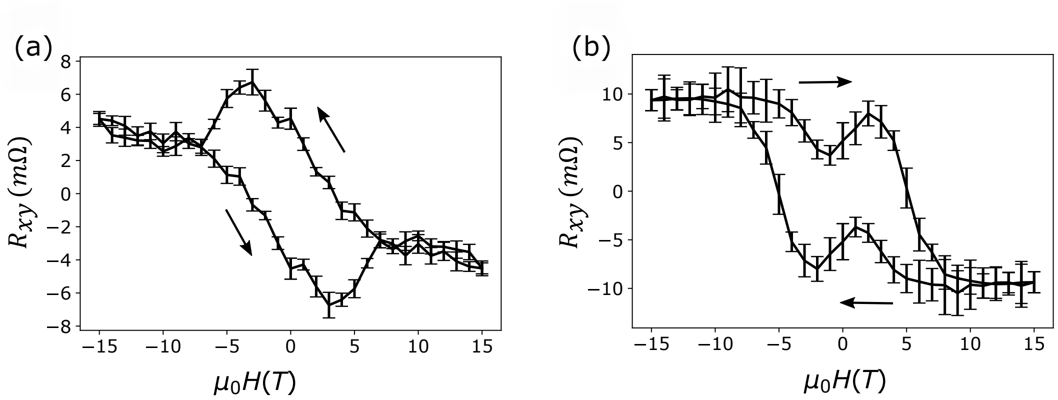

Figure 4.8.: $R_{xy}^{Anti-Sym.}$ vs $\vec{H}$ plot of two individual ϕ showing non-trivial features like (a)Peaks higher than saturation $R_{xy}^{Anti-Sym.}$ at intermediate $\mu_0\vec{H}$ and (b) bumps and dips indicating additional contributions apart from $\vec{Q}_{T_{1g}}$.

AHE behaviour is expected for an NCAFM. But before that, let us go through a brief literature review on non-trivial shapes in the AHE signal.

Non-trivial features in the transverse Hall signal are often attributed to the topological Hall effect (THE), which arises from non-trivial topological structures such as magnetic skyrmions [58]. However, several studies have highlighted that attributing such features solely to the THE requires specific conditions to be met, and simplistic attributions can be potentially incorrect [96, 60, 61]. In many cases, non-trivial transverse Hall signals can emerge from two-channel sources of the anomalous Hall effect (AHE) with opposing Hall conductivity factors. This phenomenon is particularly relevant in bilayer systems, such as those composed of oxides of Sr [62, 63, 64]. In such systems, the two channels may manifest in the AHE signal as one hysteretic channel and one non-hysteretic channel, resulting in the observed non-trivial shapes of the AHE curves. In contrast to these systems, our material, Mn_3NiCuN, does not exhibit these characteristics. The centrosymmetric structure of Mn_3NiCuN precludes the formation of topologically non-trivial structures with a fixed chirality like skyrmions, and it is not known to support multiple AHE channels as seen in bilayer systems. Given this context, we turn to symmetry analysis of the AHE contributions to propose that the non-trivial signal observed in our system arises from scalar spin chirality (SSC). The antisymmetric contribution to the transverse conductivity is given by 2.31 reproduced here:

$$\sigma_{xy}^{Anti-Sym.} = \gamma_{\text{Oct}} \left[\vec{Q}_{T_{1g}}\right]_z + \gamma_{\text{dip}} \left[\vec{M}_{T_{1g}}\right]_z + \gamma_{\text{SSC}} \left[\sum_{ijk} \vec{S}_i \cdot (\vec{S}_j \times \vec{S}_k)\right] \tag{4.3}$$

From the equation, one notes that for a non-zero value of γ_{SSC}, the contribution to $\sigma_{xy}^{Anti-Sym.}$) is zero when (1) two of the spins point in the same direction or when (2)

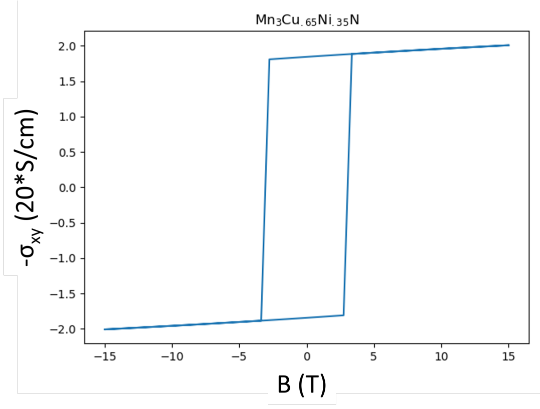

Figure 4.9.: -σ_{xy} as a function of applied field calculated using DFT and symmetry analysis.

all three spins are co-planar. In the noncollinear spin structure present in Mn_3NiCuN, this would mean that at the ground state where there is vanishingly small out-of-plane canting (see:2.4), we do not expect a large SSC contribution to the $\sigma_{xy}^{Anti-Sym.}$. However, with the sweeping of strong of strong fields, this cannot be ruled out.

In order to investigate the nature of the additional contribution, the first task is to model the σ_{xy}^{Oct}, after which we can model the additional contribution to $\sigma_{xy}^{Anti-Sym.}$ and its behaviour in response to the $\vec{H}$. The $\vec{M}$ vs $\vec{H}$ curve of a ferromagnet from mean-field and phenomenological models for ferromagnets is obtained (See 2.3.4) as a hyperbolic tangent. Since the AHE in simple ferromagnets is primarily a linear function of the net magnetization, it follows that the AHE vs $\vec{H}$ also takes the form of a hyperbolic tangent. Now it is interesting what form is taken by the AHE in an NCAFM system where the AHE has a larger contribution, not from $\vec{M}$ but other sources. It is noteworthy that the AHE in non-NCAFMs has been consistently reported to exhibit a tanh-like field sweep loop, which, at the very least, serves as empirical support for this behavior. [97, 98]. To test this proposition, one might derive this from first principle methods(See A.4). Symmetry analysis along with DFT calculations were used by Dr. Tom G. Saunderson and Dr. Fabian Lux to evaluate the σ_{xy}^{Oct} as a function of $\vec{H}$. The result is shown in Fig. 4.9. One can see that the AHE in NCAFM has the same tanh function as for a ferromagnet. To confirm this behaviour atomistic spin dynamics simulations (ASDS) of the Mn_3NiCuN system were performed with the help of Dr. Rocío Yanes-Díaz. The advantage of this technique is that we can go beyond a one unit cell model of Mn_3NiCuN, and have a three dimensional system mimicking the actual physical system that we use for our measurement. Also, with ASDS, we are easily able to introduce temperature into the system in the form of spin-fluctuation distribution, which is challenging for a first principles study. The analysis was performed in a 128 x 128 x 6 cell system with a total of close to 295000 Mn spins with periodic boundary

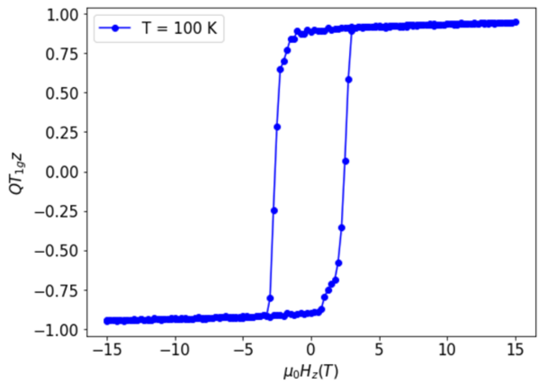

Figure 4.10.: $\vec{Q}_{T_{1g}}$ vs $\mu_0\vec{H}$ obtained from the atomistic spin dynamics simulation of the Mn_3NiCuN system shows a tanh hysteresis

conditions. The behaviour of the system was evaluated as a function of $\mu_0\vec{H}$ along [111], and $\vec{Q}_{T_{1g}}$ as a function of $\mu_0\vec{H}$ at 100 K is shown in Fig.4.10.

Although the model used for the ASDS is taken utilizing the energy parameters from DFT, we can see that for a finite system, we are able to reproduce the $\vec{Q}_{T_{1g}}$ dependence of $\vec{H}$ obtained from the symmetry analysis. With this confirmation, we can confidently assert that the $\vec{Q}_{T_{1g}}$'s behaviour in response to $\vec{H}$ resembles that of $\vec{M}$ and can be effectively modelled as a hyperbolic tangent function. Now, we model every field sweep as a combination of hyperbolic tangent function originating from σ_{xy}^{Oct}. The remanant signal represents a possible additional SSC contribution. We chose the Gaussian function to fit because it naturally reflects the distribution of the SSC associated with each individual kagome lattice. Moreover, as we will see, this choice proves to be a particularly good one, as the Gaussian fit aligned remarkably well with the experimental data, reproducing the amplitude and width of the observed THE-like signal with high accuracy.

Building on this rationale, we proceed to analyze fits constructed from a combination of hyperbolic tangent and Gaussian functions. The function used to fit the signal is :

$$R_{xy}^{Anti-Sym}(B) = R_{xy}^{Oct}\tanh\left(a\left(B - B_c\right)\right) + R_{xy}^{SSC}\exp\left(-c\left(B - B_0\right)^2\right), \tag{4.4}$$

where R_{xy}^{Oct} represents the maximum contribution coming from the octupole moment, and R_{xy}^{SSC} the maximum contribution of the scalar spin chirality, B is the magnitude of the magnetic field, B_c is the coercivity, a is related to the slope of R_{xy}^{Oct} switching, and c is related to the width of the SSC signal.

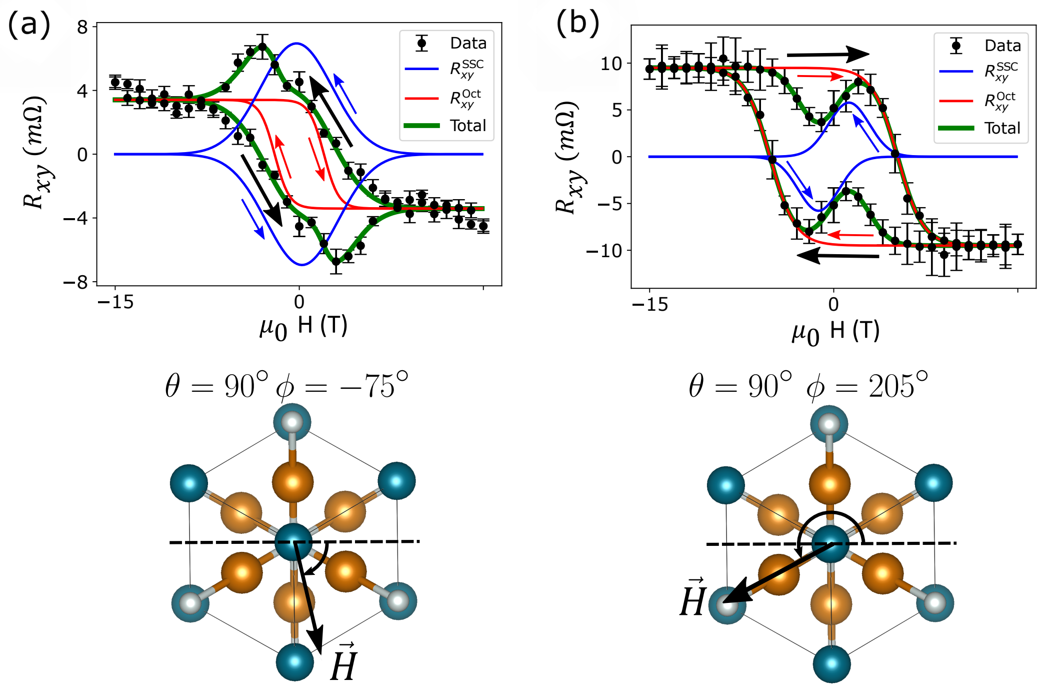

Figure 4.11.: R_{xy}^{AHE} hysteresis decomposed into R_{xy}^{Oct} (red), and R_{xy}^{SSC}(blue), and the combined fit (green) using a combination of hyperbolic tangent and gaussian functions respectively of two exemplar ϕ sweeps. The arrows represent the direction of sweep. The schematic below the graphs in (a) and (b), respectively, shows the lattice when viewed from [111] with the black arrows pointing to the direction of $\vec{H}$. Adapted from [95]

Fig.4.11(a) shows one example of such a fit, while Fig.4.11(b) shows another. Here, the black dots represent the experimental data points, the red curve the hyperbolic tangent fit of R_{xy}^{Oct}, and the blue curve the Gaussian fit of R_{xy}^{SSC}. It is evident that the combination of functions employed has produced a strong alignment with the signal. While only two examples of the fit are presented here, all individual sweeps at different ϕ were analyzed using the same combination of functions, resulting in a good fit with an error margin of less than 5%. A close examination of the field cycling direction and the corresponding contributions from the R_{xy}^{Oct} (red), and R_{xy}^{SSC}(blue) components—indicated by red and blue arrows, respectively—reveals a noteworthy feature in 4.11(a) for $\phi = 75°$. Such behavior would be thermodynamically forbidden if the AHE arose solely from $\vec{Q}_{T_{1g}}$ or $\vec{M}_{T_{1g}}$ and such behaviour warrants further investigation to understand its underlying mechanism.

4.4. Angular dependence of R_{xy}^{Oct} and SSC) hysteresis curves

In the previous section, we justified modelling the signal $R_{xy}^{Anti-Sym.}$ as a combination of hyperbolic tangent function (for R_{xy}^{Oct}) and a Gaussian (for the additional contribution). We also saw that this combination of functions resulted in a good fit for the experimentally observed signal. Having observed the three-fold symmetry in ϕ of $R_{xy}^{Anti-Sym.}$ (15 T)) in 4.2, it would be interesting to look at the ϕ-dependence of the two components of $R_{xy}^{Anti-Sym.}$, namely $R_{xy}^{Oct}$and R_{xy}^{SSC}.

As mentioned in 4.2, we performed the measurements on two Hall devices to acquire a robust data set and avoid any effects due to local inhomogeneities. Further, the measurements were repeated after warming to room temperature and re-cooling to 100 K to obtain a comprehensive data set. The averaged values of all R_{xy}^{Oct} are plotted as red dots and R_{xy}^{SSC}as blue dots in Fig. 4.12(a). One immediately notices a sinusoidal behaviour of both R_{xy}^{Oct} and R_{xy}^{SSC}. This was confirmed when a fit was performed for the data points. The red curve shows the fit for R_{xy}^{Oct} while the blue curve shows R_{xy}^{SSC}. Both have sinusoidal functions with a 120° periodicity. We also notice that the blue curve has a 180° phase shift compared to the red one, perhaps hinting at a competing interplay of these two contributions.

One sees that R_{xy}^{Oct} is equivalent to $R_{xy}^{Anti-Sym.}$ (15 T) and in many cases identical because R_{xy}^{Oct} is defined as the saturation value of the hyperbolic tangent fit function, which in many cases equals the $R_{xy}^{Anti-Sym.}$(15 T) value. Because of this, it is natural to expect a 120° periodicity in R_{xy}^{Oct} because of the symmetry in the preferred directions of the octupole moment as discussed in 4.2. However, it is interesting that R_{xy}^{SSC}

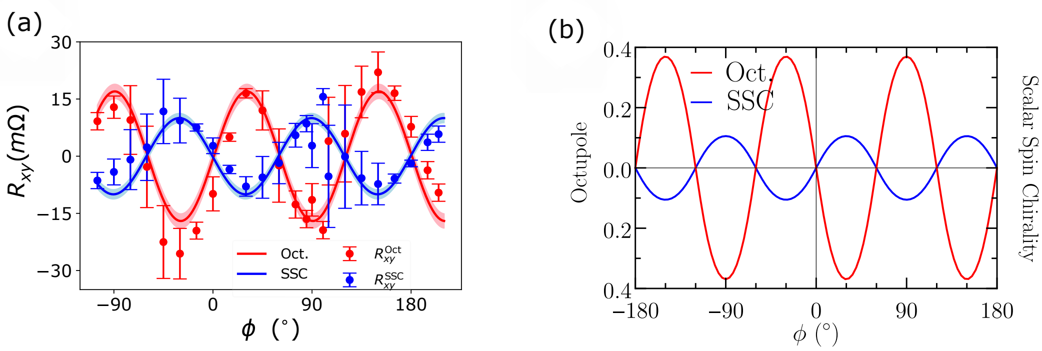

Figure 4.12.: Red and black points correspond to data quantified values of R_{xy}^{Oct} and R_{xy}^{SSC} fit by sinusoidal curves with 120° periodicity. Adapted from [95]

also exhibits the same symmetry and, more interestingly, shows a 180° phase shift compared to R_{xy}^{Oct}.

Let us now see if this is corroborated by a theoretical study of the octupolar and SSC contributions to $\sigma_{xy}^{Anti-Sym.}$ performed by Dr. Tom G. Saunderson and Dr. Fabian Lux. We can theoretically compute the SSC ($\vec{S}_1 \cdot (\vec{S}_2 \times \vec{S}_3)$) and octupole ($\vec{Q}_{T_{1g}}$) as a function of ϕ and observe if a similar dependence to the experiment is observed. This was done by first parametrizing a free energy expression of the irreducible representations (See A.4) with first principles calculations and solve a Landau- Lifshitz-Gilbert equation to provide the dependence of the SSC and the octupole ($\vec{Q}_{T_{1g}}$) moment as a function of in-plane magnetic field angle ϕ. More details are provided in A.4). The result suggests that the non-coplanar spin-textures are possible, leading to a non-zero SSC. It also predicts that both the octupole signal (arising from $\vec{Q}_{T_{1g}}$) and the THE-like signal (arising from SSC) possess an angular dependence with 120 ° rotational symmetry. Results from the analysis is shown in Fig.4.12(b) where the red curve shows the contribution of $\vec{Q}_{T_{1g}}$ to the $\sigma_{xy}^{Anti-Sym.}$ and the blue curve shows that of SSC to $\sigma_{xy}^{Anti-Sym.}$. In this figure, we see that 120° symmetry of both $\vec{Q}_{T_{1g}}$ and SSC is obtained as observed experimentally in Fig.4.12(a). Moreover, we also observe a 180° phase difference between the $\vec{Q}_{T_{1g}}$ and SSC contributions, which is consistent with the experimental results in Fig.4.12(a). This qualitative consistency between the experimental observation and the theoretical analysis strongly supports our hypothesis that the source of the additional Gaussian contribution to the $\sigma_{xy}^{Anti-Sym.}$ has its origins in SSC.

While the identical 120° symmetry of SSC with respect to ϕ is expected from arguments similar to the symmetry of $\vec{Q}_{T_{1g}}$ elaborated in 4.2, it reinforces the coexistence of different spin orders, here manifesting as different contributions to the $\sigma_{xy}^{Anti-Sym.}$, representing the magnetic state of the system – the ferromagnetic term $\vec{M}_{T_{1g}}$, partly responsible for the OOP AHE, the $\vec{Q}_{T_{1g}}$ responsible for the OOP as well as the IP AHE, and finally, the SSC acting when the spins are non-coplanar. This sets Mn_3NiCuN and the larger NCAFM class apart from the FM and collinear AFM, which host only one order parameter apiece, namely the magnetization and the Neél vector, respectively.

4.5. Temperature dependence of $R_{xy}^{Anti-Sym}$

In the previous sections (Results/AHE and Results/Decomposition), we conducted a detailed analysis of the measured data at 100 K. In this section, we present measurements performed across a range of temperatures to determine whether the observed results and their interpretation are specific to the narrow vicinity of 100 K or if they remain consistent over a broader temperature range below the Néel temperature. If an anomaly were to appear around 100 K, it would be of particular interest to investigate the nature of the phase present at this temperature and how it influences the observed interplay between the octupole moment and scalar spin chirality. Measurements were conducted at 80 K, 130 K, 145 K, 195 K, 200 K and 230 K. At each temperature, IP field sweeps were performed while simultaneously measuring the transverse Hall response at intervals of IP field angle $\phi = 30°$. Following the measurements, $R_{xy}^{Anti-Sym}$ was extracted using the procedure outlined in Section (Results/AHE) and detailed in Appendix (Data Extraction). It was then decomposed into R_{xy}^{Oct} and R_{xy}^{SSC}, following the method described in Section (Results/Decomposition), where they were modelled as hyperbolic tangent and Gaussian functions, respectively. The extracted R_{xy}^{Oct} and R_{xy}^{SSC} components were then plotted as a function of ϕ, represented by red and blue points, respectively, in Fig. 1. A sinusoidal fit was applied to the data points, shown as red and blue curves for R_{xy}^{Oct} and R_{xy}^{SSC}, respectively. This procedure was repeated for all measured temperatures, with the results presented in Fig. 4.13.

For T= 230 K , only R_{xy}^{AHE} is plotted, as the signal was too weak to be reliably modelled and was indistinguishable from noise.

A visual inspection of the sinusoidal fits for R_{xy}^{Oct} and R_{xy}^{SSC} in Fig. 4.13 indicates that below T_N, both components maintain a 120° symmetry as a function of ϕ. This suggests that the mechanisms responsible for the AHE – the $\vec{Q}_{T_{1g}}$ and SSC – persist over a broad temperature range below T_N rather than being confined to a narrow region around 100 K, as discussed in 4.3. This finding allows us to generalize and expand the role of the $\vec{Q}_{T_{1g}}$ and SSC as intrinsic parameters of noncollinear antiferromagnetism, representing distinct spin orders that act simultaneously under an applied

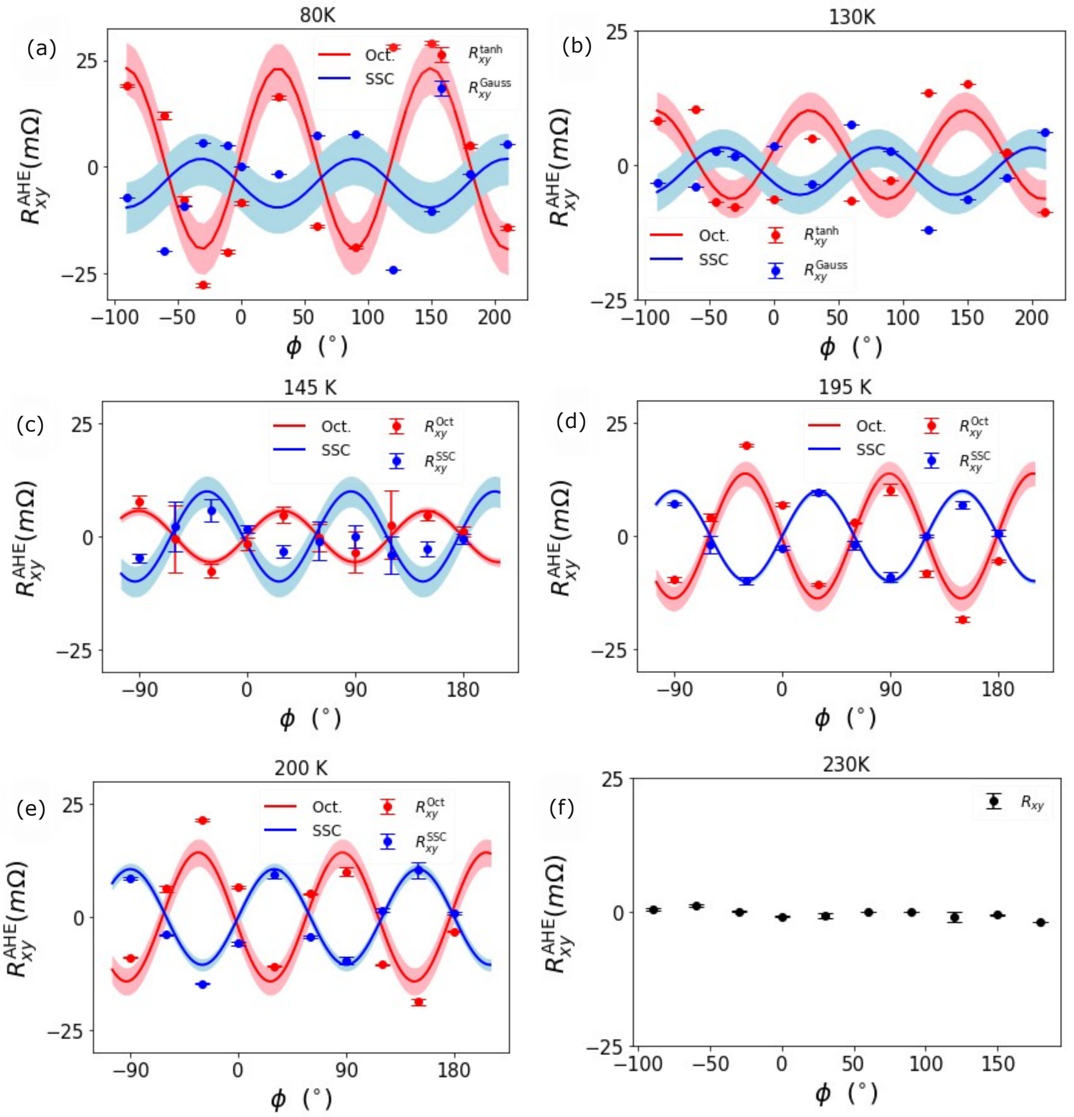

Figure 4.13.: (a)-(e) The angular dependence of the octupole (in red) and scalar spin chirality contributions (in blue) to the transverse Hall signal exhibit blackanalogous behavior across temperatures up to T_N. (b) The signal at 230 K disappears, indicating it originates from the non-collinear antiferromagnetic order.

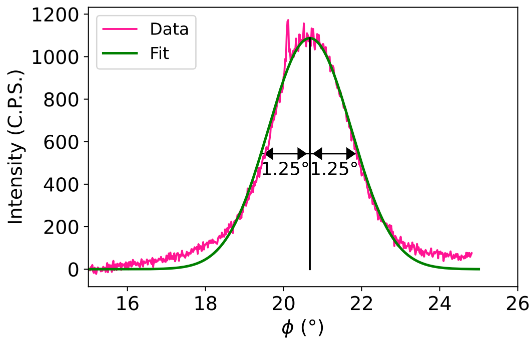

Figure 4.14.: Rocking curve at the (111) peak of the Mn_3NiCuN thin film shows alignment with the substrate OOP direction but with a spread of 1.25 ± 0.01°.

magnetic field. Furthermore, we can rule out the presence of additional phases in the temperature range of 80 K to T_N that could influence the transverse Hall signal. If such a phase existed, it would have resulted in a qualitatively different behavior of R_{xy}^{AHE} , making it impossible to model it solely as a combination of R_{xy}^{Oct} and R_{xy}^{SSC}. Additionally, we observe that the signs of R_{xy}^{Oct} and R_{xy}^{SSC} reverse between 80 K and 200 K, with the transition occurring more precisely between 145 K and 195 K. A sign reversal in R_{xy}^{AHE} has been previously reported[41], making the corresponding change in R_{xy}^{Oct} expected. However, we also note that R_{xy}^{SSC} undergoes a sign change, further confirming that both spin orders contribute in unison to the AHE.

4.6. Structural characterization of Mn_3NiCuN thin films

X-ray diffraction (XRD) was employed to characterize the growth of Mn_3NiCuN thin films on an MgO substrate. This technique allows for the assessment of two key aspects of film growth: (1) the alignment of the out-of-plane (OOP) direction of the thin film with that of the substrate ([111]) and (2) the alignment of the in-plane (IP) directions of the substrate and the thin film. To verify these alignments, we conducted two measurements: (1) a rocking curve scan to assess the OOP alignment of the Mn_3NiCuN thin film with the substrate's [111] orientation, and (2) an analysis of the in-plane alignment of the thin film relative to the substrate. The rocking curve scan at the film peak, shown in Fig.4.14, presents the measured signal (pink) alongside a Gaussian fit (green). The observed peak, with a spread of 1.25±0.01°, confirms that the film is well aligned with the OOP axis of the substrate, with an alignment error corresponding to this spread. Although the lattice parameters of the substrate (4.21 Å) and Mn_3NiCuN (3.84 Å) exhibit a significant mismatch that hinders epitaxial growth, the observed OOP spread of 1.25±0.01° still shows epitaxial registry and is sufficiently small for the purposes of this study.

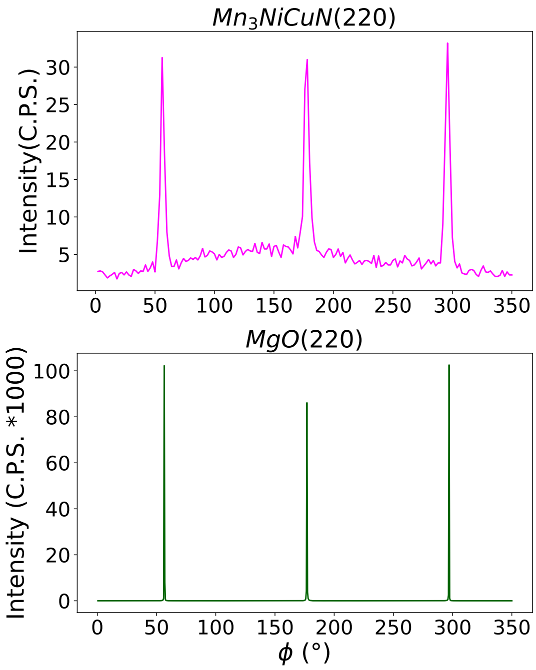

Figure 4.15.: ϕ-scans of (220) planes of the Mn_3NiCuN thin film (top) and the MgO substrate(bottom) show peaks with three-fold symmetry, demonstrating in plane alignment of the thin film with the substrate.

Next, we check the alignment of the thin film and the substrate in the IP directions. For this, we perform phi-scans for the (220) planes of the MgO substrate and the Mn_3NiCuN film, the results of which are shown in Fig.4.16. It can be seen that there are peaks at precisely the same ϕ and show a three-fold symmetry of the (220) peak for both the substrate and thin film demonstrating a clear in-plane alignment of the substrate and thin film directions.

To check the quality of in-plane alignment, we can check the spread in ϕ of the (220) peak of the thin film peak, shown in Fig.4.15 where the blue curve represents the signal obtained from the measurement and the red curve a gaussian fit performed. A spread of $2.34 \pm 0.33°$ is a result of the sizeable lattice mismatch but the clear alignment of the peaks with no other peaks excludes any parasitic phases or orientations. We note that the sharp peak close to the center is the signal from the substrate, which has been excluded for the calculation of the thin film peak spread. As mentioned before, one has to expect some spread because of the large lattice mismatch between MgO and Mn_3NiCuN.

More importantly, we note that neither the 1.25° spread from the out-of-plane (OOP)

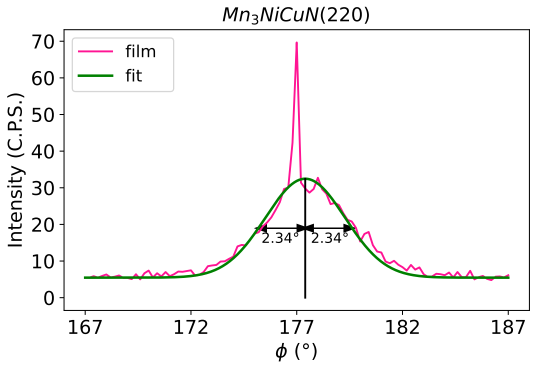

Figure 4.16.: Spread of the (220) peak of the Mn_3NiCuN film

[111] direction nor the 2.34±0.33° spread within the plane is sufficiently large to permit any alternative mechanisms that could account for the three-fold symmetry observed in the octupolar and scalar spin chirality terms extracted from the Hall signal. Furthermore, when considering the error introduced by the larger in-plane (IP) spread, the ϕ-dependence of R_{xy}^{Oct} and R_{xy}^{SSC} exhibits an even stronger agreement with the three-fold symmetry of these parameters. In a future study where the epitaxial growth of $Mn_3NiCuN(111)$ thin films is further optimized, the symmetries exhibited by R_{xy}^{Oct} and R_{xy}^{SSC} as a function of ϕ would become even more pronounced.

4.7. Effect of Pt layer on AH signal in Mn_3NiCuN/Pt system

Since the primary magnetotransport measurements (Section Results/AHE) were conducted with an in-situ deposited Pt capping layer, it is natural to consider whether this layer influences the results, particularly given its high conductivity and large spin-orbit coupling (SOC). Due to Pt's high conductivity, a significant fraction of the input current is expected to be shunted through the Pt layer. Consequently, this current shunting effect likely leads to an underestimation of the anomalous Hall resistivity quantified in this study. For a 6 nm Pt thin film, we measured a resistivity of $\approx 90\mu\Omega cm$, while for a 50 nm Mn_3NiCuN thin film, the resistivity was $\approx 170\mu\Omega cm$. Using a two-channel resistor model, we estimate that approximately 78% of the current flows through the Mn_3NiCuN layer. Since the Pt layer cannot generate a time-odd signal in our system, the reported anomalous Hall (AH) resistivity is underestimated by approximately 22%.

While current shunting does reduce the observed signal, we emphasize that it merely leads to a lower measured magnitude and is unlikely to introduce artifacts that could explain our observations. In particular, the step observed in the Hall voltage when

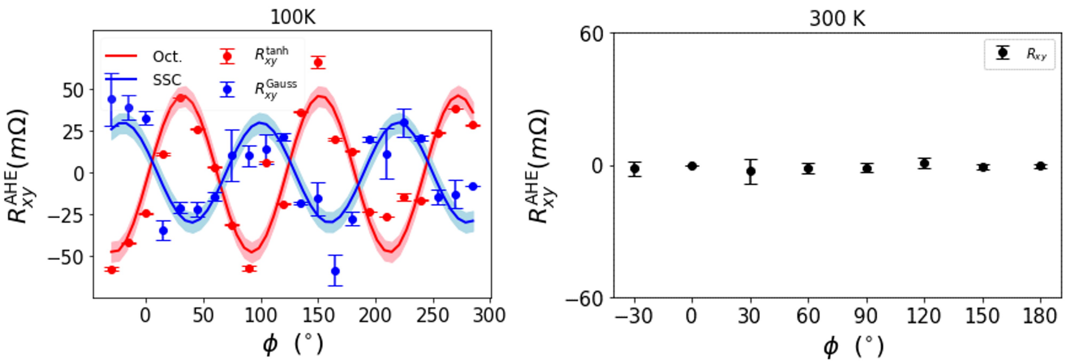

Figure 4.17.: (a) The angular dependence of the octupole (in red) and scalar spin chirality contributions (in blue) to the transverse Hall signal exhibit analogous behavior as in case of Fig. 2(h) in the main text.(b) The signal at 300 K disappears, indicating R_{xy} at 100 K originates from the non-collinear antiferromagnetic order.

sweeping an in-plane field cannot be attributed to magnetoresistance effects such as spin Hall magnetoresistance (SMR) at the Pt interface. Moreover, SMR effects typically exhibit much smaller amplitude effects compared to those observed in our study. Although SMR has been reported in the Mn_3Ir/Pt system [99] , we are not aware of any other effect that could produce a magnetoresistive response similar to what we observe here.

To assess the potential influence of the Pt capping layer on our results, we performed Hall measurements on an uncapped sample stack, MgO(111)/Mn_3NiCuN(50 nm), at 100 K. Following the same analysis procedure described in Section (Results/Decomposition), we extracted the R_{xy}^{Oct} and R_{xy}^{SSC} components from R_{xy}^{AHE} and plotted them as a function of the in-plane (IP) magnetic field angle ϕ. The results are presented in Fig. 4.17(a).

As clearly observed, even in the absence of the Pt capping layer, the R_{xy}^{Oct} component retains its characteristic 120° symmetry, while the R_{xy}^{SSC} component exhibits the exact same symmetry but with the opposite sign. This strongly suggests that the presence of Pt does not introduce any significant modification to the observed symmetry of the signals. To further verify the origin of the signal, we conducted a control measurement at 300 K, where the anomalous Hall effect (AHE) signal is expected to vanish due to the absence of long-range noncollinear antiferromagnetic (AFM) order. As anticipated, the signal disappeared at this temperature as shown in Fig. 4.17(b), confirming that the features observed at 100 K arise from the intrinsic noncollinear AFM order of Mn_3NiCuN rather than any extrinsic effects from the Pt layer.

This behavior is identical to what we observed in the Mn_3NiCuN/Pt stack, as described in 4.3. These findings conclusively demonstrate that the Pt capping layer—despite being a potential source of SOC at the interface—has an insignificant, if not negligible, influence on the observed Hall signal. Thus, our results are intrinsic to the Mn_3NiCuN layer and are not affected by interface-driven spin-orbit effects from the Pt layer.

5. Spin-orbit Torques in Mn_3NiCuN

5.1. Introduction

Spin-orbit torques (SOTs) currently offer a highly efficient mechanism for the current-induced switching of nanomagnets as required for the implementation of next-generation spintronics devices such as nonvolatile magnetic random-access memories (MRAM) [68, 100, 101]. Typically, strong SOTs are generated by applying an in-plane electric current in heavy metal (HM)/ferromagnet (FM) bilayers, where the HM generates a transverse spin current due to the spin-Hall effect (SHE) [3]. Recently, spintronics research has shifted its focus towards generating orbital Hall currents [10] in non-magnets (NMs). This shift is primarily due to the advantage that orbital Hall currents are not limited by spin-orbit coupling (SOC), thereby making a wide range of materials promising candidates for realizing MRAMs [101].

On the other hand, noncollinear antiferromagnets (NCAFMs) represent a new class of magnetic materials that exhibit various exotic effects [102], including chirality-induced anomalous Hall effect [4, 33, 6, 7, 95] without requiring net magnetization and unconventional spin currents [103, 34, 13, 104, 42, 35, 105, 106], although studies on orbital Hall effects (OHE) in these materials are still lacking. Previously, a chirality-driven novel spin current has been predicted to exhibit a strong temperature dependence due to spin fluctuations in NCAFM systems [13], yet this phenomenon has not been experimentally reported. Some recent works also suggest a significant effect on the orbital properties of conducting electrons in magnets induced by spin fluctuations [107, 108]. Therefore, exploring novel spin and orbital current generation over a wide temperature range in NCAFMs is of fundamental interest.

The orbital current is a fundamental quantity providing an intrinsic robust source [3] that can manifest as a spin current in the presence of spin-orbit coupling (SOC) [109, 12]. A nontrivial temperature dependence of the spin current has been theoretically predicted in magnetic materials, including ferromagnets [110] and collinear and noncollinear antiferromagnets [13, 17], due to spin fluctuations, which contribute to extrinsic scattering mechanisms such as skew scattering and side jump [110, 111, 13, 3].

Such fluctuation-mediated spin-current generation has been experimentally reported in ferromagnets [14, 15] and collinear AFMs recently [17, 18]. Magnon transport through a collinear insulating AFM spacer layer has been exploited to probe magnetic phase transitions [112, 113, 114]. These observations raise an intriguing question of whether spin fluctuations in chiral NCAFMs can be utilized to produce large SOTs for practical applications.

In this chapter, we address this key question while exploring the role of orbital current influenced by the chirality of NCAFM. We studied SOT produced by NCAFM, $Mn_3Ni_{0.35}Cu_{0.65}N$ (Mn_3NiCuN), as its Néel temperature (T_N) is around 210 K, providing access to quantify SOT from cryogenic temperatures to room temperature, and above and below T_N.

5.2. Material Stack

We prepared epitaxial Mn_3NiCuN films of a thickness of 15 nm by the reactive magnetron sputtering technique on a (111)-oriented single-crystal MgO substrate. More details of the thin-film growth can be found in previous works [7, 41]. After the Mn_3NiCuN growth, Cu (1.5 nm)/$Ni_{81}Fe_{19}$ (Py) (4–6 nm)/Cu (2 nm)/AlO_x (2 nm) was deposited *in situ*.

We use a 1.5 nm Cu spacer between Mn_3NiCuN and Py to magnetically decouple these layers, while the 2 nm thick top Cu layer is used to reduce the overall Oersted field acting on the magnet by current shunting effects through both the top and bottom layers. A schematic of the material stack is shown in Fig. 5.1.

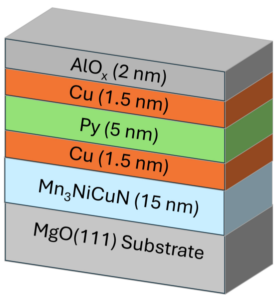

Figure 5.1.: A schematic of the thin-film material stack deposited to conduct spin-torque measurements.

Py is used as a magnet as it shows nominal in-plane anisotropy compared to other elemental magnets such as Co and Ni when grown on ordered materials such as Mn_3NiCuN. High Ni concentrations further enable us to probe the contribution of the orbital current by leveraging its spin-orbit coupling. In Mn_3NiCuN, the Kagome plane resides in the (111) sample plane where Hall-bars of dimensions 50×20 μm^2 are fabricated using standard optical lithography, etching, and lift-off techniques.

5.3. Magnetic Characterization of the Thin Film Stack

The work presented in this section was performed in collaboration with Dr. Aga Shahee and Dr. Arnab Bose. To determine the saturation magnetization M_S of the sample, we performed magnetization measurements using a SQUID magnetometer. An in-plane magnetic field was swept up to 0.5 T while monitoring the magnetic response. These measurements were repeated at multiple temperatures between 4 K and 300 K.

The temperature dependence of M_S is presented in Fig. 5.2(a). At room temperature, M_S is found to be approximately 600 emu/cc, which is slightly lower than the reported values for bulk Py samples. However, as the temperature decreases, M_S increases by approximately 10% at 4 K, as shown in Fig. 5.2(a). As discussed in Section 3.5, M_S is a key parameter in determining spin torques using the second-harmonic Hall (SHH) method, which will be employed subsequently in the chapter.

Fig. 5.2(b) illustrates the temperature dependence of the longitudinal resistance R_{xx} of the stack. To accurately measure R_{xx}, a high-value resistor (20–100 kΩ) is placed between the sample and the lock-in amplifier, allowing it to function as a current source. A notable change in the slope of R_{xx} around 210 K is observed, which is consistent with the expected Néel transition temperature T_N of Mn_3NiCuN.

The Hall resistance comprises contributions from both the anomalous Hall effect (AHE) and the planar Hall effect (PHE) in the first order (see Section 2.5.1). The coefficient associated with PHE, denoted as R_{PHE}, can be quantified by measuring $V_{1\omega}$ while rotating an external magnetic field H_{ext} within the sample plane. The temperature dependence of R_{PHE} is shown in Fig. 5.3(a), where a clear enhancement is observed near T_N.

Similarly, the coefficient associated with AHE, R_{AHE}, is determined by measuring

$V_{1\omega}$ while sweeping H_{ext} out of the sample plane. An enhancement in R_{AHE} is also observed near T_N, as shown in Fig. 5.3(b), further reinforcing the presence of a distinct phase transition at approximately 210 K. This transition is in agreement with the Néel temperature $T_N \approx 205$ K observed in the samples used for measurements in Section 4.2.

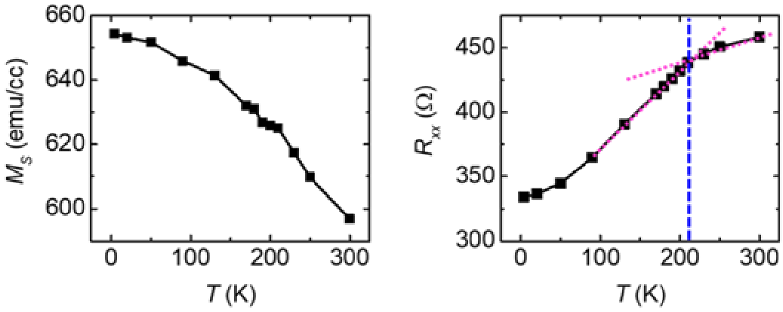

Figure 5.2.: (a) Saturation magnetization (M_S) of Py as a function of temperature (T). (b) Longitudinal resistance (R_{xx}) of the device as a function of temperature. The blue vertical line marks the expected T_N, and the pink dotted lines represent linear regression of R_{xx} below and above T_N. Adapted from [9].

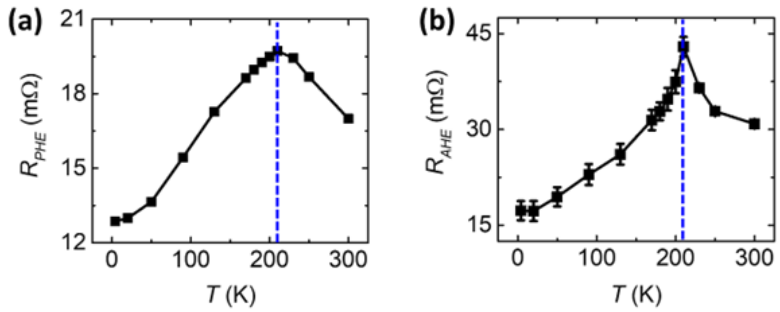

Figure 5.3.: Coefficient of (a) the planar Hall effect (PHE) (R_{PHE}) and (b) the anomalous Hall effect (AHE) (R_{AHE}) of the whole stack as a function of temperature. Both curves show a change in behavior close to the T_N marked by the blue dotted vertical line. Adapted from [9].

5.4. Temperature Dependent SOTs

To quantify SOTs, we adopt the well-established technique of second-harmonic Hall (SHH) measurements [84], performed in a three-dimensional vector-cryo setup in the presence of an external magnetic field (H_{ext}) at different temperatures (T) ranging from 4 K to 300 K. A schematic of the experiment is shown in Fig. 5.4(b).

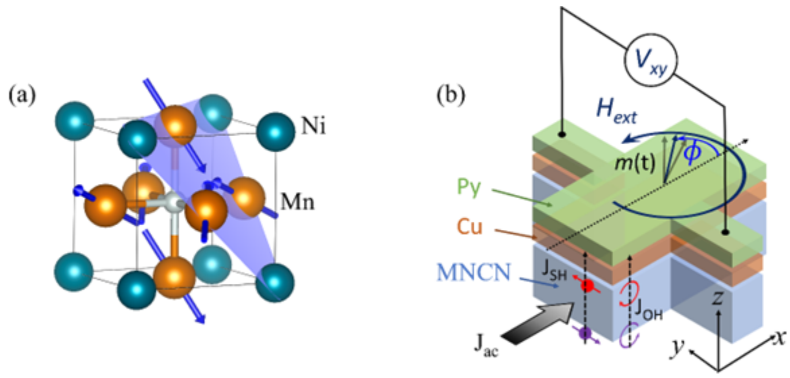

Figure 5.4.: (a) Crystal structure of $Mn_3Ni_{0.65}Cu_{0.35}N$ (Mn_3NiCuN) with spins in the Γ_{4g} configuration. (b) Schematic representation of SHH measurements. First harmonic voltages ($V_{1\omega}$) are measured by rotating the magnetic field (H_{ext}) in the plane to determine V_P.

V_{ANE} and V_{ONE} are the strengths of the anomalous Nernst effect (ANE) and ordinary Nernst effect (ONE), respectively, generated due to an unintentional out-of-plane thermal gradient coupled to the in-plane magnetization of Py and H_{ext}.

V_P is the coefficient of the planar Hall effect (PHE) voltage, expressed as:

$$V_{PHE} = V_P \sin 2\phi$$

where ϕ is the angle between the applied current and the magnetization in the sample plane (xy-plane), as illustrated in Fig. 5.4(b). V_P is determined by measuring $V_{1\omega}$ while rotating H_{ext} in the plane, shown in Fig. 5.5(a).

Similarly, V_A is the coefficient of the anomalous Hall effect (AHE) voltage:

$$V_{AHE} = V_A \cos\theta$$

where θ is the angle between the magnetization and the out-of-plane z-axis. V_A is obtained by measuring $V_{1\omega}$ while sweeping H_{ext} out of the plane, as shown in Fig. 5.5(b). The same curve provides information about $H_\perp$, the out-of-plane demagnetization field, typically around 0.4 T for a 4 nm thick Py film.

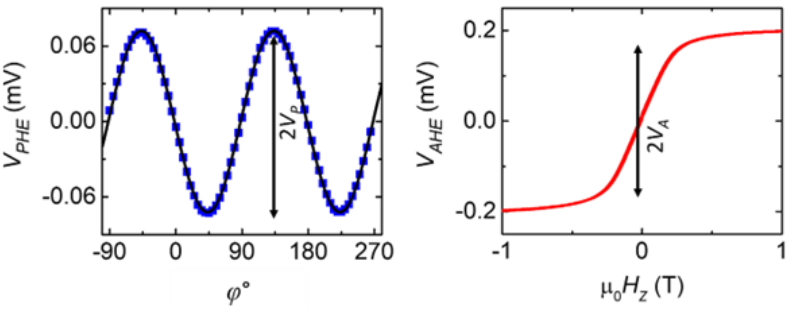

Figure 5.5.: Measured first-harmonic voltages ($V_{1\omega}$): (a) by rotating the magnetic field (H_{ext}) in-plane to determine V_P and (b) by sweeping the magnetic field out-of-plane to determine V_A. Adapted from [9].

Fig. 5.6(a) shows a typical second-harmonic voltage ($V_{2\omega}$) measured at two different H_{ext} values, 0.05 T (red squares) and 0.13 T (blue triangles), fitted to Eq. 3.2. We observe that the magnitude of $V_{2\omega}$ decreases for higher H_{ext} values, suggesting that the signals predominantly originate from SOTs.

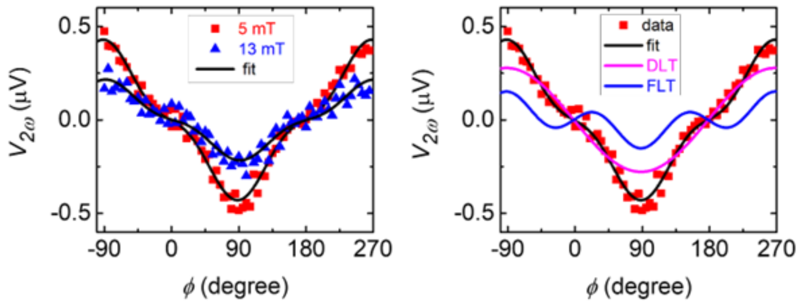

Figure 5.6.: (a) Measured second-harmonic Hall voltage ($V_{2\omega}$) for two different H_{ext} values. (b) Fitting of experimental data (red squares) showing contributions from damping-like torque (DLT, pink curve) and field-like torque (FLT, blue curve). Adapted from [9].

The $\cos\phi$ component (pink curve) reflects a dominant DLT contribution, whereas the $\cos\phi\cos 2\phi$ component (blue curve) indicates an FLT contribution.

To quantify the spin-orbit fields H^z_{DL} and H^y_{FL}, we plot the coefficients C_A and C_P as functions of H_{ext}, shown in Fig. 5.7. Both coefficients decrease with increasing H_{ext} and saturate close to zero, indicating that the $V_{2\omega}$ signal is primarily due to SOTs rather than thermal effects (e.g., ANE or ONE).

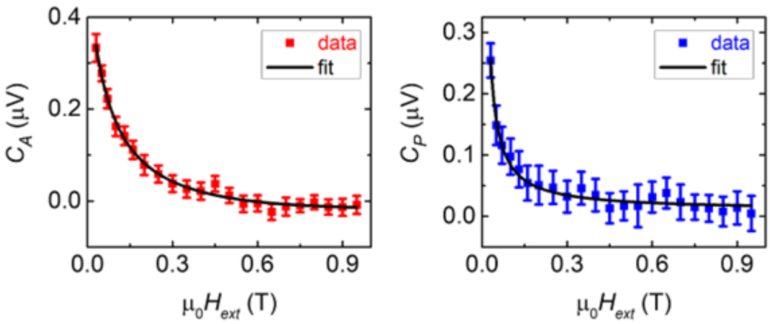

Figure 5.7.: Extracted values of (a) C_A and (b) C_P as functions of H_{ext}.

5.4.1. Temperature Dependence of ξ_{DL}^{E} and ξ_{DL}^{j}

The damping-like torque (DLT) efficiency per unit electric field, ξ_{DL}^{E}, and per unit current density, ξ_{DL}^{j}, are determined from the extracted effective fields using the following relations:

$$\begin{aligned} \xi_{DL}^{E} &= -\frac{2e}{\hbar}\mu_0 M_S t_{FM}\frac{H_{DL}^{z}}{E} \\ \xi_{DL}^{j} &= \xi_{DL}^{E}\rho \end{aligned} \tag{5.1}$$

Here, μ_0 is the vacuum permeability, $\hbar$ is the reduced Planck's constant, e is the elementary charge, M_S is the saturation magnetization, t_{FM} is the thickness of the ferromagnetic layer, H_{DL}^{z} is the effective field, E is the electric field, and ρ is the electrical resistivity.

The resistivity ρ of the Mn_3NiCuN thin films as a function of temperature is shown in Fig. 5.8(a). A noticeable slope change occurs around 210 K, consistent with the Néel transition.

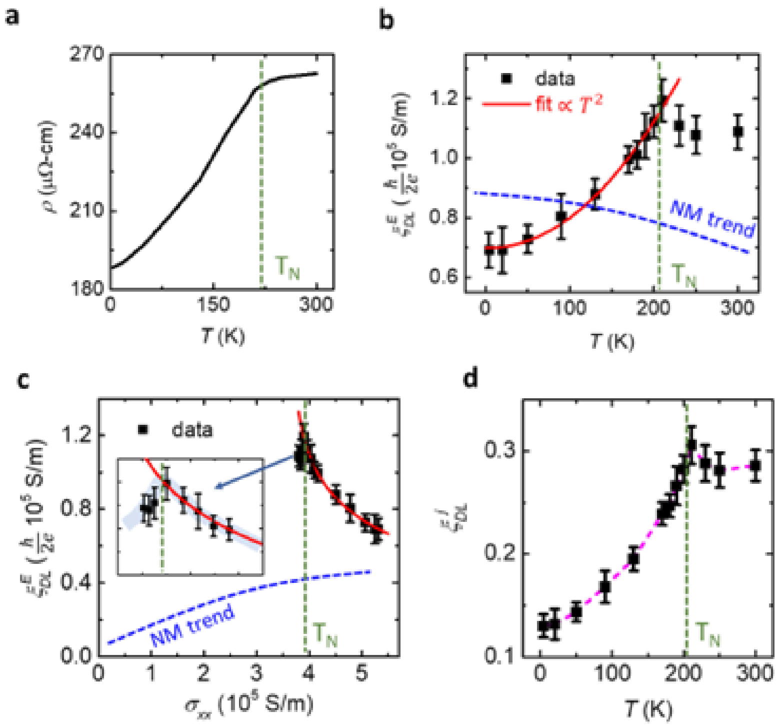

[]

Figure 5.8.: (a) Resistivity (ρ) of Mn_3NiCuN as a function of temperature. (b) Damping-like torque efficiency ξ^E_{DL} as a function of T. (c) Electrical conductivity σ_{xx} versus T. The blue-dashed curves indicate typical trends for conventional non-magnetic metals (e.g., Pt). (d) DLT efficiency per unit current density ξ^j_{DL} as a function of T. Adapted from [9].

Fig. 5.8(b) and (c) demonstrate a strong and unusual temperature dependence of ξ^E_{DL} and σ_{xx}. A large enhancement of ξ^E_{DL} (about 70%) and ξ^j_{DL} (about 140%) occurs near T_N, suggesting that spin fluctuations around T_N significantly enhance the spin-orbit torque generation.

The maximum values extracted are $\xi^E_{DL} \approx \frac{\hbar}{2e}(1.2 \pm 0.1) \times 10^5$ S/m and $\xi^j_{DL} \approx 0.30 \pm 0.03$, which are notably higher than those observed in heavy metals such as Pt [90] ($\xi^j_{DL} \sim 0.07$).

This strong temperature dependence deviates from conventional expectations: in typical nonmagnetic metals (NMs) like Pt, ξ^E_{DL} generally either increases linearly with σ_{xx}

in the "dirty" regime ($\sigma_{xx} < 10^6$ S/m) or saturates in the "clean" regime (10^6–10^8 S/m). However, for Mn_3NiCuN, ξ^E_{DL} decreases with increasing σ_{xx} below T_N, suggesting a different mechanism dominated by magnetic fluctuations.

5.5. Origins of the Observed Spin-Torques

To investigate the origin of the large observed DLT-efficiency, we carried out density functional theory (DFT) calculations for Mn_3NiCuN in both the nonmagnetic phase and the noncollinear antiferromagnetic (NCAFM) phase, adopting a static "all-in-all-out" magnetic configuration, as shown in Fig. 5.9(a) and (b), respectively.

Atomistic spin dynamics simulations were subsequently performed to assess the temperature dependence of the relevant parameters, shown in Fig. 5.9(c).

In both the magnetic and nonmagnetic phases, the DFT calculations predict a small intrinsic spin-Hall conductivity (σ_{SH}) with magnitude below $-\frac{e}{\hbar}1 \times 10^4$ S/m and a negative sign (similar to Ta). In contrast, a significantly large orbital-Hall conductivity ($\sigma_{OH} \sim +\frac{e}{\hbar}5 \times 10^5$ S/m) with a positive sign (similar to Pt) was found. The spin-orbit coupling in Mn_3NiCuN is very weak and does not contribute significantly to OHE.

Notably, the magnitude of σ_{OH} decreases slightly in the magnetic phase compared to the nonmagnetic phase, suggesting that the OHE fundamentally originates from the crystal structure itself.

Our experimentally measured $\xi^E_{DL} = +\frac{e}{2\hbar}(1.2 \pm 0.1) \times 10^5$ S/m is much larger than the calculated σ_{SH} (with opposite sign), indicating that the observed damping-like torque is predominantly due to the OHE, not the SHE. The reversal in sign is a key signature of OHE, consistent with other recent experimental reports [115, 116, 117].

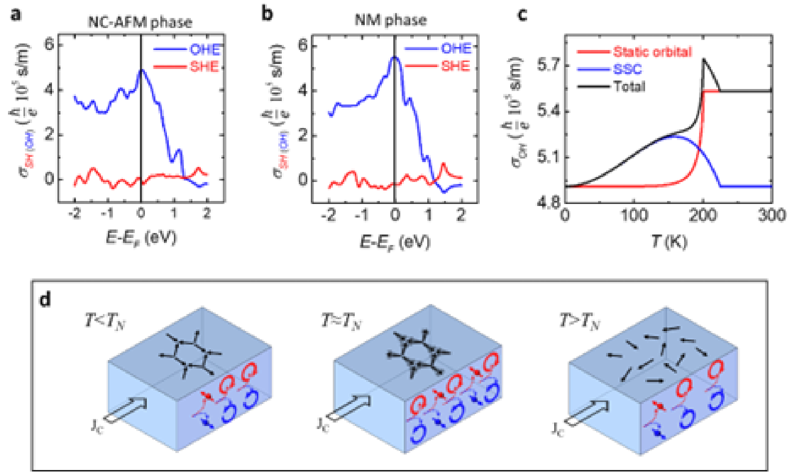

Figure 5.9.: (a), (b) DFT calculations of spin-Hall conductivity (σ_{SH}) and orbital-Hall conductivity (σ_{OH}) for Mn_3NiCuN in the NCAFM and NM phases, respectively.(c) Temperature dependence of σ_{OH} predicted by combining mean-field and scalar spin chirality (SSC) mechanisms.(d) Schematic illustration of spin and orbital current generation mechanisms across different temperature regimes. Adapted from [9].

The orbital current generated from Mn_3NiCuN is converted into a spin current via the spin-orbit coupling (SOC) of the adjacent Ni (in Py), leading to a large effective torque. The pronounced temperature dependence of ξ_{DL}^{E} observed below T_N cannot be fully explained by intrinsic OHE alone, suggesting the involvement of additional extrinsic mechanisms such as chirality-induced spin scattering.

Previous studies of other NCAFMs such as Mn_3Ir, Mn_3GaN, Mn_3Sn, and Mn_3Pt reported spin-orbit torque efficiencies ranging between 0.1 and 0.3 [35, 105, 118, 119, 120, 121, 122]. Our value of $\xi_{DL}^{j} \approx 0.30$ thus lies at the high end of these observations, with the added novelty of a sharp enhancement near the phase transition at T_N.

These findings indicate that orbital current generation in Mn_3NiCuN is a robust and temperature-sensitive phenomenon, strongly linked to both the underlying crystal symmetry and dynamic spin fluctuations.

5.6. Scalar Spin Chirality Induced Enhancement

The theoretical work presented in this section was performed by Dr. Tom G. Saunderson and Dr. Lichuan Zhang. In addition to the well-established scattering-driven processes contributing to spin-orbit torque (SOT) generation, we propose an alternative mechanism: chirality-induced orbital current generation, influenced by spin fluctuations both across and below T_N.

In this mechanism, the inherent chiral magnetic structure in NCAFMs facilitates an asymmetric redistribution of electronic states, generating an orbital current that is further modulated by thermally driven spin fluctuations.

This idea is strongly supported by recent theoretical predictions [107] and experimental demonstrations [108] of orbital magnetism induced by magnonic excitations, where collective spin-wave modes mediate orbital responses in complex magnetic systems.

Given the fundamental nature of this interaction, such phenomena are not necessarily confined to our specific NCAFM, but may represent a general feature across a broader class of materials. Chirality-induced orbital current generation could thus be a universal mechanism contributing to orbital Hall effect (OHE) enhancement in NCAFMs, opening new avenues for spintronic device design based on orbital transport phenomena.

We extend this theoretical framework to Mn_3NiCuN. Our observations indicate that scalar spin chirality (SSC), arising from fluctuating spins, increases progressively with temperature up to T_N and then rapidly diminishes beyond T_N. This behavior coincides with the emergence and suppression of the chirality-induced orbital Hall current, as shown in Fig. 5.9(c).

Notably, SSC predicts $\sigma_{OH} = 0$ at $T = 0$ K. For better visualization, this theoretical curve has been vertically shifted in the figure.

In contrast, the red curve in Fig. 5.9(c) represents the mean-field behavior of the OHE originating from the suppression of magnetic order across the phase transition. The interplay between these two mechanisms—SSC-driven and mean-field contributions—may explain the observed peak in the magnitude of the orbital Hall current near T_N, as indicated by the black curve in Fig. 5.9(c).

Importantly, the predicted SSC-driven OHE is expected to scale as T^2 at low temperatures (see Section A.6), a trend that matches our experimental findings shown in Fig. 5.8(b).

Furthermore, Mn_3NiCuN stabilizes the Γ_{4g} magnetic phase, characterized by an all-in-all-out spin configuration [Fig. 5.4(a)]. Future studies aiming to stabilize alternative phases, such as Γ_{5g}, or exploring other NCAFMs with different chiralities (e.g., Mn_3Sn), could offer deeper insights into the role of spin chirality in orbital current generation.

Altogether, these results highlight a novel pathway for enhancing orbital currents through fluctuating spins, offering valuable new perspectives for the control of spin and orbital transport phenomena in a wide variety of antiferromagnetic systems.

In conclusion, we report an unprecedented temperature dependence of strong spin-orbit torques in the epitaxial noncollinear antiferromagnetic thin film Mn_3NiCuN. The SOT efficiency per unit current density, ξ^j_{DL}, reaches approximately 0.3, peaking near $T_N \approx 210$ K. This value significantly surpasses those typically achieved using conventional heavy metals such as Pt.

Our experimental findings strongly suggest that the dominant contribution to the observed torques above the magnetic phase transition arises from the orbital Hall effect, consistent with DFT predictions. Below T_N, both extrinsic skew-scattering mechanisms and chirality-enhanced orbital current generation appear to play critical roles.

These insights open exciting opportunities for future research and technological applications, particularly in magnetic random-access memory (MRAM) devices, where leveraging large spin-orbit torques could enable more efficient and scalable architectures.

5.7. ST-FMR Measurements

The work presented in this section was done in collaboration with Dr. Durgesh Kumar. Spin-torque ferromagnetic resonance (ST-FMR) serves as the resonant counterpart to second harmonic Hall (SHH) measurements, providing a complementary method to probe current-induced torques in magnetic heterostructures. In the ST-FMR technique, a direct current (DC) voltage is measured while an external magnetic field is swept at an angle ϕ (typically 45°) relative to the direction of the applied radio frequency (RF) current.

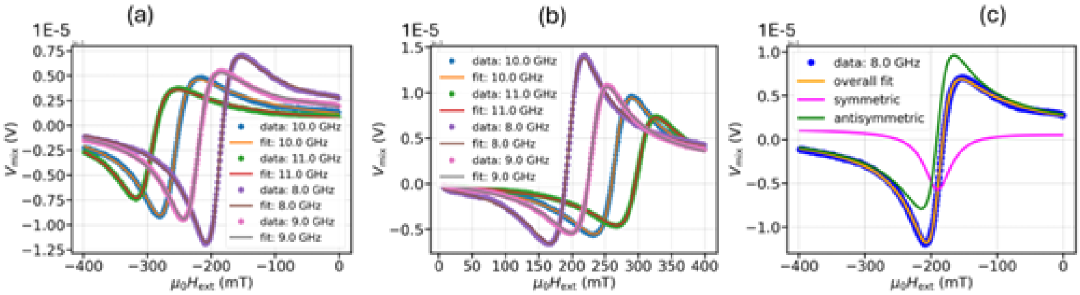

Figure 5.10.: ST-FMR data for Mn_3NiCuN/Cu/Py/Cu/cap at room temperature. V_{mix} for the negative (a) and positive (b) field sweep at different frequencies. (c) Fitting of the V_{mix} with the symmetric (V_S, pink curve) and anti-symmetric (V_A, green curve) Lorentzian functions. Large V_S signifies substantial damping-like torques, consistent with SHH measurements.

As described in Section 3.6, the RF current generates an oscillating spin-orbit torque, exciting the magnetization into resonance. This resonance condition allows precise characterization of the various torques acting on the magnetic layer.

The detection mechanism in ST-FMR relies on homodyne mixing between the RF current and the anisotropic magnetoresistance (AMR) of the sample. This mixing generates a measurable DC voltage spectrum.

ST-FMR measurements were performed across a range of frequencies (8–11 GHz). Fig. 5.10(a) and (b) show the responses to negative and positive H_{ext}, respectively.

Each response can be decomposed into two Lorentzian components: - A symmetric component (V_S), attributed primarily to the damping-like torque. - An anti-symmetric component (V_A), typically arising from the Oersted field and/or field-like torque.

The sizable V_S component observed for the 15 nm thick Mn_3NiCuN layer indicates efficient spin and/or orbital current generation, consistent with the SHH measurements.

The agreement between the two independent experimental techniques (SHH and ST-

FMR) provides strong evidence for the dominant role of orbital and spin transport mechanisms in our system. Furthermore, the significant spin-orbit torque efficiency confirmed through ST-FMR underscores the potential of Mn_3NiCuN-based heterostructures for next-generation spintronic devices.

5.8. The Contribution of Self-Torque from Py

The work presented in this section was performed in collaboration with Dr. Durgesh Kumar. To isolate the contribution of Mn_3NiCuN to spin-orbit torque (SOT) generation and rule out the influence of self-induced torques, we performed control measurements using the second-harmonic Hall (SHH) technique on a reference sample.

This reference stack, Si/SiO_2(sub)/Ta(1)/Cu(2)/Py(5)/Cu(2)/MgO(1.5)/Ta(1.5), was structurally similar to the main samples studied but lacked the Mn_3NiCuN layer.

By comparing the results from this control sample with those from our primary Mn_3NiCuN-based heterostructures, we could determine whether the observed SOT originated from Mn_3NiCuN or alternative mechanisms, such as self-induced torques arising from interfacial effects.

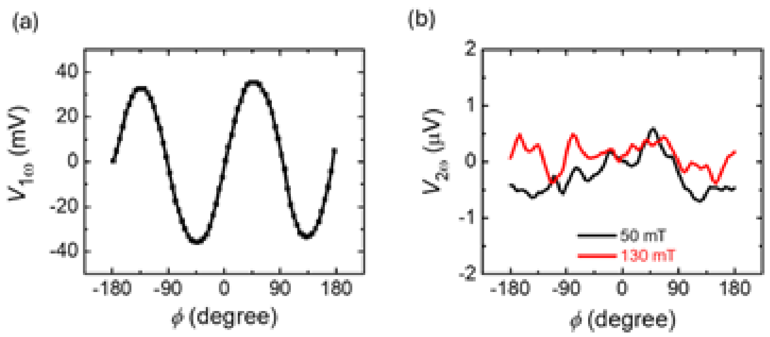

Figure 5.11.: First and second harmonic Hall voltages for Si/SiO_2/Ta(1)/Cu(2)/Py(5)/Cu(2)/MgO(1.5)/Ta(1.5) measured at 300 K with applied magnetic fields of 50 mT (black) and 130 mT (red).

As shown in Fig. 5.11(a), the first-harmonic voltage exhibited a clear $\sin(2\phi)$ dependence, consistent with the planar Hall effect (PHE) and confirming the expected magnetotransport response in the absence of additional torque-driven contributions.

However, the second-harmonic voltage (shown in Fig. 5.11(b)) for H_{ext} values of 50 mT and 130 mT displayed no significant angular or field dependence typically associated with SOT effects. This behavior stands in stark contrast to the Mn_3NiCuN-based samples, where a pronounced SOT-induced second-harmonic signal was observed. These findings strongly indicate that self-induced torques, such as those generated by the Rashba-Edelstein effect or interfacial spin-orbit coupling, are negligible in our samples, especially given the Py thickness and its adjacent nonmagnetic layers. Furthermore, even if self-torques were present, they would be unlikely to exhibit a significant variation around the Néel transition temperature of Mn_3NiCuN.

Thus, we conclude that the SOT observed in our main heterostructures can be attributed solely to the Mn_3NiCuN layer, providing direct and robust evidence for its crucial role in spin-orbit and orbital torque generation.

6. Conclusion and Outlook

6.1. Conclusion

This thesis has investigated the interplay between spin textures, electronic transport, and current-induced torques in the noncollinear antiferromagnet $Mn_3Ni_{0.35}Cu_{0.65}N$ (Mn_3NiCuN). The primary motivation was twofold: to understand the fundamental origins of the anomalous Hall effect (AHE) in noncollinear antiferromagnets (NCAFMs) beyond conventional dipolar magnetism, and to explore the generation of efficient spin-orbit torques (SOTs) for potential application in next-generation spintronic devices. While previous experimental reports established the presence of large AHE in NCAFMs such as Mn_3Sn and Mn_3Ge, a definitive experimental substantiation of the underlying mechanisms remained lacking. In particular, earlier studies often employed perpendicular field geometries that entangled contributions from residual magnetization with intrinsic symmetry-driven Hall effects, leaving open questions regarding the precise origin of the observed signals.

To address these limitations, a detailed experimental protocol was developed, wherein the anomalous Hall effect was systematically probed not only with out-of-plane fields but also under in-plane field rotations. This approach enabled disentanglement of the magnetization-related signal from higher-order contributions. Remarkably, significant AHE signals were detected even in the in-plane geometry, where sensitivity to net magnetization is intrinsically suppressed. This observation provided compelling evidence for the presence of higher-order multipolar contributions, specifically an octupolar moment, in governing the Hall response.

A detailed angular dependence analysis revealed a characteristic 120° periodicity of the in-plane AHE with respect to the azimuthal angle ϕ. This symmetry was successfully explained by considering the alignment of the octupolar order parameter with six high-symmetry directions in the crystal lattice, as determined by the external magnetic field. Positive and negative projections of the octupolar moment on the measurement plane were shown to result in the observed 120° oscillations in the Hall signal, fully consistent with theoretical models of octupole-driven Berry curvature generation.

In addition to the dominant octupolar signature, finer features were observed in individual Hall hysteresis loops, suggestive of contributions beyond the leading order. These features were modeled phenomenologically by superposing a hyperbolic tangent function (representing octupolar switching) with a Gaussian term (representing scalar spin chirality, SSC contributions). The excellent agreement between the modeled and experimental curves strongly supports the interpretation of multiple coexisting order parameters influencing the electronic transport properties in Mn_3NiCuN.

Robustness checks were extensively performed. Temperature-dependent studies confirmed the persistence of the in-plane AHE and its symmetry signatures up to the Néel temperature (T_N), with vanishing signal above T_N, reaffirming the magnetic origin of the observed phenomena. Structural characterization via rocking curves and ϕ-scans indicated good crystalline alignment between the film and substrate despite non-ideal epitaxy, ensuring the intrinsic nature of the measured effects. Moreover, the results were reproduced in samples with and without a Pt capping layer, ruling out spurious contributions from the heavy metal layer.

In parallel, the generation of spin-orbit torques was explored through second harmonic Hall measurements and spin-torque ferromagnetic resonance (ST-FMR). Notably, this work provides the first experimental confirmation of orbital Hall effect (OHE) contributions in a NCAFM. A significant enhancement of the damping-like spin-orbit torque was observed near the Néel temperature. The origin of this enhancement could be attributed to two alternative but complementary mechanisms: (i) increased spin and orbital current generation driven by critical fluctuations of the noncollinear antiferromagnetic order, and (ii) spin currents generated by fluctuation-induced scalar spin chirality (SSC). Both mechanisms offer viable explanations for the temperature dependence of the torque efficiency and highlight the complexity of angular momentum generation in NCAFMs.

Altogether, the results presented in this thesis establish Mn_3NiCuN as a model material system for studying higher-order Berry curvature effects, multipolar-driven transport phenomena, and fluctuation-mediated spin-orbit torques in NCAFM systems.

6.2. Outlook

The findings of this thesis open multiple promising avenues for further research, both on a fundamental level and toward practical spintronic applications.

From a fundamental perspective, although clear signatures of octupolar and SSC contributions to the AHE have been experimentally demonstrated, direct microscopic visualization of the underlying spin textures remains an open challenge. Techniques such as spin-polarized scanning tunneling microscopy (SP-STM), Lorentz transmission electron microscopy (LTEM), or spin-resolved photoemission spectroscopy (SARPES) could provide real-space or momentum-space confirmation of the chiral spin configurations and Berry curvature distributions. In particular, orbital-resolved spectroscopy techniques would be instrumental in directly detecting the emergence of orbital Hall currents, further substantiating the proposed mechanisms.

Extending the experimental framework developed here to other NCAFMs with different crystal symmetries—such as Mn_3Sn, Mn_3Ge, Mn_3Pt, or newly synthesized compounds—could help elucidate the role of lattice symmetry, spin fluctuations, and orbital character in controlling spin transport phenomena. Comparative studies between 2D, 3D, metallic, and insulating NCAFMs would offer valuable insights into the universality and material dependence of fluctuation-enhanced torque generation.

From a dynamical perspective, the use of ultrafast pump-probe techniques, such as time-resolved magneto-optical Kerr effect (TR-MOKE) or terahertz emission spectroscopy, could shed light on the timescales and dynamics of fluctuation-mediated torques. Investigating the temperature and frequency dependence of SOT efficiencies across the critical region near T_N could provide critical information on how spin and orbital currents respond to dynamic fluctuations, revealing nontrivial relaxation and coherence phenomena.

On the applied side, the large, fluctuation-enhanced spin-orbit torques demonstrated in Mn_3NiCuN suggest that NCAFMs could serve as robust building blocks for next-generation SOT-MRAM technologies. Their absence of stray fields, immunity to external magnetic perturbations, and ultrafast dynamics offer distinct advantages over conventional ferromagnetic systems. Engineering artificial multilayers or hybrid structures combining NCAFMs with heavy metals or topological materials could allow further enhancement and tunability of torques. The possibility of electrically controlling multiple order parameters (octupolar, SSC) in a single material system opens new pathways toward multifunctional spintronic devices capable of programmable logic and memory operations.

Finally, the broader conceptual lesson of this work is that critical phenomena, such as spin fluctuations and multipolar ordering, are not merely nuisances that hinder magnetic ordering or coherence. Rather, they are active resources that can be harnessed to enhance spin transport, manipulate angular momentum, and enable entirely new classes of device functionalities. Systematic control of fluctuation spectra—via strain, chemical substitution, gating, or light excitation—may thus offer powerful tools for tuning and optimizing spin-orbitronics based on noncollinear antiferromagnets.

In conclusion, this thesis provides a foundational step toward understanding and exploiting the rich interplay of spin texture, criticality, and transport in NCAFMs, paving the way for future advances in both fundamental condensed matter physics and spintronic device engineering.

A. Appendix

A.1. Data Analysis

A systematic study of magnetic field dependent Hall effect was conducted at different orientations of magnetic field with respect to the crystal axis of the sample in the kagome plane in steps of $\phi = 15°$. Each measurement consists of application of DC current source and the subsequent measurement of the Hall voltage after a time delay. Multiple current application, both positive and negative were applied to (i) obtain a larger data set and increase the signal, and (ii) to eliminate joule heating related effects by processing the positive and negative currents.

The symmetric $R_{xy}^{Sym}(B)$ and anti-symmetric $R_{xy}^{Anti-Sym.}(B)$ components of the Hall resistance as a function of magnetic field B are defined,

$$R_{xy}^{Anti-Sym.}(B) = \frac{V_{xy}(B) - V_{xy}(-B)}{2I_{xx}}, \tag{A.1}$$

$$R_{xy}^{Sym}(B) = \frac{V_{xy}(B) + V_{xy}(-B)}{2I_{xx}}, \tag{A.2}$$

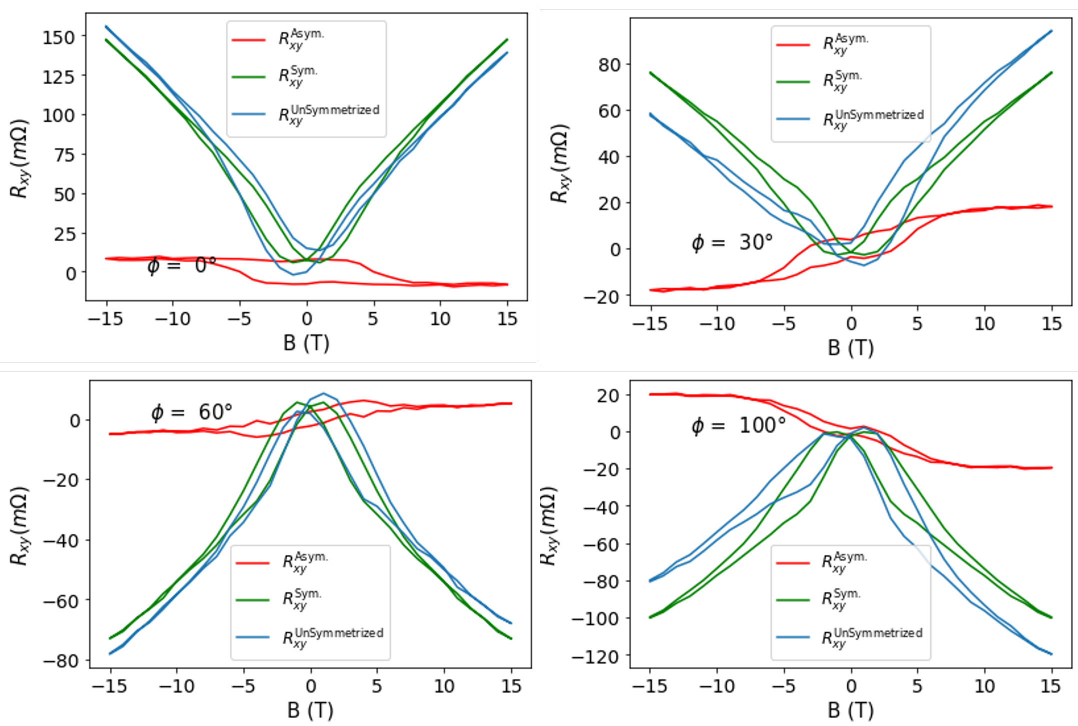

Figure A.1.: Unsymmetrized signal (in blue) decomposed into $R_{xy}^{Anti-Sym}(B)$ (in red) and $R_{xy}^{Sym}(B)$ (in green) components as described in Eq. A.1 and A.2

where $V_{xy}(B)$ is the transverse voltage measured at applied magnetic field B, I_{xx} is the applied longitudinal current. $R_{xy}^{Anti-Sym}$ saturates for all ϕ at 15 T while R_{xy}^{Sym} does not. The unsymmetrized AHE signal $R_{xy}^{Unsymmetrized}$ along with its symmetrized and antisymmetrized components R_{xy}^{Sym} and $R_{xy}^{Anti-Sym}$ respectively is shown in Fig. A.1.

A.2. AHE comparison in select NCAFM

To provide a comparative perspective, we have compiled the anomalous Hall conductivity (AHC) and remanent magnetization (M_{rem}) values reported for several noncollinear antiferromagnets (AFMs) and conventional ferromagnets. The data highlight that a significant AHE can arise in systems with negligible net magnetization, reinforcing the role of nontrivial spin textures and Berry curvature effects in NCAFMs.

Material / Reference	R_{xy} (mΩ)	ρ_{xy} (μΩcm)	σ_{xy} (Ω^{-1}cm^{-1})	M_{rem} (mμ_B/atom)
This work	80	0.16	7 (100 K)	5
Mn_3Ge (Kiyohara et al. [94])	–	1.5	60 (300 K)	20
Mn_3Sn (Nakatsuji et al. [33])	–	4	90 (100 K)	7
Mn_3NiN (Boldrin et al. [37])	–	–	18 (100 K)	50
Mn_3Sn (Xie et al. [123])	1200	2.6	50 (300 K)	45
Mn_3Ir (Iwaki et al. [124])	50	–	40 (300 K)	7
Ni (Ye et al. [125])	–	0.01	600 (300 K)	1000
Fe (Miyasota et al. [126])	–	–	800 (100 K)	2900

Table A.1.: Comparison of transverse resistance, Hall resistivity, Hall conductivity, and remnant magnetization for various materials.

A.3. Hysteresis Decomposition Plots

Additional anomalous Hall hysteresis loops are presented below to further support the analysis discussed in the main text. Each of these loops has been systematically decomposed into contributions arising from the R_{xy}^{Oct} and R_{xy}^{SSC}, following the methodology and analytical formula introduced in Eq. 4.4. This decomposition allows for a clearer identification of the distinct symmetry components contributing to the overall Hall signal and provides further validation of the interpretation presented in the primary discussion. The plots illustrate the robustness and reproducibility of the separation between the two contributions across different field orientations and measurement conditions.

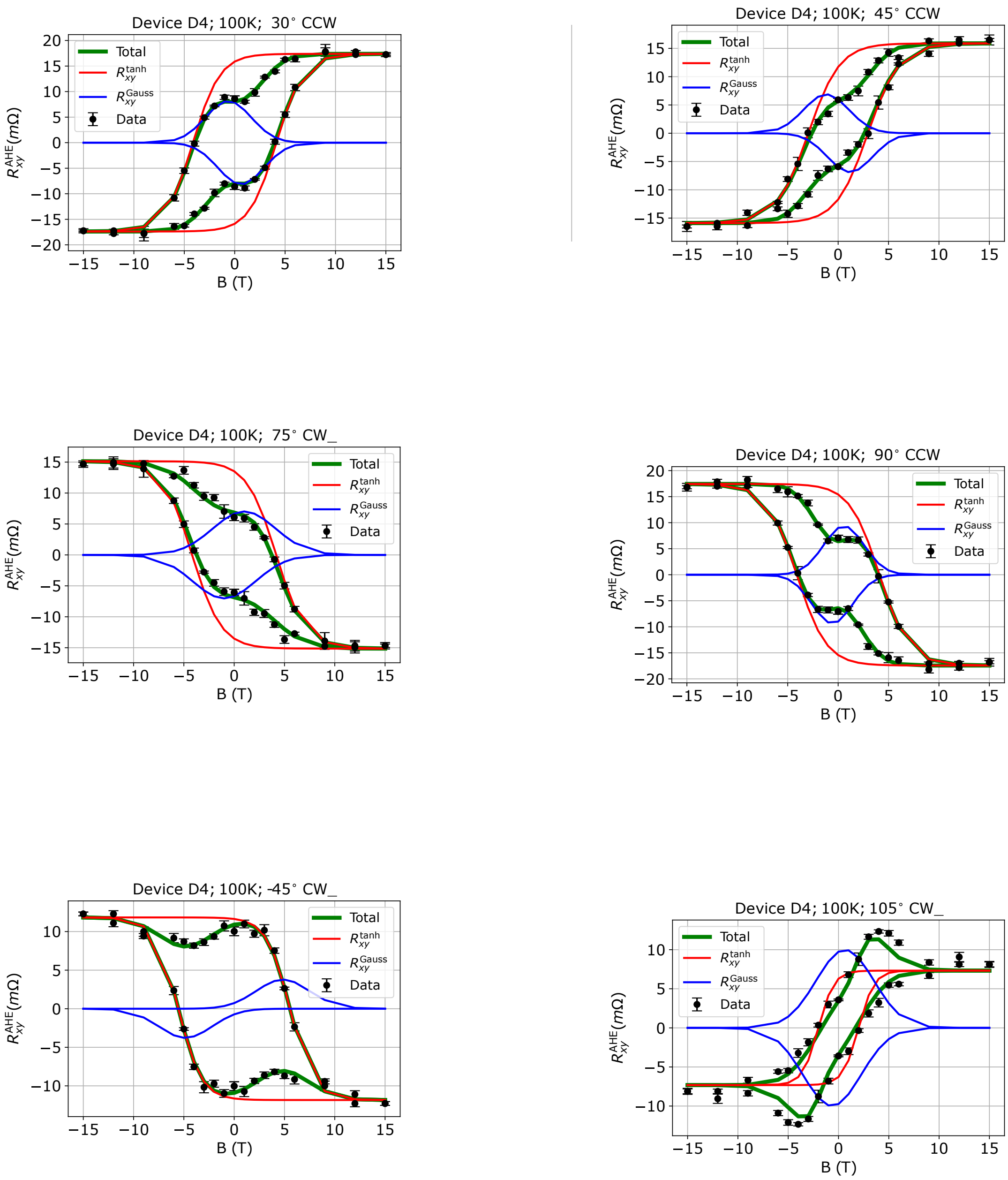

Figure A.2.: $R_{xy}^{Anti-Sym}(B)$ (in black dots) decomposed into R_{xy}^{Oct} (red) and R_{xy}^{SSC} (blue)

A.4. Representation theory approach

A.4.1. Crystallographic properties

The space of group of Mn3NiN is $Pm\overline{3}m$ (No. 221). Its underlying point group is therefore $m\overline{3}m$ (O_h). The magnetic Mn atoms are located in Wyckoff position $3c$ with site symmetry $4/mm.m$. We collect the atomic site positions in the matrix

$$\begin{pmatrix} 0 & 1/2 & 1/2 \\ 1/2 & 0 & 1/2 \\ 1/2 & 1/2 & 0 \end{pmatrix}, \tag{A.3}$$

where each row represents a fractional coordinate vector. All coordinates are represented in the intrinsic coordinate system defined by the crystallographic axes $\vec{a}, \vec{b}$ and $\vec{c}$. Thereby, we follow the conventions of the International Tables of Crystallography. Corresponding to the rows of the atomic site position matrix, we refer to the localized magnetic moments as $\vec{S}_1$, $\vec{S}_2$ and $\vec{S}_3$ respectively. We obtain the the decomposition of the site symmetry

$$\Gamma_{\mathrm{site}} = A_{1g} \oplus E_g, \tag{A.4}$$

which leads us to the magnetic representation

$$\Gamma_{\mathrm{mag}} = \Gamma_{\mathrm{site}} \otimes T_{1g} = T_{1g} \oplus (T_{1g} \oplus T_{2g}) \tag{A.5}$$

We decompose further, into collinear and non-collinear parts

$$\Gamma^{\mathrm{c}}_{\mathrm{mag}} = T_{1g} \tag{A.6}$$

$$\Gamma^{\mathrm{nc}}_{\mathrm{mag}} = T_{1g} \oplus T_{2g}, \tag{A.7}$$

where the collinear term originates from the tensor product with the totally symmetric part of the site representation, i.e., it represents the decoration of each site with an identical magnetic moment. Worth noting: T_{1g} is sometimes also referred to as Γ_4^+ and T_{2g} as Γ_5^+. To find the invariant components of the magnetic representation, we set up the projection operator to the T_{1g} subspace

$$P_{T_{1g}} = \frac{3}{48} \sum_{g \in m\overline{3}m} \chi_{T_{1g}}(g) \Gamma_{\mathrm{mag}}(g) = \begin{pmatrix} 1 & 0 & 0 & 0 & 0 & 0 & 0 & 0 & 0 \\ 0 & \frac{1}{2} & 0 & 0 & 0 & 0 & 0 & \frac{1}{2} & 0 \\ 0 & 0 & \frac{1}{2} & 0 & 0 & \frac{1}{2} & 0 & 0 & 0 \\ 0 & 0 & 0 & \frac{1}{2} & 0 & 0 & \frac{1}{2} & 0 & 0 \\ 0 & 0 & 0 & 0 & 1 & 0 & 0 & 0 & 0 \\ 0 & 0 & \frac{1}{2} & 0 & 0 & \frac{1}{2} & 0 & 0 & 0 \\ 0 & 0 & 0 & \frac{1}{2} & 0 & 0 & \frac{1}{2} & 0 & 0 \\ 0 & \frac{1}{2} & 0 & 0 & 0 & 0 & 0 & \frac{1}{2} & 0 \\ 0 & 0 & 0 & 0 & 0 & 0 & 0 & 0 & 1 \end{pmatrix}. \tag{A.8}$$

The matrix acts on the direct sum $\vec{S}_1 \oplus \vec{S}_2 \oplus \vec{S}_3$. There are three (physically) obvious eigenvectors with eigenvalue equal to 1 that constitute the net magnetization. They are summarized by the quantity

$$\vec{M}_{T_{1g}} = \frac{1}{\sqrt{3}} \begin{pmatrix} S_1^x + S_2^x + S_3^x \\ S_1^y + S_2^y + S_3^y \\ S_1^z + S_2^z + S_3^z \end{pmatrix} . \tag{A.9}$$

Out of these eigenvectors, we can construct the projector

$$P_{M_{T_{1g}}} = \begin{pmatrix} \frac{1}{3} & 0 & 0 & \frac{1}{3} & 0 & 0 & \frac{1}{3} & 0 & 0 \\ 0 & \frac{1}{3} & 0 & 0 & \frac{1}{3} & 0 & 0 & \frac{1}{3} & 0 \\ 0 & 0 & \frac{1}{3} & 0 & 0 & \frac{1}{3} & 0 & 0 & \frac{1}{3} \\ \frac{1}{3} & 0 & 0 & \frac{1}{3} & 0 & 0 & \frac{1}{3} & 0 & 0 \\ 0 & \frac{1}{3} & 0 & 0 & \frac{1}{3} & 0 & 0 & \frac{1}{3} & 0 \\ 0 & 0 & \frac{1}{3} & 0 & 0 & \frac{1}{3} & 0 & 0 & \frac{1}{3} \\ \frac{1}{3} & 0 & 0 & \frac{1}{3} & 0 & 0 & \frac{1}{3} & 0 & 0 \\ 0 & \frac{1}{3} & 0 & 0 & \frac{1}{3} & 0 & 0 & \frac{1}{3} & 0 \\ 0 & 0 & \frac{1}{3} & 0 & 0 & \frac{1}{3} & 0 & 0 & \frac{1}{3} \end{pmatrix} . \tag{A.10}$$

It fulfills $P_{M_{T_{1g}}} P_{T_{1g}} P^{\perp}_{M_{T_{1g}}} = P^{\perp}_{M_{T_{1g}}} P_{T_{1g}} P_{M_{T_{1g}}} = 0$, where $P^{\perp}_{M_{T_{1g}}} = -P_{M_{T_{1g}}}$. The remaining T_{1g} subspace can then be found in

$$P^{\perp}_{M_{T_{1g}}} P_{T_{1g}} P^{\perp}_{M_{T_{1g}}} = \begin{pmatrix} \frac{2}{3} & 0 & 0 & -\frac{1}{3} & 0 & 0 & -\frac{1}{3} & 0 & 0 \\ 0 & \frac{1}{6} & 0 & 0 & -\frac{1}{3} & 0 & 0 & \frac{1}{6} & 0 \\ 0 & 0 & \frac{1}{6} & 0 & 0 & \frac{1}{6} & 0 & 0 & -\frac{1}{3} \\ -\frac{1}{3} & 0 & 0 & \frac{1}{6} & 0 & 0 & \frac{1}{6} & 0 & 0 \\ 0 & -\frac{1}{3} & 0 & 0 & \frac{2}{3} & 0 & 0 & -\frac{1}{3} & 0 \\ 0 & 0 & \frac{1}{6} & 0 & 0 & \frac{1}{6} & 0 & 0 & -\frac{1}{3} \\ -\frac{1}{3} & 0 & 0 & \frac{1}{6} & 0 & 0 & \frac{1}{6} & 0 & 0 \\ 0 & \frac{1}{6} & 0 & 0 & -\frac{1}{3} & 0 & 0 & \frac{1}{6} & 0 \\ 0 & 0 & -\frac{1}{3} & 0 & 0 & -\frac{1}{3} & 0 & 0 & \frac{2}{3} \end{pmatrix} \tag{A.11}$$

Again, three eigenvectors of eigenvalue equal to one can identified. They are summarized by

$$\vec{Q}_{T_{1g}} = \frac{1}{\sqrt{6}} \begin{pmatrix} -2S_1^x + S_2^x + S_3^x \\ S_1^y - 2S_2^y + S_3^y \\ S_1^z + S_2^z - 2S_3^z \end{pmatrix} . \tag{A.12}$$

We continue to look for the T_{2g} representation contained in Γ_{mag}. Since we know that $\ker P_{T_{1g}} = \Gamma_{T_{2g}}$, this irrep only appears once in the decomposition of Γ_{mag}. Therefore,

$$P_{T_{2g}} = -P_{T_{1g}} = \begin{pmatrix} 0 & 0 & 0 & 0 & 0 & 0 & 0 & 0 & 0 \\ 0 & \frac{1}{2} & 0 & 0 & 0 & 0 & 0 & -\frac{1}{2} & 0 \\ 0 & 0 & \frac{1}{2} & 0 & 0 & -\frac{1}{2} & 0 & 0 & 0 \\ 0 & 0 & 0 & \frac{1}{2} & 0 & 0 & -\frac{1}{2} & 0 & 0 \\ 0 & 0 & 0 & 0 & 0 & 0 & 0 & 0 & 0 \\ 0 & 0 & -\frac{1}{2} & 0 & 0 & \frac{1}{2} & 0 & 0 & 0 \\ 0 & 0 & 0 & -\frac{1}{2} & 0 & 0 & \frac{1}{2} & 0 & 0 \\ 0 & -\frac{1}{2} & 0 & 0 & 0 & 0 & 0 & \frac{1}{2} & 0 \\ 0 & 0 & 0 & 0 & 0 & 0 & 0 & 0 & 0 \end{pmatrix}. \tag{A.13}$$

By diagonalizing this projection operators, we identify the threefold degenerate subspace represented by

$$\vec{Q}_{T_{2g}} = \frac{1}{\sqrt{2}} \begin{pmatrix} S_2^x - S_3^x \\ S_3^y - S_1^y \\ S_1^z - S_2^z \end{pmatrix}. \tag{A.14}$$

In terms of those, the magnetic state can be parameterized as

$$\begin{pmatrix} \vec{S}_1 \\ \vec{S}_2 \\ \vec{S}_3 \end{pmatrix} = \mathcal{B} \begin{pmatrix} \vec{M}_{T_{1g}} \\ \vec{Q}_{T_{1g}} \\ \vec{Q}_{T_{2g}} \end{pmatrix} \tag{A.15}$$

where $\mathcal{B}$ is an orthogonal transformation.

A.4.2. Useful relations

Since the transformation to the invariant basis is orthogonal, we have the property that

$$3 = \sum_i \|\vec{S}_i\|^2 = \|\vec{M}_{T_{1g}}\|^2 + \|\vec{Q}_{T_{1g}}\|^2 + \|\vec{Q}_{T_{2g}}\|^2, \tag{A.16}$$

if the individual magnetic moments were normalized to unit length. Further, one finds the relations

$$\mathcal{H} \equiv \vec{S}_1 \cdot \vec{S}_2 + \vec{S}_2 \cdot \vec{S}_3 + \vec{S}_3 \cdot \vec{S}_1 = \|\vec{M}_{T_{1g}}\|^2 - \frac{1}{2}\left(\|\vec{Q}_{T_{1g}}\|^2 + \|\vec{Q}_{T_{2g}}\|^2\right). \tag{A.17}$$

Implementing the normalization constraint, we therefore have

$$\|\vec{M}_{T_{1g}}\|^2 = 1 + \frac{2}{3}\mathcal{H}. \tag{A.18}$$

Further, we have

$$\vec{K}^{-}_{T_{1g}} \equiv \vec{M}_{T_{1g}}/\sqrt{3} - \sqrt{2/3}\ \vec{Q}_{T_{1g}} = \begin{pmatrix} S_{1,x} \\ S_{2,y} \\ S_{3,z} \end{pmatrix} \tag{A.19}$$

and

$$\vec{K}^{+}_{T_{1g}} = 2\vec{M}_{T_{1g}}/\sqrt{3} + \sqrt{2/3}\ \vec{Q}_{T_{1g}} = \begin{pmatrix} S_{2,x} + S_{3,x} \\ S_{3,y} + S_{1,y} \\ S_{1,z} + S_{2,z} \end{pmatrix} \tag{A.20}$$

These relations can be inverted to give

$$\begin{aligned} \vec{M}_{T_{1g}} &= \frac{1}{\sqrt{3}}\left(\vec{K}^{+}_{T_{1g}} + \vec{K}^{-}_{T_{1g}}\right) \\ \vec{Q}_{T_{1g}} &= \frac{1}{\sqrt{6}}\left(\vec{K}^{+}_{T_{1g}} - 2\vec{K}^{-}_{T_{1g}}\right) \end{aligned} \tag{A.21}$$

For the absolute magnitude of these vectors, we find

$$\|\vec{K}^{-}_{T_{1g}}\|^2 = \frac{1}{3}\|\vec{M}_{T_{1g}}\|^2 + \frac{2}{3}\|\vec{Q}_{T_{1g}}\|^2 - 2\sqrt{2}/3\ \vec{M}_{T_{1g}} \cdot \vec{Q}_{T_{1g}} \tag{A.22}$$

$$\|\vec{K}^{+}_{T_{1g}}\|^2 = \frac{4}{3}\|\vec{M}_{T_{1g}}\|^2 + \frac{2}{3}\|\vec{Q}_{T_{1g}}\|^2 + 4\sqrt{2/3}\vec{M}_{T_{1g}} \cdot \vec{Q}_{T_{1g}} \tag{A.23}$$

We need one higher order term:

$$\|\vec{M}_{T_{1g}}\|^4 = \left(1 + \frac{2}{3}\mathcal{H}\right)^2 = 1 + \frac{4}{3}\mathcal{H} + \frac{4}{9}\mathcal{H}^2. \tag{A.24}$$

A.4.3. Magnetic interactions

The energy density of the magnetic state is parameterized by

$$\mathcal{F} = \Gamma_{\text{mag}} \odot \Gamma_{\text{mag}}\ |_{A_{1g}} \tag{A.25}$$

The symmetrized tensor product is given by

$$\Gamma_{\text{mag}} \odot \Gamma_{\text{mag}} = 4A_{1g} \oplus 2A_{2g} \oplus 6E_g \oplus 3T_{1g} \oplus 6T_{2g}. \tag{A.26}$$

This means there are four possible invariant couplings at second order. We have

$$T_{1g} \odot T_{1g}|A_{1g} = 1 \tag{A.27}$$

$$T_{2g} \odot T_{2g}|A_{1g} = 1 \tag{A.28}$$

Combining this result with a look into the basis functions from the character table, we can immediately deduce the invariants $\|\vec{M}_{T_{1g}}\|^2$, $\|\vec{Q}_{T_{1g}}\|^2$ and $\|\vec{Q}_{T_{2g}}\|^2$. Since

$T_{1g} \otimes T_{2g}|A_{1g} = 0$, the remaining, unknown invariant is therefore hidden in the symmetrized product of $\vec{M}_{T_{1g}}$ and $\vec{Q}_{T_{1g}}$. The natural candidate is $\vec{Q}_{T_{1g}} \cdot \vec{M}_{T_{1g}}$. We therefore arrive at

$$\mathcal{F} = f_2\|\vec{M}_{T_{1g}}\|^2 + f_3\|\vec{Q}_{T_{1g}}\|^2 + f_4\vec{Q}_{T_{1g}} \cdot \vec{M}_{T_{1g}} + f_5\|\vec{Q}_{T_{2g}}\|^2, \tag{A.29}$$

with material and temperature dependent parameters f_i. We make use of Molien's formula to determine the number of higher order invariants:

$$\begin{aligned}
&\sum_{n=0}^{\infty} \Gamma_{\mathrm{mag}}^{\odot n}|A_{1g}\; t^n = \frac{1}{|m\bar{3}m|} \sum_{g \in m\bar{3}m} \frac{1}{\det(-t\; \Gamma_{\mathrm{mag}}(g))} \\
&= \frac{1}{3\,(-t^9 + 3t^6 - 3t^3 + 1)} \\
&+ \frac{1}{4(1-t)\,(-t^8 - 2t^6 + 2t^2 + 1)} \\
&+ \frac{1}{4(t+1)\,(t^8 - 4t^6 + 6t^4 - 4t^2 + 1)} \\
&+ \frac{1}{8\,(-t^9 - 3t^8 + 8t^6 + 6t^5 - 6t^4 - 8t^3 + 3t + 1)} \\
&+ \frac{1}{24\,(-t^9 + 9t^8 - 36t^7 + 84t^6 - 126t^5 + 126t^4 - 84t^3 + 36t^2 - 9t + 1)} \\
&= 1 + 4t^2 + 4t^3 + 30t^4 + 42t^5 + 150t^6 + 235t^7 + 592t^8 + O\left(t^9\right)
\end{aligned} \tag{A.30}$$

Besides the 4 terms at the second order which we have just determined, there are thus 30 new terms at fourth order. From those terms, $10 = 4(4+1)/2$ are just obtained from taking all possible quadratic combinations of second order terms. We know already that the interactions seem to favor the $\vec{Q}_{T_{1g}}$ order parameter. Therefore, a first approach would be to disregard the possible interactions between different irreducible components at the fourth order.

$$T_{1g}^{\odot 4}|A_{1g} = 2 \tag{A.31}$$

$$T_{2g}^{\odot 4}|A_{1g} \leq 4 \tag{A.32}$$

The natural canditates are

$$\mathcal{F}_1 = \alpha_1\|\vec{M}_{T_{1g}}\|^4 - \beta_1\|\vec{M}_{T_{1g}}\|^2 + \gamma_1((M_{T_{1g}}^x)^4 + (M_{T_{1g}}^y)^4 + (M_{T_{1g}}^z)^4) \tag{A.33}$$

$$\mathcal{F}_2 = \alpha_2\|\vec{Q}_{T_{1g}}\|^4 - \beta_2\|\vec{Q}_{T_{1g}}\|^2 + \gamma_2((Q_{T_{1g}}^x)^4 + (Q_{T_{1g}}^y)^4 + (Q_{T_{1g}}^z)^4) \tag{A.34}$$

$$\mathcal{F}_3 = \alpha_3\|\vec{Q}_{T_{2g}}\|^4 - \beta_3\|\vec{Q}_{T_{2g}}\|^2 + \gamma_3((Q_{T_{2g}}^x)^4 + (Q_{T_{2g}}^y)^4 + (Q_{T_{2g}}^z)^4) \tag{A.35}$$

The numerical evidence seems to suggest that the Q^4 terms are completely negligible. Further, the $\|\vec{Q}_{T_{2g}}\|^2$ component in the energy can be eliminated by the normalization constraint. We therefore propose the following energy density:

$$\begin{aligned}
\mathcal{F} =& f_1\|\vec{M}_{T_{1g}}\|^4 + f_2\|\vec{M}_{T_{1g}}\|^2 + f_3\|\vec{Q}_{T_{1g}}\|^2 \\
&+ f_4\; \vec{Q}_{T_{1g}} \cdot \vec{M}_{T_{1g}} - \mu_{\mathrm{Mn}}\sqrt{3}\vec{B} \cdot \vec{M}_{T_{1g}},
\end{aligned} \tag{A.36}$$

where $\vec{B}$ represents an external magnetic field, μ_{Mn} is the magnetic moment of the Manganese atoms. The functional is to be minimized under the constraint of fixed-magnitude moments. Additionally one can consider the presence of a nonzero orbital magnetization:

$$\delta\mathcal{F}_{\mathrm{orb}} = -\vec{B} \cdot \vec{M}_{\mathrm{orb}}, \tag{A.37}$$

where we can write,

$$\vec{M}_{\mathrm{orb}} = \mu^{(1)}_{\mathrm{orb}} \vec{M}_{T_{1g}} + \mu^{(2)}_{\mathrm{orb}} \vec{Q}_{T_{1g}}, \tag{A.38}$$

to first order in the magnetic moments.

A.4.4. Mapping to a lattice Heisenberg model

The relations derived in the previous section enable us to identify

$$\begin{aligned} \mathcal{F} &= E_0 + J_2\mathcal{H} + J_4\mathcal{H}^2 + K_- \|\vec{K}^-_{T_{1g}}\|^2 + K_+ \|\vec{K}^+_{T_{1g}}\|^2 \\ &= f_1 \|\vec{M}_{T_{1g}}\|^4 + f_2 \|\vec{M}_{T_{1g}}\|^2 + f_3 \|\vec{Q}_{T_{1g}}\|^2 + f_4 \vec{M}_{T_{1g}} \cdot \vec{Q}_{T_{1g}}, \end{aligned} \tag{A.39}$$

where we find

$$E_0 = \frac{3J_2}{2} - \frac{9}{4}J_4 \tag{A.40}$$

$$f_1 = \frac{9J_4}{4} \tag{A.41}$$

$$f_2 = \frac{3}{2}J_2 - \frac{9}{2}J_4 + \frac{1}{3}K_- + \frac{4}{3}K_+ \tag{A.42}$$

$$f_3 = \frac{2}{3}(K_- + K_+) \tag{A.43}$$

$$f_4 = -\frac{2\sqrt{2}}{3}K_- + \frac{4\sqrt{2}}{\sqrt{3}}K_+, \tag{A.44}$$

and for the corresponding inverse transformation

$$J_2 = \frac{4f_1}{3} + \frac{2f_2}{3} + \frac{-4\left(2+\sqrt{3}\right) f_3 - 3\sqrt{2} f_4}{6 + 12\sqrt{3}} \tag{A.45}$$

$$\begin{aligned} J_4 &= \frac{4f_1}{9} \\ K^+ &= \frac{3f_3}{2\left(1+2\sqrt{3}\right)} + \frac{3f_4}{2\sqrt{2}\left(1+2\sqrt{3}\right)} \\ K^- &= \frac{3\sqrt{3}f_3}{1+2\sqrt{3}} - \frac{3f_4}{2\sqrt{2}\left(1+2\sqrt{3}\right)} \\ E_0 &= f_1 + f_2 + \frac{-4\left(2+\sqrt{3}\right) f_3 - 3\sqrt{2} f_4}{4 + 8\sqrt{3}}. \end{aligned} \tag{A.46}$$

From DFT, we have obtained

$$f_1 = 106 \pm 2.6 \tag{A.47}$$
$$f_2 = -28.2 \pm 0.77 \tag{A.48}$$
$$f_3 = -0.123 \pm 0.0020 \tag{A.49}$$
$$f_4 = -0.321 \pm 0.0092 \tag{A.50}$$

for Mn3(CuNi)N. This leads to

$$J_2 = 123 \pm 3.5 \tag{A.51}$$
$$J_4 = 47.2 \pm 1.1 \tag{A.52}$$
$$K^+ = -0.0692 \pm 0.0031 \tag{A.53}$$
$$K^- = -0.1183 \pm 0.0023 \tag{A.54}$$

A.4.5. Electric conductivity tensor

The electric conductivity tensor is a polar tensor of second rank, i.e.,

$$\sigma = T_{1u} \otimes T_{1u} = A_{1g} + E_g + T_{2g} + T_{1g}. \tag{A.55}$$

We decompose $\sigma = \sigma_+ + \sigma_-$ into symmetric and antisymmetric parts (σ_+ and σ_- respectively):

$$\sigma_+ = A_{1g} + E_g + T_{2g} \tag{A.56}$$
$$\sigma_- = T_{1g}, \tag{A.57}$$

and assign the following names

$$\sigma|_{A_{1g}} = \text{Isotropic longitudinal conductivity} \tag{A.58}$$
$$\sigma|_{E_g} = \text{Anisotropic longitudinal conductivity} \tag{A.59}$$
$$\sigma|_{T_{1g}} = \text{(Anomalous) Hall conductivity} \tag{A.60}$$
$$\sigma|_{T_{2g}} = \text{Planar Hall conductivity} \tag{A.61}$$

Further, we define the Hall conductivity as the off-diagonal elements

$$\sigma^{\mathrm{HC}} = \sigma|_{T_{1g}} + \sigma|_{T_{2g}}, \tag{A.62}$$

with $\sigma^{\mathrm{AHC}} = \sigma_-^{\mathrm{HC}} = T_{1g}$ and $\sigma^{\mathrm{PHC}} = \sigma_+^{\mathrm{HC}} = T_{2g}$. Up to linear order in the magnetic moments, there is thus three invariant terms, and they are given by

$$\sigma^{\mathrm{AHC}} = \sigma|_{T_{1g}} = (\sigma_{[yz]}, \sigma_{[zx]}, \sigma_{[xy]}) = \gamma_{\mathrm{AHE}}\ \vec{M}_{T_{1g}} + \gamma_{\mathrm{CHE}}\ \vec{Q}_{T_{1g}} \tag{A.63}$$

Additionally, we can now consider what happens if symmetries of the systems are broken, for example due to the presence of an interface. If the perturbation is small, we can model it as the presence of a time-reversal invariant polar vector which is acting upon the system. As such it carries the representation T_{1u} and it can facilate new couplings of the magnetic order parameters into the Hall effect. To investigate this, we can reduce the tensor product of T_{1u} with the irreducible representations carried by the magnetic texture, i.e., T_{1g} and T_{2g}. The lowest nontrivial term has to second order in the components of T_{1u}. We have

$$T_{1u} \odot T_{1u} = A_{1g} + E_g + T_{2g} \tag{A.64}$$

The tensor product with A_{1g} will not lead to new couplings. E_g and T_{2g} of this tensor can however modify the Hall effect. This is because

$$E_g \otimes T_{1g} = T_{1g} + T_{2g} \tag{A.65}$$

$$E_g \otimes T_{2g} = T_{1g} + T_{2g} \tag{A.66}$$

$$T_{2g} \otimes T_{1g} = A_{2g} + E_g + T_{1g} + T_{2g} \tag{A.67}$$

$$T_{2g} \otimes T_{2g} = A_{1g} + E_g + T_{1g} + T_{2g} \tag{A.68}$$

Not only can these couplings engange other compontents of $\vec{Q}_{T_{1g}}$ and $\vec{M}_{T_{1g}}$, they can also potentially activate components of $\vec{Q}_{T_{2g}}$.

A.4.6. Approximate ground state

Assume $f_1, f_2 > 0$ while $f_3 < 0$ at zero field. Then, the ground states can be obtained from the effective functional

$$\mathcal{F}_{\text{eff}} = -\|\vec{Q}_{T_{1g}}\|^2. \tag{A.69}$$

Due to the normalization constraint, we know that $\|\vec{Q}_{T_{1g}}\|^2 = 3$. One could assume that the groundstate has continuous $SO(3)$ symmetry because of that. This is however not the case, since $SO(3)$ transformations of the $\vec{Q}_{T_{1g}}$ order parameter do not preserve the normalization of the individual moments. As we will see, only a discrete set of magnetic configurations saturate $\|\vec{Q}_{T_{1g}}\|^2 = 3$ while also preserving the individual size of the magnetic moments. With respect to the crystallographic coordinate system, write

$$\vec{Q}_{T_{1g}} = \sqrt{3}\begin{pmatrix} \sin\theta\cos\phi \\ \sin\theta\sin\phi \\ \cos\theta \end{pmatrix}. \tag{A.70}$$

We further set $\vec{Q}_{T_{2g}} = \vec{M}_{T_{2g}} = 0$. Rotating back from the irreps to the spin representation, we find

$$\|\vec{S}_3\|^2 = \frac{1}{4}(5 + 3\cos 2\theta) \overset{!}{=} 1 \tag{A.71}$$

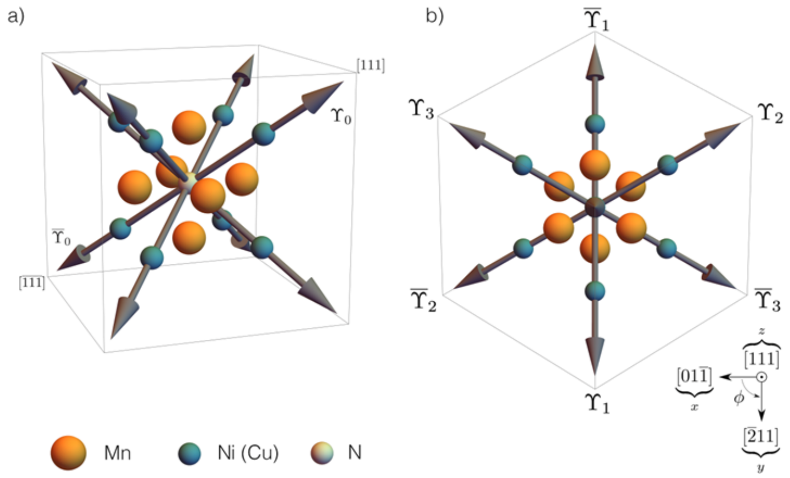

Figure A.3.: Classification of the energy minima in the anisotropy potential $\delta\mathcal{F} = -\|\vec{Q}_{T_{1g}}\|^2$. Fig. a) shows the orientation of the stable equilibrium configurations of the $\vec{Q}_{T_{1g}}$ order parameter in the cubic crystallographic environment. Fig. b) shows the corresponding perspective from a viewpoint in [111] direction. The nomenclature is defined such that Υ_i has a positive projection onto the [111] axis, while $\overline{\Upsilon}_i$ is the time-reversal partner state with a negative projection onto the [111] axis. Further, the projection of $\Upsilon_{i>0}$ onto the [111] plane intersects the position of Mn atom no. i. The Hall signal due to $\overline{\Upsilon}_i$ has the opposite sign as compared to Υ_i. Note the alternating pattern in Fig b).

There are two solutions within the interval $[0, \pi)$:

$$\theta^{+} = \frac{1}{2}\arccos(-1/3), \tag{A.72}$$

$$\theta^{-} = \pi - \frac{1}{2}\arccos(-1/3). \tag{A.73}$$

Inserting this result in the remaining two constraints, we obtain

$$\|\vec{S}_1\|^2_{\theta=\theta^{\pm}} = \|\vec{S}_2\|^2_{\theta=\theta^{\pm}} = 1 \;\Rightarrow\; \cos 2\phi = 0. \tag{A.74}$$

For $\phi \in [0, 2\pi)$, this equation has 4 solutions:

$$\phi_n = (2n-1)\pi/4, \quad n = 1, 2, 3, 4. \tag{A.75}$$

In total, we therefore obtain 8 degenerate ground states:

$$1^+, 2^+, 3^+, 4^+, 1^-, 2^-, 3^-, 4^-. \tag{A.76}$$

In spherical coordinates, the inversion operator acts as $\theta \to \pi - \theta$, $\phi \to \phi + \pi$. We can use this to pair up spin configurations which are related by the time reversal operation, since $T\theta^{\pm} = \theta^{\mp}$, while $T\phi_1 = \phi_3$, and $T\phi_2 = \phi_4$. From now on, we define Υ_i as those equilibrium configurations (for the simplified functional discussed in this section) for which $\vec{Q}_{T_{1g}}$ has a positive projection onto the [111] axis as shown in figure Fig. A.3. The time-reversal partner states are denote by $\overline{\Upsilon}_i$. Further, the projection of $\Upsilon_{i>0}$ onto the [111] plane intersects the position of Mn atom no. i. The Hall signal due to $\overline{\Upsilon}_i$ has the opposite sign as compared to Υ_i. Note the alternating pattern in Fig. A.3 b). In terms of the magnetic moments, the direction of $\vec{Q}_{T_{1g}}$ simply tells us which sublattice contains displays the "all-out" configuraton.

A.5. Numerical details

First principles calculations are performed in three steps. Firstly, the electronic structure is found self-consistently using density functional theory (DFT). Secondly, the Kohn-Sham states are converted to maximally localized Wannier basis (MLWFs). Finally, calculations of the response functions can be performed efficiently within the basis of MLWFs by k-point interpolation.

For the DFT calculation of bulk Mn_3NiCuN the code FLEUR [127], a full-potential linearized augmented plane wave method [128], is used. For the exchange correlation functional we chose the Perdew-Burke-Ernzerhof functional within the generalized gradient approximation [129]. The plane-wave cutoff is $11.6a_0^{-1}$ for the exchange correlation functional and $16.0a_0^{-1}$ for the charge density, where a_0 is the Bohr radius.

The planewave cutoff for the basis functions was $4.0a_0^{-1}$. For Mn and Ni(Cu) the maximum angular momentum expansion is set to $l_{max} = 12$ and the muffin-tin radii for each was set to $2.29a_0$ and for N $l_{max} = 6$ and the muffin tin radii was $1.29a_0$. The lattice parameter for the cubic system is 3.9012Å from Zhao *et al* [130] as shown in Fig. 1(a) of the main text. The $24 \times 24 \times 24$ Monkhorst-Pack k-mesh was sampled in the first Brillouin zone.

From the Bloch wavefunctions obtained from the DFT calculation we construct ML-WFs by using the Wannier90 package [131, 132] interfaced with the code FLEUR [133, 127]. A mesh of 8 by 8 by 8 k-points was used with 166 Bloch states to obtain 78 MLWFs. Initial projections are chosen to be s, p and d states for Mn and Ni and p states for the N atom. The maximum frozen window is set to $4eV$ above the Fermi energy. The Hamiltonian and torque operators are evaluated in the Bloch basis and transformed into the MLWF basis.

By Fourier transforming the tight-binding model into k-space and diagonalizing the Hamiltonian, the electric response of the AHE is evaluated on a dense interpolation k-mesh ($N_k = 256 \times 256 \times 256$),

$$\sigma_{xy}^{\mathrm{AHC}} = \frac{e^2}{\hbar} \sum_n \int_{\mathrm{BZ}} \frac{d^3k}{(2\pi)^3} f_{n\mathbf{k}} \Omega_{n\mathbf{k}}, \tag{A.77}$$

where the Berry curvature, $\Omega_n(\mathbf{k})$, of a state n at point $\mathbf{k}$ is given by [134],

$$\Omega_{n\mathbf{k}} = 2\hbar^2 \sum_{m \neq n} \mathrm{Im} \left[\frac{\langle u_{n\mathbf{k}} | v_y | u_{m\mathbf{k}} \rangle \langle u_{m\mathbf{k}} | v_x | u_{n\mathbf{k}} \rangle}{(E_{n\mathbf{k}} - E_{m\mathbf{k}} + i\eta)^2} \right] \tag{A.78}$$

where $E_{n\mathbf{k}}$ is the energy of a Bloch state with lattice periodic part of Bloch wave function given by $u_{n\mathbf{k}}$, and v_i is the i'th Cartesian component of the velocity operator. For improving the convergence, we set $\eta = 25$meV.

To separate out the three individual contributions to the Hall effect we chose three distinct spin configurations. Each configuration is designed to isolate one term from 2.31 while nullifying the others through symmetry considerations. The methodology for isolating the scalar spin chirality (SSC) contribution requires an additional manipulation. Here, we highlight the steps to extract all components.

1. Firstly, we orient the spins into the ferromagnetic configuration where all the spins point in the same direction, this cancels out the octupole and SSC contributions.

2. Secondly, we consider the standard non-collinear antiferromagnetic ordering with (111) being the kagome plane described in Fig. 1(a) of the main text. This negates contributions from both the dipole and SSC terms.

3. Finally, to extract the SSC contribution, one orients the spins in a non-coplanar configuration. This orientation would typically incorporate effects from both magnetic and octupole terms in the Hall response. To circumvent this, we switch off the spin-orbit coupling term originating from the Dirac equation in the calculation. Such a deactivation enforces a symmetry that negates the dipolar and octupole contributions.

To evaluate the SHE and OHE, the tight binding model is Fourier transformed into k-space and the Hamiltonian diagonalized. They are finally evaluated on a dense interpolation k-mesh ($N_k = 256 \times 256 \times 256$) using the Kubo formulism,

$$\sigma_{nk}^{\mathrm{OH(SH)}} = -e\hbar \int \frac{d^3k}{(2\pi)^3} \sum_{n \neq m} (f_{n\mathbf{k}} - f_{m\mathbf{k}}) \mathrm{Im} \left[\frac{\left\langle u_{n\mathbf{k}} | j_y^{O_z} | u_{m\mathbf{k}} \right\rangle \langle u_{m\mathbf{k}} | v_x | u_{n\mathbf{k}} \rangle}{(E_{n\mathbf{k}} - E_{m\mathbf{k}} + i\eta)^2} \right] \tag{A.79}$$

where e>0 is the electronic charge, $\hbar$ is the reduced Planck constant, $|u_{m\mathbf{k}}\rangle$ is the periodic part of the Bloch state with crystal momentum $\mathbf{k}$, n and m are band indices, E_{nk} is the energy eigenvalue and f_{nk} is the Fermi-Dirac distribution, v_x is the x component of the velocity operator, η is a smearing term used for numerical convenience, which is set to 25 meV. Finally $j_y^{O_z} = (v_y X_z + X_z v_y)/2$ is the conventional orbital(spin) current with $X_z = L_z(S_z)$ where L_z is the z component of the orbital angular momentum operator, and S_z is similarly the z component of the spin operator.

A.6. Scalar spin chirality imprinted by magnon excitation

The impact of magnon excitations on the scalar spin chirality (SSC) was investigated through numerical modeling. To facilitate the analysis, the qualitative behavior of orbital magnetization induced by magnon excitations was evaluated on a monolayer antiferromagnetic kagome lattice. In the employed model, only the nearest-neighbor Heisenberg exchange interaction was considered, and the spin Hamiltonian was ex-

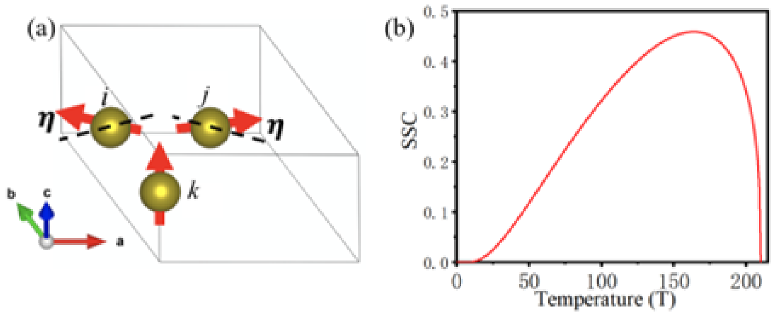

Figure A.4.: (a) Schematic structure of the monolayer antiferromagnetic Kagome lattice under external magnetic field. (b) The value of scalar spin chirality as a function of the temperature.

pressed as:

$$\hat{H} = J \sum_{i,j} \mathbf{S}_i \cdot \mathbf{S}_j \tag{A.80}$$

A value of J = 6 meV was selected, consistent with previous DFT calculations and the experimentally measured Néel temperature of the system (T_N=210 K) [3,12]. The spin operator was assigned a magnitude of S=3/2. The temperature-dependent average spin length was modeled using the relation [13]:

$$S_T = S(1 - T/T_N)^\beta, \tag{A.81}$$

with $\beta = 0.362$

The SSC induced by magnon excitations was subsequently calculated using linear spin wave theory [12,13]. As illustrated in Fig.A.4(a), a small canting angle $\eta = 5°$ was introduced via the application of a weak out-of-plane magnetic field. The computed SSC as a function of temperature is presented in Fig.A.4(b). It was found that the SSC exhibits a quadratic T^2 dependence at low temperatures, consistent with magnonic origin. As the system approaches the Néel temperature, the SSC rapidly diminishes and vanishes at $T = T_N$, consistent with the absence of coherent magnons in the paramagnetic regime. This magnon-mediated generation of scalar spin chirality is predicted to yield a strong orbital response of the spin system, attributable to the mechanism of topological orbital magnetism [12].

Publications list

Parts of this thesis have been published in the following articles:

- **A. Rajan**, T. G. Saunderson, F. R. Lux, R. Yanes Díaz, H. M. Abdullah, A. Bose, B. Bednarz, J.-Y. Kim, D. Go, T. Hajiri, G. Shukla, O. Gomonay, Y. Yao, W. Feng, H. Asano, U. Schwingenschlögl, L. López-Díaz, J. Sinova, Y. Mokrousov, A. Manchon, and M. Kläui,
Revealing the higher-order spin nature of the Hall effect in non-collinear antiferromagnet $Mn_3Ni_{0.35}Cu_{0.65}N$,
(2023), arXiv preprint [arXiv:2304.10747](https://arxiv.org/abs/2304.10747).

- A. Bose, T. G. Saunderson, A. Shahee, L. Zhang, T. Hajiri, **A. Rajan**, D. Go, H. Asano, U. Schwingenschlögl, A. Manchon, Y. Mokrousov, and M. Kläui,
Fluctuation-mediated spin-orbit torque enhancement in the noncollinear antiferromagnet $Mn_3Ni_{0.35}Cu_{0.65}N$,
(2024), arXiv preprint [arXiv:2401.16021](https://arxiv.org/abs/2401.16021).

Curriculum Vitae

Removed due to data privacy.

Bibliography

[1] G. E. Moore, "Moore's Law: Original Draft 1965."

[2] M. M. Waldrop, "The chips are down for Moore's law," *Nature*, vol. 530, pp. 144–147, Feb. 2016.

[3] J. Sinova, S. O. Valenzuela, J. Wunderlich, C. H. Back, and T. Jungwirth, "Spin Hall effects," *Reviews of Modern Physics*, vol. 87, no. 4, pp. 1213–1260, 2015.

[4] H. Chen, Q. Niu, and A. H. MacDonald, "Anomalous Hall Effect Arising from Noncollinear Antiferromagnetism," *Physical Review Letters*, vol. 112, p. 017205, Jan. 2014.

[5] S. Nakatsuji, N. Kiyohara, and T. Higo, "Large anomalous Hall effect in a non-collinear antiferromagnet at room temperature," *Nature*, vol. 527, pp. 212–215, Nov. 2015.

[6] A. K. Nayak, J. E. Fischer, Y. Sun, B. Yan, J. Karel, A. C. Komarek, C. Shekhar, N. Kumar, W. Schnelle, J. Kübler, C. Felser, and S. S. P. Parkin, "Large anomalous Hall effect driven by a nonvanishing Berry curvature in the non-colinear antiferromagnet Mn_3 Ge," *Science Advances*, vol. 2, p. e1501870, Apr. 2016.

[7] K. Zhao, T. Hajiri, H. Chen, R. Miki, H. Asano, and P. Gegenwart, "Anomalous Hall effect in the noncollinear antiferromagnetic antiperovskite $\mathrm{Mn_3Ni_{1-x}Cu_{x}N}$," *Physical Review B*, vol. 100, p. 045109, July 2019.
Publisher: American Physical Society.

[8] N. Nagaosa, J. Sinova, S. Onoda, A. H. MacDonald, and N. P. Ong, "Anomalous Hall effect," *Reviews of Modern Physics*, vol. 82, pp. 1539–1592, May 2010.

[9] A. Bose, T. G. Saunderson, A. Shahee, L. Zhang, T. Hajiri, A. Rajan, D. Go, H. Asano, U. Schwingenschlögl, A. Manchon, Y. Mokrousov, and M. Kläui, "Fluctuation-mediated spin-orbit torque enhancement in the noncollinear antiferromagnet Mn3Ni0.35Cu0.65N," Jan. 2024.
arXiv:2401.16021 [cond-mat].

[10] D. Go, D. Jo, H.-W. Lee, M. Klaeui, and Y. Mokrousov, "Orbitronics: Orbital currents in solids," *EPL (Europhysics Letters)*, 2021.

[11] H. Kontani, T. Tanaka, D. S. Hirashima, K. Yamada, and J. Inoue, "Giant Intrinsic Spin and Orbital Hall Effects in Sr 2 M O 4 (M = Ru , Rh, Mo)," *Physical Review Letters*, vol. 100, p. 096601, Mar. 2008.

[12] T. Tanaka, H. Kontani, M. Naito, T. Naito, D. S. Hirashima, K. Yamada, and J. Inoue, "Intrinsic spin Hall effect and orbital Hall effect in 4 d and 5 d transition metals," *Physical Review B*, vol. 77, p. 165117, Apr. 2008.

[13] H. Ishizuka and N. Nagaosa, "Spin chirality induced skew scattering and anomalous Hall effect in chiral magnets," *Science Advances*, vol. 4, p. eaap9962, Feb. 2018.

[14] D. Wei, Y. Niimi, B. Gu, T. Ziman, S. Maekawa, and Y. Otani, "The spin Hall effect as a probe of nonlinear spin fluctuations," *Nature Communications*, vol. 3, p. 1058, Sept. 2012.

[15] P.-H. Wu, D. Qu, Y.-C. Tu, Y.-Z. Lin, C. L. Chien, and S.-Y. Huang, "Exploiting Spin Fluctuations for Enhanced Pure Spin Current," *Physical Review Letters*, vol. 128, p. 227203, June 2022.

[16] Y. Ou, D. C. Ralph, and R. A. Buhrman, "Strong Enhancement of the Spin Hall Effect by Spin Fluctuations near the Curie Point of Fe x Pt 1 - x Alloys," *Physical Review Letters*, vol. 120, p. 097203, Mar. 2018.

[17] C. Fang, C. Wan, X. Zhang, S. Okamoto, T. Ma, J. Qin, X. Wang, C. Guo, J. Dong, G. Yu, Z. Wen, N. Tang, S. S. P. Parkin, N. Nagaosa, Y. Lu, and X. Han, "Observation of the Fluctuation Spin Hall Effect in a Low-Resistivity Antiferromagnet," *Nano Letters*, vol. 23, pp. 11485–11492, Dec. 2023.

[18] L. Frangou, S. Oyarzún, S. Auffret, L. Vila, S. Gambarelli, and V. Baltz, "Enhanced Spin Pumping Efficiency in Antiferromagnetic IrMn Thin Films around the Magnetic Phase Transition," *Physical Review Letters*, vol. 116, p. 077203, Feb. 2016.

[19] C. Kittel, *Introduction to solid state physics*.
Hoboken, NJ: Wiley, 8th ed ed., 2005.

[20] S. Blundell, *Magnetism in Condensed Matter*.
Oxford University PressOxford, Oct. 2001.

[21] J. M. D. Coey, *Magnetism and Magnetic Materials*.
Cambridge University Press, 1 ed., Jan. 2001.

[22] "Collective electron ferronmagnetism," *Proceedings of the Royal Society of London. Series A. Mathematical and Physical Sciences*, vol. 165, pp. 372–414, Apr. 1938.

[23] J. Kübler and J. Kübler, *Theory of Itinerant Electron Magnetism*.
International Series of Monographs on Physics, Oxford, New York: Oxford University Press, Aug. 2000.

[24] N. Nagaosa and Y. Tokura, "Topological properties and dynamics of magnetic skyrmions," *Nature Nanotechnology*, vol. 8, pp. 899–911, Dec. 2013.

[25] A. Bogdanov and A. Hubert, "Thermodynamically stable magnetic vortex states in magnetic crystals," *Journal of Magnetism and Magnetic Materials*, vol. 138, pp. 255–269, Dec. 1994.

[26] R. Skomski, *Simple Models of Magnetism*.
Oxford University Press, Jan. 2008.

[27] L. Onsager, "Crystal Statistics. I. A Two-Dimensional Model with an Order-Disorder Transition," *Physical Review*, vol. 65, pp. 117–149, Feb. 1944.

[28] J. Takács, “A phenomenological mathematical model of hysteresis,” *COMPEL - The international journal for computation and mathematics in electrical and electronic engineering*, vol. 20, pp. 1002–1015, Dec. 2001.

[29] B. H. Rimmler, B. Pal, and S. S. P. Parkin, “Non-collinear antiferromagnetic spintronics,” *Nature Reviews Materials*, vol. 10, pp. 109–127, Aug. 2024.

[30] D. Khadka, T. R. Thapaliya, S. Hurtado Parra, X. Han, J. Wen, R. F. Need, P. Khanal, W. Wang, J. Zang, J. M. Kikkawa, L. Wu, and S. X. Huang, “Kondo physics in antiferromagnetic Weyl semimetal Mn $_{3+\ x}$ Sn $_{1-\ x}$ films,” *Science Advances*, vol. 6, p. eabc1977, Aug. 2020.

[31] X. Zhou, J.-P. Hanke, W. Feng, F. Li, G.-Y. Guo, Y. Yao, S. Blügel, and Y. Mokrousov, “Spin-order dependent anomalous Hall effect and magneto-optical effect in the noncollinear antiferromagnets Mn 3 X N with X = Ga , Zn, Ag, or Ni,” *Physical Review B*, vol. 99, p. 104428, Mar. 2019.

[32] S. Singh, S. W. D’Souza, J. Nayak, E. Suard, L. Chapon, A. Senyshyn, V. Petricek, Y. Skourski, M. Nicklas, C. Felser, and S. Chadov, “Room-temperature tetragonal non-collinear Heusler antiferromagnet Pt2MnGa,” *Nature Communications*, vol. 7, p. 12671, Aug. 2016.

[33] S. Nakatsuji, N. Kiyohara, and T. Higo, “Large anomalous Hall effect in a non-collinear antiferromagnet at room temperature,” *Nature*, vol. 527, pp. 212–215, oct 2015.

[34] Y. Zhang, J. Železný, Y. Sun, J. Van Den Brink, and B. Yan, “Spin Hall effect emerging from a noncollinear magnetic lattice without spin–orbit coupling,” *New Journal of Physics*, vol. 20, p. 073028, July 2018.

[35] T. Nan, C. X. Quintela, J. Irwin, G. Gurung, D. F. Shao, J. Gibbons, N. Campbell, K. Song, S. Y. Choi, L. Guo, R. D. Johnson, P. Manuel, R. V. Chopdekar, I. Hallsteinsen, T. Tybell, P. J. Ryan, J. W. Kim, Y. S. Choi, P. G. Radaelli, D. C. Ralph, E. Y. Tsymba, M. S. Rzchowski, and C. B. Eom, “Controlling spin current polarization through non-collinear antiferromagnetism,” Dec. 2019.

[36] E. V. Gomonaj, “Magnetostriction and piezomagnetism of noncollinear antiferromagnet Mn $_3$ NiN,” *Phase Transitions*, vol. 18, pp. 93–101, July 1989.

[37] D. Boldrin, I. Samathrakis, J. Zemen, A. Mihai, B. Zou, F. Johnson, B. D. Esser, D. W. McComb, P. K. Petrov, H. Zhang, and L. F. Cohen, “Anomalous Hall effect in noncollinear antiferromagnetic Mn_3NiN thin films,” *Phys. Rev. Mater.*, vol. 3, no. 9, p. 094409, 2019.

[38] D. Boldrin, A. P. Mihai, B. Zou, J. Zemen, R. Thompson, E. Ware, B. V. Neamtu, L. Ghivelder, B. Esser, D. W. McComb, P. Petrov, and L. F. Cohen, “Giant Piezomagnetism in Mn $_3$ NiN,” *ACS Applied Materials & Interfaces*, vol. 10, pp. 18863–18868, June 2018.

[39] K. Takenaka, M. Ichigo, T. Hamada, A. Ozawa, T. Shibayama, T. Inagaki, and K. Asano, “Magnetovolume effects in manganese nitrides with antiperovskite structure,” *Science and Technology of Advanced Materials*, vol. 15, p. 015009, Feb. 2014.

[40] D. Boldrin, E. Mendive-Tapia, J. Zemen, J. B. Staunton, T. Hansen, A. Aznar,

J.-L. Tamarit, M. Barrio, P. Lloveras, J. Kim, X. Moya, and L. F. Cohen, "Multisite Exchange-Enhanced Barocaloric Response in Mn 3 NiN," *Physical Review X*, vol. 8, p. 041035, Nov. 2018.

[41] R. Miki, K. Zhao, T. Hajiri, P. Gegenwart, and H. Asano, "Epitaxial growth and orientation-dependent anomalous Hall effect of noncollinear antiferromagnetic Mn $_3$ Ni $_{0.35}$ Cu $_{0.65}$ N films," *Journal of Applied Physics*, vol. 127, p. 113907, Mar. 2020.

[42] P. Qin, H. Yan, X. Wang, H. Chen, Z. Meng, J. Dong, M. Zhu, J. Cai, Z. Feng, X. Zhou, L. Liu, T. Zhang, Z. Zeng, J. Zhang, C. Jiang, and Z. Liu, "Room-temperature magnetoresistance in an all-antiferromagnetic tunnel junction," *Nature*, vol. 613, pp. 485–489, Jan. 2023.

[43] Y. Pu, G. Shi, Q. Yang, D. Yang, F. Wang, C. Zhang, and H. Yang, "Field-Free Switching of Perpendicular Magnetization by Anisotropic Spin Hall Effect in Mn_3 Ir," *Advanced Functional Materials*, vol. 34, p. 2400143, Aug. 2024.

[44] E. H. Hall, "On a New Action of the Magnet on Electric Currents," *American Journal of Mathematics*, vol. 2, no. 3, pp. 287–292, 1879.
Publisher: Johns Hopkins University Press.

[45] A. Karsenty, "A Comprehensive Review of Integrated Hall Effects in Macro-, Micro-, Nanoscales, and Quantum Devices," *Sensors*, vol. 20, p. 4163, July 2020.

[46] Y. Wang, P. A. Lee, D. M. Silevitch, F. Gomez, S. E. Cooper, Y. Ren, J.-Q. Yan, D. Mandrus, T. F. Rosenbaum, and Y. Feng, "Antisymmetric linear magnetoresistance and the planar Hall effect," *Nature Communications*, vol. 11, p. 216, Jan. 2020.

[47] Z. Feng, X. Zhou, L. Šmejkal, L. Wu, Z. Zhu, H. Guo, R. González-Hernández, X. Wang, H. Yan, P. Qin, X. Zhang, H. Wu, H. Chen, Z. Meng, L. Liu, Z. Xia, J. Sinova, T. Jungwirth, and Z. Liu, "An anomalous Hall effect in altermagnetic ruthenium dioxide," *Nature Electronics*, vol. 5, pp. 735–743, Nov. 2022.

[48] R. Karplus and J. M. Luttinger, "Hall Effect in Ferromagnetics," *Physical Review*, vol. 95, pp. 1154–1160, Sept. 1954.

[49] J. Smit, "The spontaneous hall effect in ferromagnetics I," *Physica*, vol. 21, pp. 877–887, Jan. 1955.

[50] L. Berger, "Side-Jump Mechanism for the Hall Effect of Ferromagnets," *Physical Review B*, vol. 2, pp. 4559–4566, Dec. 1970.

[51] Y. Yao, L. Kleinman, A. H. MacDonald, J. Sinova, T. Jungwirth, D.-s. Wang, E. Wang, and Q. Niu, "First Principles Calculation of Anomalous Hall Conductivity in Ferromagnetic bcc Fe," *Physical Review Letters*, vol. 92, p. 037204, Jan. 2004.

[52] M.-T. Suzuki, T. Koretsune, M. Ochi, and R. Arita, "Cluster multipole theory for anomalous Hall effect in antiferromagnets," *Physical Review B*, vol. 95, p. 094406, Mar. 2017.

[53] K. Ohgushi, S. Murakami, and N. Nagaosa, "Spin anisotropy and quantum Hall effect in the *kagomé* lattice: Chiral spin state based on a ferromagnet,"

Physical Review B, vol. 62, pp. R6065–R6068, Sept. 2000.

[54] S. V. Grigoriev, S. V. Maleyev, A. I. Okorokov, Y. O. Chetverikov, R. Georgii, P. Böni, D. Lamago, H. Eckerlebe, and K. Pranzas, “Critical fluctuations in MnSi near T C : A polarized neutron scattering study,” *Physical Review B*, vol. 72, p. 134420, Oct. 2005.

[55] N. Nagaosa, “Emergent electromagnetism in condensed matter,” *Proceedings of the Japan Academy, Series B*, vol. 95, pp. 278–289, June 2019.

[56] J. Ye, Y. B. Kim, A. J. Millis, B. I. Shraiman, P. Majumdar, and Z. Tešanović, “Berry Phase Theory of the Anomalous Hall Effect: Application to Colossal Magnetoresistance Manganites,” *Physical Review Letters*, vol. 83, pp. 3737–3740, Nov. 1999.

[57] Y. Taguchi, Y. Oohara, H. Yoshizawa, N. Nagaosa, and Y. Tokura, “Spin Chirality, Berry Phase, and Anomalous Hall Effect in a Frustrated Ferromagnet,” *Science*, vol. 291, pp. 2573–2576, Mar. 2001.

[58] H. Wang, Y. Dai, G.-M. Chow, and J. Chen, “Topological hall transport: Materials, mechanisms and potential applications,” *Progress in Materials Science*, vol. 130, p. 100971, Oct. 2022.

[59] G. Kimbell, C. Kim, W. Wu, M. Cuoco, and J. W. A. Robinson, “Challenges in identifying chiral spin textures via the topological Hall effect,” *Communications Materials*, vol. 3, p. 19, Apr. 2022.

[60] L. Tai, B. Dai, J. Li, H. Huang, S. K. Chong, K. L. Wong, H. Zhang, P. Zhang, P. Deng, C. Eckberg, G. Qiu, H. He, D. Wu, S. Xu, A. Davydov, R. Wu, and K. L. Wang, “Distinguishing the Two-Component Anomalous Hall Effect from the Topological Hall Effect,” *ACS Nano*, vol. 16, pp. 17336–17346, Oct. 2022.
Publisher: American Chemical Society.

[61] H. Sabri, B. E. Carlson, S. S. Pershoguba, and J. Zang, “Topological Hall-like behavior of multidomain ferromagnets,” 2024.
Version Number: 2.

[62] D. J. Groenendijk, C. Autieri, T. C. Van Thiel, W. Brzezicki, J. R. Hortensius, D. Afanasiev, N. Gauquelin, P. Barone, K. H. W. Van Den Bos, S. Van Aert, J. Verbeeck, A. Filippetti, S. Picozzi, M. Cuoco, and A. D. Caviglia, “Berry phase engineering at oxide interfaces,” *Physical Review Research*, vol. 2, p. 023404, June 2020.

[63] Y. Ohuchi, J. Matsuno, N. Ogawa, Y. Kozuka, M. Uchida, Y. Tokura, and M. Kawasaki, “Electric-field control of anomalous and topological Hall effects in oxide bilayer thin films,” *Nature Communications*, vol. 9, p. 213, Jan. 2018.
Publisher: Nature Publishing Group.

[64] L. Wang, Q. Feng, H. G. Lee, E. K. Ko, Q. Lu, and T. W. Noh, “Controllable Thickness Inhomogeneity and Berry Curvature Engineering of Anomalous Hall Effect in $SrRuO_3$ Ultrathin Films,” *Nano Letters*, vol. 20, pp. 2468–2477, Apr. 2020.

[65] T. Gilbert, “A phenomenological theory of damping in ferromagnetic materials,” *IEEE Transactions on Magnetics*, vol. 40, pp. 3443–3449, Nov. 2004.

Conference Name: IEEE Transactions on Magnetics.

[66] B. A. Bernevig, T. L. Hughes, and S.-C. Zhang, "Orbitronics: The Intrinsic Orbital Current in \$p\$-Doped Silicon," *Physical Review Letters*, vol. 95, p. 066601, Aug. 2005.
Publisher: American Physical Society.

[67] S. Murakami, N. Nagaosa, and S.-C. Zhang, "Dissipationless Quantum Spin Current at Room Temperature," *Science*, vol. 301, pp. 1348–1351, Sept. 2003.

[68] A. Manchon, J. Železný, I. M. Miron, T. Jungwirth, J. Sinova, A. Thiaville, K. Garello, and P. Gambardella, "Current-induced spin-orbit torques in ferromagnetic and antiferromagnetic systems," *Reviews of Modern Physics*, vol. 91, p. 035004, Sept. 2019.
Publisher: American Physical Society.

[69] H. Ohno, "A window on the future of spintronics," *Nature Materials*, vol. 9, pp. 952–954, Dec. 2010.

[70] I. M. Miron, K. Garello, G. Gaudin, P.-J. Zermatten, M. V. Costache, S. Auffret, S. Bandiera, B. Rodmacq, A. Schuhl, and P. Gambardella, "Perpendicular switching of a single ferromagnetic layer induced by in-plane current injection," *Nature*, vol. 476, pp. 189–193, Aug. 2011.

[71] L. Liu, C.-F. Pai, Y. Li, H. W. Tseng, D. C. Ralph, and R. A. Buhrman, "Spin-Torque Switching with the Giant Spin Hall Effect of Tantalum," *Science*, vol. 336, pp. 555–558, May 2012.

[72] A. Chernyshov, M. Overby, X. Liu, J. K. Furdyna, Y. Lyanda-Geller, and L. P. Rokhinson, "Evidence for reversible control of magnetization in a ferromagnetic material by means of spin–orbit magnetic field," *Nature Physics*, vol. 5, pp. 656–659, Sept. 2009.

[73] K. Garello, I. M. Miron, C. O. Avci, F. Freimuth, Y. Mokrousov, S. Blügel, S. Auffret, O. Boulle, G. Gaudin, and P. Gambardella, "Symmetry and magnitude of spin–orbit torques in ferromagnetic heterostructures," *Nature Nanotechnology*, vol. 8, pp. 587–593, Aug. 2013.

[74] J. E. Hirsch, "Spin Hall Effect," *Physical Review Letters*, vol. 83, pp. 1834–1837, Aug. 1999.

[75] S. D. Ganichev and L. E. Golub, "Interplay of Rashba/Dresselhaus spin splittings probed by photogalvanic spectroscopy –A review," *physica status solidi (b)*, vol. 251, pp. 1801–1823, Sept. 2014.

[76] A. Manchon and S. Zhang, "Theory of nonequilibrium intrinsic spin torque in a single nanomagnet," *Physical Review B*, vol. 78, p. 212405, Dec. 2008.

[77] P. Wadley, B. Howells, J. elezny, C. Andrews, V. Hills, R. P. Campion, V. Novak, K. Olejnik, F. Maccherozzi, S. S. Dhesi, S. Y. Martin, T. Wagner, J. Wunderlich, F. Freimuth, Y. Mokrousov, J. Kune, J. S. Chauhan, M. J. Grzybowski, A. W. Rushforth, K. W. Edmonds, B. L. Gallagher, and T. Jungwirth, "Electrical switching of an antiferromagnet," *Science*, vol. 351, pp. 587–590, Feb. 2016.

[78] Y.-G. Choi, D. Jo, K.-H. Ko, D. Go, K.-H. Kim, H. G. Park, C. Kim, B.-C.

Min, G.-M. Choi, and H.-W. Lee, "Observation of the orbital Hall effect in a light metal Ti," *Nature*, vol. 619, pp. 52–56, July 2023.
Number: 7968 Publisher: Nature Publishing Group.

[79] O. Busch, I. Mertig, and B. Göbel, "Orbital Hall effect and orbital edge states caused by s electrons," *Physical Review Research*, vol. 5, p. 043052, Oct. 2023.

[80] "X-Ray Diffraction."

[81] J. Clarke and A. I. Braginski, eds., *The SQUID Handbook: Fundamentals and Technology of SQUIDs and SQUID Systems.*
Wiley, 1 ed., May 2004.

[82] B. Josephson, "Possible new effects in superconductive tunnelling," *Physics Letters*, vol. 1, pp. 251–253, July 1962.

[83] S. Sze and K. K. Ng, *Physics of Semiconductor Devices.*
Wiley, 1 ed., Oct. 2006.

[84] M. Hayashi, J. Kim, M. Yamanouchi, and H. Ohno, "Quantitative characterization of the spin-orbit torque using harmonic Hall voltage measurements," *Physical Review B*, vol. 89, p. 144425, Apr. 2014.

[85] C. O. Avci, K. Garello, M. Gabureac, A. Ghosh, A. Fuhrer, S. F. Alvarado, and P. Gambardella, "Interplay of spin-orbit torque and thermoelectric effects in ferromagnet/normal-metal bilayers," *Physical Review B*, vol. 90, p. 224427, Dec. 2014.

[86] T. Schulz, K. Lee, B. Krüger, R. Lo Conte, G. V. Karnad, K. Garcia, L. Vila, B. Ocker, D. Ravelosona, and M. Kläui, "Effective field analysis using the full angular spin-orbit torque magnetometry dependence," *Physical Review B*, vol. 95, p. 224409, June 2017.

[87] S. Dutta, A. Bose, A. A. Tulapurkar, R. A. Buhrman, and D. C. Ralph, "Interfacial and bulk spin Hall contributions to fieldlike spin-orbit torque generated by iridium," *Physical Review B*, vol. 103, p. 184416, May 2021.

[88] K. Behnia and H. Aubin, "Nernst effect in metals and superconductors: a review of concepts and experiments," *Reports on Progress in Physics*, vol. 79, p. 046502, Apr. 2016.

[89] N. Roschewsky, E. S. Walker, P. Gowtham, S. Muschinske, F. Hellman, S. R. Bank, and S. Salahuddin, "Spin-orbit torque and Nernst effect in Bi-Sb/Co heterostructures," *Physical Review B*, vol. 99, p. 195103, May 2019.

[90] L. Liu, T. Moriyama, D. C. Ralph, and R. A. Buhrman, "Spin-Torque Ferromagnetic Resonance Induced by the Spin Hall Effect," *Physical Review Letters*, vol. 106, p. 036601, Jan. 2011.

[91] M. Harder, Y. Gui, and C.-M. Hu, "Electrical detection of magnetization dynamics via spin rectification effects," *Physics Reports*, vol. 661, pp. 1–59, Nov. 2016.

[92] S.-J. Kim, D.-K. Lee, S.-H. Oh, H. C. Koo, and K.-J. Lee, "Theory of spin-torque ferrimagnetic resonance," *Physical Review B*, vol. 104, p. 024405, July 2021.

[93] J. Kübler and C. Felser, "Non-collinear antiferromagnets and the anomalous Hall effect," *EPL (Europhysics Letters)*, vol. 108, p. 67001, Dec. 2014.

[94] N. Kiyohara, T. Tomita, and S. Nakatsuji, “Giant Anomalous Hall Effect in the Chiral Antiferromagnet Mn3Ge,” *Phys. Rev. Appl.*, vol. 5, p. 064009, jun 2016.

[95] A. Rajan, T. G. Saunderson, F. R. Lux, R. Y. Díaz, H. M. Abdullah, A. Bose, B. Bednarz, J.-Y. Kim, D. Go, T. Hajiri, G. Shukla, O. Gomonay, Y. Yao, W. Feng, H. Asano, U. Schwingenschlögl, L. López-Díaz, J. Sinova, Y. Mokrousov, A. Manchon, and M. Kläui, “Revealing the higher-order spin nature of the Hall effect in non-collinear antiferromagnet $\mathrm{Mn_3Ni_{0.35}Cu_{0.65}N}$,” 2023.
Publisher: arXiv Version Number: 1.

[96] G. Kimbell, C. Kim, W. Wu, M. Cuoco, and J. W. Robinson, “Challenges in identifying chiral spin textures via the topological Hall effect,” *Commun. Mater.*, vol. 3, p. 19, apr 2022.

[97] Z. Q. Liu, H. Chen, J. M. Wang, J. H. Liu, K. Wang, Z. X. Feng, H. Yan, X. R. Wang, C. B. Jiang, J. M. D. Coey, and A. H. MacDonald, “Electrical switching of the topological anomalous Hall effect in a non-collinear antiferromagnet above room temperature,” *Nature Electronics*, vol. 1, pp. 172–177, Mar. 2018.

[98] P. K. Rout, P. V. P. Madduri, S. K. Manna, and A. K. Nayak, “Field-induced topological Hall effect in the noncoplanar triangular antiferromagnetic geometry of Mn 3 Sn,” *Physical Review B*, vol. 99, p. 094430, Mar. 2019.

[99] K. Oda, T. Moriyama, and T. Ono, “Magnetoresistance in Bilayers of Heavy Metal and Non-collinear Antiferromagnet,” *Journal of the Magnetics Society of Japan*, vol. 43, p. n/a, Jan. 2019.

[100] B. Dieny, I. L. Prejbeanu, K. Garello, P. Gambardella, P. Freitas, R. Lehndorff, W. Raberg, U. Ebels, S. O. Demokritov, J. Akerman, A. Deac, P. Pirro, C. Adelmann, A. Anane, A. V. Chumak, A. Hirohata, S. Mangin, S. O. Valenzuela, M. C. Onbaşlı, M. d’Aquino, G. Prenat, G. Finocchio, L. Lopez-Diaz, R. Chantrell, O. Chubykalo-Fesenko, and P. Bortolotti, “Opportunities and challenges for spintronics in the microelectronics industry,” *Nature Electronics*, vol. 3, pp. 446–459, Aug. 2020.

[101] R. Gupta, C. Bouard, F. Kammerbauer, J. O. Ledesma-Martin, A. Bose, I. Kononenko, S. Martin, P. Usé, G. Jakob, M. Drouard, and M. Kläui, “Harnessing orbital Hall effect in spin-orbit torque MRAM,” *Nature Communications*, vol. 16, p. 130, Jan. 2025.

[102] H. Chen, P. Qin, H. Yan, Z. Feng, X. Zhou, X. Wang, Z. Meng, L. Liu, and Z. Liu, “Noncollinear Antiferromagnetic Spintronics,” 2022.
Publisher: arXiv Version Number: 2.

[103] J. Železný, Y. Zhang, C. Felser, and B. Yan, “Spin-Polarized Current in Noncollinear Antiferromagnets,” *Phys. Rev. Lett.*, vol. 119, p. 187204, nov 2017.

[104] X. Chen, T. Higo, K. Tanaka, T. Nomoto, H. Tsai, H. Idzuchi, M. Shiga, S. Sakamoto, R. Ando, H. Kosaki, T. Matsuo, D. Nishio-Hamane, R. Arita, S. Miwa, and S. Nakatsuji, “Octupole-driven magnetoresistance in an antiferromagnetic tunnel junction,” *Nature*, vol. 613, pp. 490–495, Jan. 2023.

[105] M. Dc, D.-F. Shao, V. D.-H. Hou, A. Vailionis, P. Quarterman, A. Habiboglu, M. B. Venuti, F. Xue, Y.-L. Huang, C.-M. Lee, M. Miura, B. Kirby, C. Bi, X. Li, Y. Deng, S.-J. Lin, W. Tsai, S. Eley, W.-G. Wang, J. A. Borchers, E. Y. Tsymbal, and S. X. Wang, "Observation of anti-damping spin–orbit torques generated by in-plane and out-of-plane spin polarizations in MnPd3," *Nature Materials*, vol. 22, pp. 591–598, May 2023.

[106] M. Kimata, H. Chen, K. Kondou, S. Sugimoto, P. K. Muduli, M. Ikhlas, Y. Omori, T. Tomita, A. H. MacDonald, S. Nakatsuji, and Y. Otani, "Magnetic and magnetic inverse spin Hall effects in a non-collinear antiferromagnet," *Nature*, vol. 565, pp. 627–630, Jan. 2019.

[107] L.-c. Zhang, D. Go, J.-P. Hanke, P. M. Buhl, S. Grytsiuk, S. Blügel, F. R. Lux, and Y. Mokrousov, "Imprinting and driving electronic orbital magnetism using magnons," *Communications Physics*, vol. 3, p. 227, Dec. 2020.

[108] L. Alahmed, X. Zhang, J. Wen, Y. Xiong, Y. Li, L.-c. Zhang, F. Lux, F. Freimuth, M. Mahdi, Y. Mokrousov, V. Novosad, W.-K. Kwok, D. Yu, W. Zhang, Y. S. Lee, and P. Li, "Evidence of Magnon-Mediated Orbital Magnetism in a Quasi-2D Topological Magnon Insulator," *Nano Letters*, vol. 22, pp. 5114–5119, July 2022.

[109] D. Xiao, M.-C. Chang, and Q. Niu, "Berry phase effects on electronic properties," *Reviews of Modern Physics*, vol. 82, pp. 1959–2007, July 2010.

[110] S. Okamoto, T. Egami, and N. Nagaosa, "Critical Spin Fluctuation Mechanism for the Spin Hall Effect," *Physical Review Letters*, vol. 123, p. 196603, Nov. 2019.

[111] A. Crépieux and P. Bruno, "Theory of the anomalous Hall effect from the Kubo formula and the Dirac equation," *Physical Review B*, vol. 64, p. 014416, June 2001.

[112] Z. Qiu, J. Li, D. Hou, E. Arenholz, A. T. N'Diaye, A. Tan, K.-i. Uchida, K. Sato, S. Okamoto, Y. Tserkovnyak, Z. Q. Qiu, and E. Saitoh, "Spin-current probe for phase transition in an insulator," *Nature Communications*, vol. 7, p. 12670, Aug. 2016.

[113] D. Hou, Z. Qiu, J. Barker, K. Sato, K. Yamamoto, S. Vélez, J. M. Gomez-Perez, L. E. Hueso, F. Casanova, and E. Saitoh, "Tunable Sign Change of Spin Hall Magnetoresistance in Pt / NiO / YIG Structures," *Physical Review Letters*, vol. 118, p. 147202, Apr. 2017.

[114] Z. Qiu, D. Hou, J. Barker, K. Yamamoto, O. Gomonay, and E. Saitoh, "Spin colossal magnetoresistance in an antiferromagnetic insulator," *Nature Materials*, vol. 17, pp. 577–580, July 2018.

[115] D. Lee, D. Go, H.-J. Park, W. Jeong, H.-W. Ko, D. Yun, D. Jo, S. Lee, G. Go, J. H. Oh, K.-J. Kim, B.-G. Park, B.-C. Min, H. C. Koo, H.-W. Lee, O. Lee, and K.-J. Lee, "Orbital torque in magnetic bilayers," Nov. 2021.
Publisher: Zenodo.

[116] A. Bose, F. Kammerbauer, R. Gupta, D. Go, Y. Mokrousov, G. Jakob, and M. Kläui, "Detection of long-range orbital-Hall torques," *Physical Review B*, vol. 107, p. 134423, Apr. 2023.

[117] H. Hayashi, D. Jo, D. Go, T. Gao, S. Haku, Y. Mokrousov, H.-W. Lee, and K. Ando, "Observation of long-range orbital transport and giant orbital torque," *Communications Physics*, vol. 6, p. 32, Feb. 2023.

[118] W. Zhang, W. Han, S.-H. Yang, Y. Sun, Y. Zhang, B. Yan, and S. S. P. Parkin, "Giant facet-dependent spin-orbit torque and spin Hall conductivity in the triangular antiferromagnet $IrMn_3$," *Science Advances*, vol. 2, p. e1600759, Sept. 2016.

[119] K. Kondou, H. Chen, T. Tomita, M. Ikhlas, T. Higo, A. H. MacDonald, S. Nakatsuji, and Y. Otani, "Giant field-like torque by the out-of-plane magnetic spin Hall effect in a topological antiferromagnet," *Nature Communications*, vol. 12, p. 6491, Nov. 2021.

[120] H. Bai, X. F. Zhou, H. W. Zhang, W. W. Kong, L. Y. Liao, X. Y. Feng, X. Z. Chen, Y. F. You, Y. J. Zhou, L. Han, W. X. Zhu, F. Pan, X. L. Fan, and C. Song, "Control of spin-orbit torques through magnetic symmetry in differently oriented noncollinear antiferromagnetic Mn 3 Pt," *Physical Review B*, vol. 104, p. 104401, Sept. 2021.

[121] S. Hu, D.-F. Shao, H. Yang, C. Pan, Z. Fu, M. Tang, Y. Yang, W. Fan, S. Zhou, E. Y. Tsymbal, and X. Qiu, "Efficient perpendicular magnetization switching by a magnetic spin Hall effect in a noncollinear antiferromagnet," *Nature Communications*, vol. 13, p. 4447, Aug. 2022.

[122] J. Holanda, H. Saglam, V. Karakas, Z. Zang, Y. Li, R. Divan, Y. Liu, O. Ozatay, V. Novosad, J. E. Pearson, and A. Hoffmann, "Magnetic Damping Modulation in IrMn 3 / Ni 80 Fe 20 via the Magnetic Spin Hall Effect," *Physical Review Letters*, vol. 124, p. 087204, Feb. 2020.

[123] H. Xie, X. Chen, Q. Zhang, Z. Mu, X. Zhang, B. Yan, and Y. Wu, "Magnetization switching in polycrystalline Mn3Sn thin film induced by self-generated spin-polarized current," *Nat. Commun. 2022*, vol. 13, p. 5744, sep 2022.

[124] H. Iwaki, M. Kimata, T. Ikebuchi, Y. Kobayashi, K. Oda, Y. Shiota, T. Ono, and T. Moriyama, "Large anomalous Hall effect in L12-ordered antiferromagnetic Mn3Ir thin films," *Appl. Phys. Lett.*, vol. 116, p. 022408, jan 2020.

[125] L. Ye, Y. Tian, X. Jin, and D. Xiao, "Temperature dependence of the intrinsic anomalous Hall effect in nickel," *Physical Review B*, vol. 85, p. 220403, June 2012.

[126] T. Miyasato, N. Abe, T. Fujii, A. Asamitsu, S. Onoda, Y. Onose, N. Nagaosa, and Y. Tokura, "Crossover Behavior of the Anomalous Hall Effect and Anomalous Nernst Effect in Itinerant Ferromagnets," *Physical Review Letters*, vol. 99, p. 086602, Aug. 2007.

[127] For the program description, see https://www.flapw.de.

[128] E. Wimmer, H. Krakauer, M. Weinert, and A. J. Freeman, "Full-potential self-consistent linearized-augmented-plane-wave method for calculating the electronic structure of molecules and surfaces: O2 molecule," *Phys. Rev. B*, vol. 24, no. 2, pp. 864–875, 1981.

[129] J. P. Perdew, K. Burke, and M. Ernzerhof, "Generalized Gradient Approximation Made Simple," *Phys. Rev. Lett.*, vol. 77, no. 18, pp. 3865–3868, 1996.

[130] K. Zhao, T. Hajiri, H. Chen, R. Miki, H. Asano, and P. Gegenwart, "Anomalous hall effect in the noncollinear antiferromagnetic antiperovskite $\mathrm{Mn_3Ni_{1-x}Cu_{x}N}$," *Phys. Rev. B*, vol. 100, no. 4, p. 045109, 2019.

[131] X. Wang, J. R. Yates, I. Souza, and D. Vanderbilt, "Ab initio calculation of the anomalous Hall conductivity by Wannier interpolation," *Phys. Rev. B - Condens. Matter Mater. Phys.*, vol. 74, no. 19, p. 195118, 2006.

[132] G. Pizzi, V. Vitale, R. Arita, S. Blügel, F. Freimuth, G. Géranton, M. Gibertini, D. Gresch, C. Johnson, T. Koretsune, J. Ibantilde;ez-Azpiroz, H. Lee, J. M. Lihm, D. Marchand, A. Marrazzo, Y. Mokrousov, J. I. Mustafa, Y. Nohara, Y. Nomura, L. Paulatto, S. Poncé, T. Ponweiser, J. Qiao, F. Thöle, S. S. Tsirkin, M. Wierzbowska, N. Marzari, D. Vanderbilt, I. Souza, A. A. Mostofi, and J. R. Yates, "Wannier90 as a community code: New features and applications," *J. Phys. Condens. Matter*, vol. 32, no. 16, p. 165902, 2020.

[133] F. Freimuth, Y. Mokrousov, D. Wortmann, S. Heinze, and S. Blügel, "Maximally localized Wannier functions within the FLAPW formalism," *Phys. Rev. B - Condens. Matter Mater. Phys.*, vol. 78, no. 3, p. 035120, 2008.

[134] N. Nagaosa, J. Sinova, S. Onoda, A. H. MacDonald, and N. P. Ong, "Anomalous Hall effect," *Rev. Mod. Phys.*, vol. 82, no. 2, pp. 1539–1592, 2010.